Max-Planck-Institut
für Meteorologie

MAX-PLANCK-GESELLSCHAFT

International Max Planck Research School
on Earth System Modelling

Numerical Studies of Stratosphere-Troposphere Dynamical Coupling in a Changing Climate

Felix Bunzel

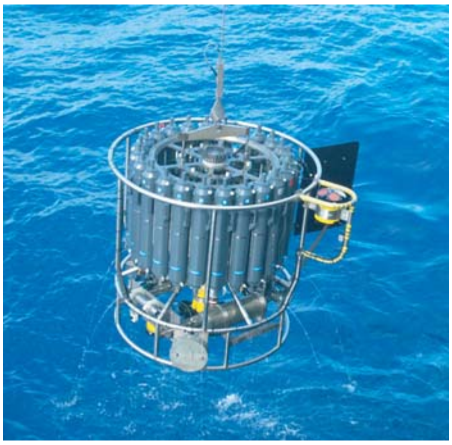

Berichte zur Erdsystemforschung 137/2013

Reports on Earth System Science

Hinweis

Die Berichte zur Erdsystemforschung werden vom Max-Planck-Institut für Meteorologie in Hamburg in unregelmäßiger Abfolge herausgegeben.

Sie enthalten wissenschaftliche und technische Beiträge, inklusive Dissertationen.

Die Beiträge geben nicht notwendigerweise die Auffassung des Instituts wieder.

Die "Berichte zur Erdsystemforschung" führen die vorherigen Reihen "Reports" und "Examensarbeiten" weiter.

Notice

The Reports on Earth System Science are published by the Max Planck Institute for Meteorology in Hamburg. They appear in irregular intervals.

They contain scientific and technical contributions, including Ph. D. theses.

The Reports do not necessarily reflect the opinion of the Institute.

The "Reports on Earth System Science" continue the former "Reports" and "Examensarbeiten" of the Max Planck Institute.

Anschrift / Address

Max-Planck-Institut für Meteorologie
Bundesstrasse 53
20146 Hamburg
Deutschland

Tel.: +49-(0)40-4 11 73-0
Fax: +49-(0)40-4 11 73-298
Web: www.mpimet.mpg.de

Layout:

Bettina Diallo, PR & Grafik

Titelfotos:
vorne:
Christian Klepp - Jochem Marotzke - Christian Klepp
hinten:
Clotilde Dubois - Christian Klepp - Katsumasa Tanaka

Berichte zur Erdsystemforschung
137
2013

Numerical Studies of Stratosphere-Troposphere Dynamical Coupling in a Changing Climate

Felix Bunzel

aus Hamburg

Hamburg 2013

Reports on Earth System Science
137
2013

ISSN 1614-1199

Felix Bunzel
Max-Planck-Institut für Meteorologie
Bundesstrasse 53
20146 Hamburg

Als Dissertation angenommen
vom Department Geowissenschaften der Universität Hamburg

auf Grund der Gutachten von
Prof. Dr. Bjorn Stevens
und
Dr. Hauke Schmidt

Hamburg, den 7. Juni 2013
Prof. Dr. Jürgen Oßenbrügge
Leiter des Departments für Geowissenschaften

ISSN 1614-1199

Numerical Studies of Stratosphere-Troposphere Dynamical Coupling in a Changing Climate

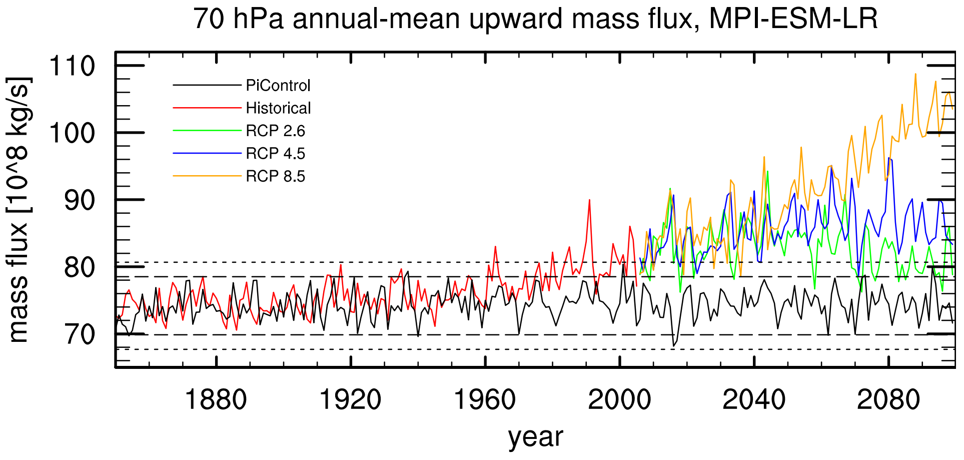

Felix Bunzel

Hamburg 2013

Abstract

In this thesis the behaviour of stratosphere-troposphere dynamical coupling under a changing climate is investigated. The response of the main features of stratospheric dynamics to a changing climate is evaluated, and the implications of stratospheric changes for the troposphere-surface system are assessed. A prominent feature of stratospheric dynamics is the stratospheric meridional overturning circulation, the Brewer-Dobson Circulation (BDC). The BDC is driven by the dissipation and breaking of different types of upward propagating atmospheric waves which originate from the troposphere.

Recent modelling studies showed that the tropospheric warming and simultaneous stratospheric cooling, induced by increasing greenhouse gas (GHG) concentrations, modify the driving forces of the BDC in a changing climate by exerting an upward shift on the critical layers for wave dissipation. The vast majority of climate models consistently simulates a BDC strengthening for the last decades. Observational datasets, however, indicate no significant change or even a slight decrease in BDC strength over the last 30 years. Both significance and origin of this discrepancy between model and observational data are studied in this thesis.

First the mechanisms that drive the BDC are investigated. Although most models produce a qualitatively similar response, an acceleration of the BDC in a changing climate, the mechanisms causing this acceleration are still not fully understood. In some models the simulated BDC strengthening is mainly due to the drag originating from resolved large-scale waves, while other models find the parameterised small-scale wave drag to yield the more prominent contribution to the positive trend in BDC strength. It is also unclear to what extent the simulated BDC response depends on the representation of the stratosphere in a model. In order to investigate the impact of both vertical resolution and vertical extent of a model on the simulated BDC trend, sensitivity simulations with the General Circulation Model ECHAM6 were performed for three different model configurations and for three different sets of boundary conditions, representing preindustrial, present-day, and future climate states. Tropical upwelling velocities and age of stratospheric air are used as a measure for the strength of the BDC. Both consistently show a BDC strengthening from the preindustrial to the future time slice for all configurations of the model. However, the amplitude and origin of this change vary among the different setups. Analyses of the tropical upward mass flux indicate that in the model with a lid at 10 hPa (*low top*) the BDC strengthening at 70 hPa is primarily produced by resolved wave drag, while in the model with a higher lid (0.01 hPa, *high top*) the parameterised wave drag yields the main contribution to the BDC increase. This implies that consistent changes in the BDC originate from different causes when the stratosphere is not sufficiently resolved in a model. Furthermore, the effect of enhancing the horizontal diffusion in the upper model layers to avoid resolved wave reflection at the model lid is quantified, and a possible link to the different behaviour of the low-top model with regard to the origin of the BDC change is identified.

Trends in the strength of the BDC may also be confused with or masked by natural BDC variability. In order to further investigate the discrepancy between model and observational data in terms of the BDC strength, the natural BDC variability is assessed in this study from a multi-centennial preindustrial control simulation, performed with the Max Planck Institute Earth System Model (MPI-ESM). The obtained results indicate substantial decadal-scale natural BDC variability modes. These modes of variability imply that in the second half of the 20th century at least 30 years of model data with good spatial and temporal coverage is necessary to obtain a trend in BDC strength, which is significantly distinguishable from natural BDC variability.

The described ECHAM6 time-slice simulations together with transient simulations with MPI-ESM are also analysed to evaluate the stratosphere-troposphere dynamical coupling and its behaviour in a changing climate. The Northern Annular Mode (NAM) index, which can be considered as a measure for the strength of the stratospheric polar vortex, is used to define extreme events in stratospheric polar vortex strength. The weeks before and after the occurrence of such events are well-suited to investigate stratosphere-troposphere coupling, since the associated dynamical disturbance originates from the troposphere. After triggering an extreme stratospheric event, the dynamical disturbance often yields significant feedback effects for the troposphere-surface system. These effects are, e.g., reflected by a shift in the index of the North Atlantic Oscillation (NAO), which is a key index for the weather and climate in central and northern Europe and Eurasia.

Neither the simulated climate state nor the applied ECHAM6 model configuration indicates a significant impact on the frequency of extreme stratospheric events or on the ratio of downward to non-downward propagating events. However, transient multi-centennial simulations with MPI-ESM show a substantial increase in the frequency of sudden stratospheric warming events, which usually coincide with weak polar vortex events, in the second half of the 21st century in the RCP4.5 and RCP8.5 scenario. This increase is followed in the RCP8.5 scenario by a relatively rapid drop in SSW frequency after 2100. Almost simultaneously, the troposphere-surface system undergoes a transition, which is reflected by a positive shift in the NAO index. This positive shift would imply more mild winters over central and northern Europe and Eurasia after 2100.

Zusammenfassung

In dieser Arbeit wird das Verhalten der dynamischen Kopplung zwischen Stratosphäre und Troposphäre in einem sich ändernden Klima untersucht. Zunächst wird der Einfluss des sich wandelnden Klimas auf die Dynamik der Stratosphäre ausgewertet, anschließend werden die Auswirkungen einer stratosphärischen Veränderung auf die Troposphäre und die Erdoberfläche analysiert. Ein bedeutendes Merkmal der Stratosphärendynamik ist die stratosphärische "Meridional Overturning Circulation", die sogenannte Brewer-Dobson-Zirkulation (BDC). Die BDC wird angetrieben durch die Dissipation und das Brechen aufwärts in der Atmosphäre propagierender Wellen, die ihren Ursprung in der Troposphäre haben.

Jüngste Modellstudien haben gezeigt, dass die Temperatureffekte der ansteigenden Treibhausgaskonzentrationen in der Troposphäre (Erwärmung) und Stratosphäre (Abkühlung) die Antriebskräfte der BDC verändern. Dies geschieht durch eine Aufwärtsverschiebung der für die Wellendissipation verantwortlichen Luftschichten. Die große Mehrheit der Klimamodelle simuliert konsistent eine Verstärkung der BDC für die vergangenen Jahrzehnte. Dieses Verhalten wird von den Beobachtungsdaten der letzten 30 Jahre allerdings nicht bestätigt. Hier konnte keine signifikante BDC-Änderung festgestellt werden. Signifikanz und Ursache dieser Diskrepanz zwischen Modell- und Beobachtungsdaten werden in dieser Arbeit untersucht.

Zunächst werden die Antriebskräfte der BDC analysiert. Obwohl die meisten Modelle ein qualitativ ähnliches Verhalten - eine Verstärkung der BDC in einem sich wandelnden Klima - simulieren, können die Mechanismen, die zu dieser Verstärkung führen, noch nicht vollständig erklärt werden. In manchen Modellen wird die BDC-Verstärkung hauptsächlich durch die Dissipation von aufgelösten großskaligen Wellen hervorgerufen. In anderen Modellen hingegen, liefern die parametrisierten kleinskaligen Wellen den größeren Beitrag. Es ist ebenfalls unklar, inwiefern die simulierte BDC-Änderung von der Modellkonfiguration hinsichtlich der Stratosphäre abhängt. Um den Einfluss der vertikalen Auflösung sowie der vertikalen Ausdehnung eines Modells auf die simulierte BDC-Änderung zu untersuchen, wurden im Rahmen dieser Arbeit Sensitivitätsstudien mit dem Allgemeinen Zirkulationsmodell ECHAM6 durchgeführt. Hierbei wurden drei verschiedene Modellkonfigurationen und drei verschiedene Klimazustände untersucht. Die drei Klimazustände werden durch Randbedingungen beschrieben, die dem präindustriellen, dem aktuellen und dem in Zukunft zu erwartenden Klima entsprechen. Die Geschwindigkeit des tropischen Aufwärtstransports sowie das stratosphärische Luftalter werden als Maß für die BDC-Stärke herangezogen. Beide Größen zeigen konsistent eine Verstärkung der BDC vom präindustriellen zum zukünftigen Klimazustand. Jedoch zeigt sich sowohl bezüglich des Ausmaßes als auch der Herkunft der BDC-Verstärkung eine starke Abhängigkeit von der Modellkonfiguration. Analysen der Geschwindigkeit des tropischen Aufwärtstransports zeigen, dass die BDC-Verstärkung hauptsächlich durch die Dissipation aufgelöster großskaliger Wellen hervorgerufen wird, wenn die Modellkonfiguration mit geringer Vertikalausdehnung (bis 10 hPa) verwendet wird. Andererseits wird die BDC-Verstärkung eher von kleinskaligen parametrisierten Wellen hervorgerufen, wenn die Konfiguration mit hoher Vertikalausdehnung (bis 0,01 hPa) benutzt wird. Daraus folgt, dass zwar konsistente BDC-Veränderungen simuliert werden, wenn die Stratosphäre im Modell nicht gut aufgelöst ist, die Ursache jedoch eine andere ist als bei der Modellkonfiguration mit hoher Vertikalausdehnung. Des Weiteren wird hier der Effekt der künstlich erhöhten Horizontaldiffusion in den oberen Modellschichten quantifiziert, die zur Vermeidung von Reflexion großskaliger Wellen am oberen Modellrand dient. Eine mögliche Verbindung zum unterschiedlichen Verhalten des Modells mit geringer Vertikalausdehnung bezüglich der simulierten Herkunft der BDC-Verstärkung wird aufgezeigt.

Zeitliche Veränderungen in der BDC-Stärke können auch mit natürlicher BDC-Variabilität verwechselt oder von ihr überdeckt werden. Um weiter auf die Diskrepanz zwischen Modell- und Beobachtungsdaten hinsichtlich der gezeigten BDC-Stärke einzugehen, wird die natürliche BDC-Variabilität in dieser Arbeit anhand eines Modelllaufs des Erdsystem-Modells MPI-ESM analysiert, der mehrere Jahrhunderte unter konstanten präindustriellen Randbedingungen simuliert. In diesen Simulationen zeigt sich eine erhebliche dekadische Variabilität der BDC-Stärke. Es stellt sich heraus, dass diese Variabilität zur Folge hat, dass in der zweiten Hälfte des 20. Jahrhunderts Modelldaten für mindestens 30 simulierte Jahre mit guter zeitlicher und räumlicher Auflösung notwendig sind, um eine BDC-Veränderung nachzuweisen, die sich signifikant von der natürlichen Variabilität der BDC unterscheidet.

Die beschriebenen ECHAM6-Zeitscheiben-Simulationen sowie die transienten Simulationen mit MPI-ESM werden des Weiteren analysiert, um die dynamische Kopplung zwischen Stratosphäre und Troposphäre in einem sich wandelnden Klima zu untersuchen. Der Index der “Northern Annular Mode” (NAM) wird als Maß für die Stärke des Polarwirbels herangezogen und verwendet, um Extremereignisse in der Polarwirbelstärke zu definieren. Die Wochen vor und nach solchen Extremereignissen eignen sich gut zur Untersuchung der dynamischen Kopplung zwischen Stratosphäre und Troposphäre, da die auslösende dynamische Störung des Wirbels troposphärischen Ursprungs ist. Ein solches Extremereignis geht häufig einher mit einem Rückkopplungseffekt, der eine signifikante Veränderung des Troposphären-Oberflächen-Systems nach sich zieht. Der Einfluss dieses Rückkopplungseffekts zeigt sich z.B. in einer Veränderung des Indexes der Nordatlantischen Oszillation (NAO), der als Kennzahl für das Wetter und Klima in Zentral- und Nordeuropa sowie Eurasien gilt.

Weder der simulierte Klimazustand noch die verwendete ECHAM6-Modellkonfiguration zeigen einen signifikanten Einfluss auf die Häufigkeit der stratosphärischen Extremereignisse. Auch bezüglich des Anteils der stratosphärischen Extremereignisse, die einen signifikanten Rückkopplungseffekt auf die Troposphäre nach sich ziehen, hat sich kein signifikanter Einfluss gezeigt. Die transienten Simulationen mit MPI-ESM, die sich über mehrere Jahrhunderte erstrecken, zeigen jedoch einen erheblichen Anstieg der Häufigkeit von spontanen Stratosphärenerwärmungen (SSWs) in der zweiten Hälfte des 21. Jahrhunderts im RCP4.5- und RCP8.5-Szenario. SSW-Ereignisse stellen einen Extremfall der stratosphärischen Schwachwirbelereignisse dar. Im RCP8.5-Szenario ist dieser Anstieg in der SSW-Häufigkeit gefolgt von einem relativ abrupten Rückgang nach 2100. Dieser Rückgang geht einher mit einer Veränderung im Troposphären-Oberflächen-System, die sich in einer positiven Anomalie des NAO-Indexes zeigt. Diese positive Anomalie würde eine höhere Anzahl milder Winter nach 2100 in Zentral- und Nordeuropa sowie Eurasien zur Folge haben.

Contents

Chapter 1

Introduction

The Earth's climate is characterised by complex interactions of various dynamical, radiative and chemical processes acting on different timescales. These do not only comprise atmospheric processes. Also the other components of the Earth System - the ocean and the land surface - as well as their interaction with the atmosphere have to be accounted for.

In the Earth's atmosphere, different layers defined by the vertical structure of the temperature field are distinguished (see Fig. 1.1). The interaction between atmosphere, ocean, and land surface takes place in the lowest part of the atmosphere, the troposphere. This layer contains roughly 80% of the atmosphere's mass and on average extends up to approximately 11 km (depending on season and latitude). The upper boundary of the troposphere, the tropopause, is characterised by a temperature inversion. Berson and Süring were the first to reach this region of the atmosphere during their record balloon flight over Berlin in 1901. Thus, they confirmed earlier hints of a temperature inversion from automated measurements (Aßmann, 1902; Teisserenc de Bort, 1902). The tropopause largely prevents the exchange of mass between the troposphere and the layer above, the stratosphere. In the stratosphere, high concentrations of ozone (O_3) absorb a significant amount of the incoming solar short-wave radiation. Thus, the ozone prevents life on the Earth's surface from harmful ultraviolet (UV) radiation, and increases the air temperature in the stratosphere with height. The positive vertical temperature gradient leads to a stable stratification of air masses in this part of the atmosphere. The region of high ozone concentrations extends up to the stratopause located at about 50 km altitude, where the vertical temperature gradient reverses again. In the above layer, the mesosphere, the temperature decreases with height up to an altitude of on average roughly 100 km, where the mesopause separates the so-called *middle atmosphere* (stratosphere and mesosphere) from the *upper atmosphere* (thermosphere and above). In contrast to the middle atmosphere, where the atmospheric constituents are still relatively well mixed, in the upper atmosphere the constituents are separated vertically by their molecular mass, as molecular diffusion exceeds the effect of mixing processes.

Although the middle atmosphere contains less than 20% of the entire atmosphere's mass, it yields a few processes which are crucial for the troposphere-surface system and the life on Earth. The Brewer-Dobson Circulation (BDC, see Section 1.1.1) is a

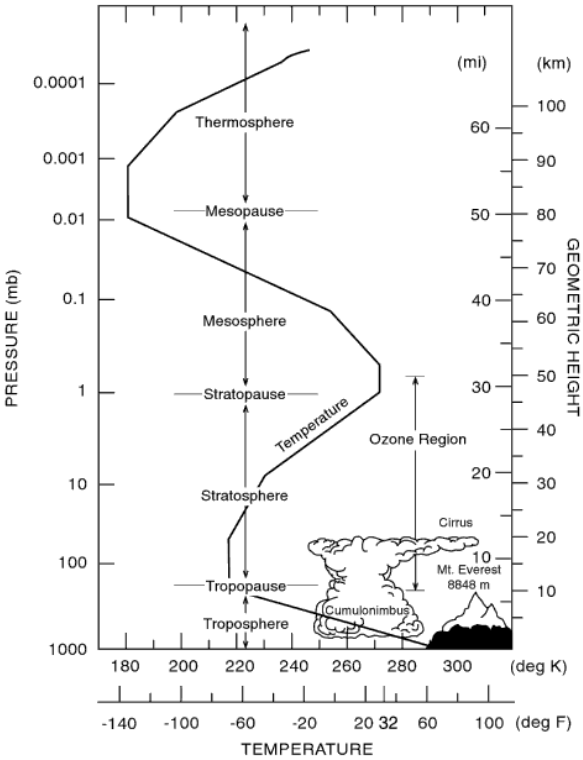

Figure 1.1: The vertical profile of the thermal structure of the atmosphere is shown. [Figure from Andrews et al. (1987)]

large-scale meridional overturning circulation, which transports air masses on various pathways from the tropical lower stratosphere towards higher latitudes. As ozone is primarily produced in the tropics, it is distributed by the BDC to the middle and high latitudes, shielding also these areas from harmful solar UV radiation.

While the breaking and dissipation of atmospheric waves drive the meridional transport of air parcels from the tropics to higher latitudes in the middle atmosphere, a strong wind regime, referred to as the polar vortex, acts as a transport barrier on the winter hemisphere and, thus, largely prevents the air parcels from reaching the winter pole. On the northern hemisphere, however, the occurrence of an extreme stratospheric event (see Section 1.1.2) coinciding with a breakdown of the polar vortex, may cause an increase in the stratospheric polar cap temperature of up to 30 K or more within a few days. Via dynamical stratosphere-troposphere coupling (see Section 1.1.3) these stratospheric anomalies propagate downward during the first 1-3 months after an event and, statistically, even yield a significant impact on the troposphere-surface system.

In this thesis the behaviour of the strength and pattern of the BDC is investigated in a changing climate. Different configurations of state-of-the-art climate models are used to assess the impact of the model setup on stratospheric dynamics and its simulated change under increasing GHG concentrations. Most climate models simulate a BDC strengthening under a GHG-induced climate change, already for the second half of the 20th century. Observational datasets, however, indicate no significant trend. This discrepancy is studied by assessing the natural BDC variability from multi-centennial model simulations, and contrasting it to BDC trends derived from both model and observational datasets. Additionally, it is evaluated how a future change in the occurrence of extreme stratospheric events may affect the troposphere-surface system.

1.1 State of the art

While progress in computer science in the past decades has been rapid, also the capability of state-of-the-art climate models to simulate the complex interactions of processes in the Earth's climate system realistically has increased. State-of-the-art atmospheric General Circulation Models are not only run in a stand-alone version with many prescribed input datasets, but are also used as a part of Earth System Models, which include the interactive simulation of the ocean, the land surface, and partly even the impact of aerosols and chemical processes. Since a significant impact of the middle atmosphere on the tropospheric state has been identified, the interactive simulation of processes taking place in the middle atmosphere has been incorporated into the new generation of climate models.

In the last decades many different studies investigated middle atmospheric processes, their origin, as well as their impact on the troposphere-surface system in model simulations and observational datasets. As the length of observational time series increases, the opportunities to test the quality of the models become more diverse. In the following an overview about the state-of-the-art understanding of the main processes involved in middle atmosphere dynamics and the coupling between stratosphere and troposphere, as derived from both model simulations and observational data, is given.

1.1.1 The Brewer-Dobson Circulation

When Brewer (1949) and Dobson (1952) investigated the distribution of water vapour and ozone in the stratosphere, respectively, the first evidence for a large-scale circulation, or *world circulation*, of air parcels in the middle atmosphere was found. The breaking and dissipation of different types of atmospheric waves originating from the troposphere induce this meridional overturning circulation, the Brewer-Dobson Circulation (BDC, see Fig. 1.2), in the middle atmosphere (Holton et al., 1995). On the one hand, these waves comprise large-scale planetary and synoptic-scale waves, which are resolved by models and global-scale observational datasets. On the other hand, unresolved small-scale waves, such as gravity waves, originating partly from the orography, yield a significant contribution to the BDC at some heights and latitudes. In order to account for the effect of unresolved waves in climate models, parameterisation schemes are developed and incorporated into the models.

Measures of the BDC strength. In comprehensive middle atmosphere resolving climate models as well as in observational datasets, there are two widely accepted methods to obtain a measure of the BDC strength. Either the tropical upward mass flux is evaluated from the residual mean meridional circulation (see Section 3.1.1), as formulated by Andrews et al. (1987) in the transformed Eulerian-mean (TEM)

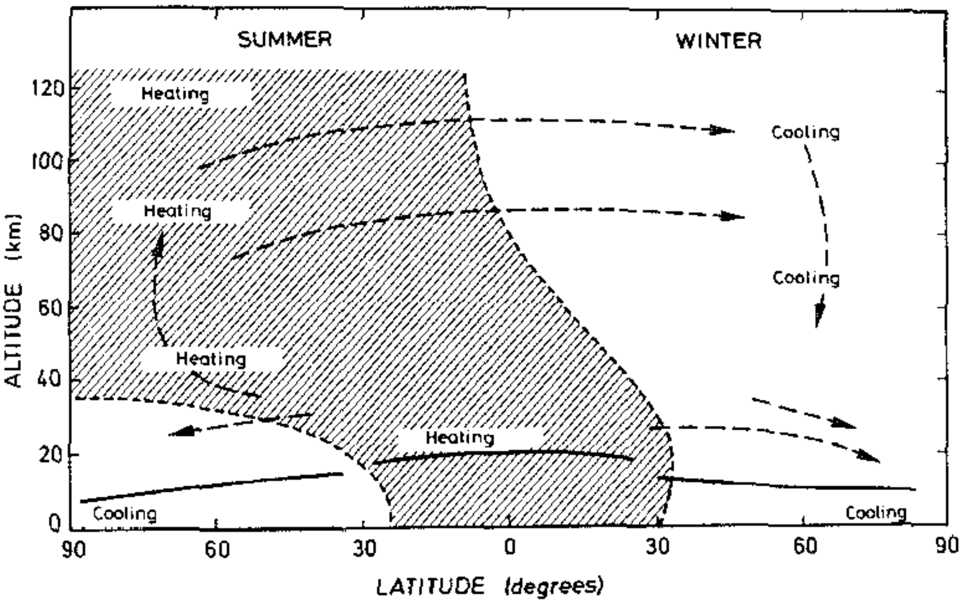

Figure 1.2: The meridional circulation, consisting of tropical upwelling, transport from the summer to the winter hemisphere in the middle and upper atmosphere, as well as extratropical downwelling, is shown based on the study by Murgatroyd and Singleton (1961). [Figure from Murgatroyd (1971)]

framework, or the mean age of stratospheric air (Hall and Plumb, 1994) is derived by using mixing ratios of atmospheric trace species (see Section 3.4). In model simulations the age of air can also be obtained by introducing artificial trace species.

Austin and Li (2006) showed that a linear relation exists between the tropical upwelling velocity and the age of stratospheric air in multi-decadal simulations performed with the GFDL (Geophysical Fluid Dynamics Laboratory) coupled chemistry-climate model AMTRAC (Atmospheric Model with Transport and Chemistry). Birner and Bönisch (2011), however, emphasized the importance of the different meaning of these two measures of the BDC strength. The tropical upwelling velocity is calculated from the residual mean meridional circulation and, thus, reflects only the advective part of the overall transport. Besides the advective part, however, two-way mixing processes which may lead to net tracer exchange (Birner and Bönisch, 2011) also contribute to the overall transport. The mean age of air reflects the combined effect of both the mixing contribution and the advective part of the overall transport.

In a confined altitude region between 100 and 10 hPa, the tropical upwelling induces a systematic phase lag in water vapour mixing ratios between the tropopause and the levels above, reflecting the seasonal anomalies in tropospheric water vapour concentrations. This so-called water vapour *tape recorder* effect (Mote et al., 1996) can be used to obtain an additional independent measure of the BDC strength (Schoeberl et al., 2008) in both model and observational data.

The BDC in a changing climate. For a changing climate induced by increasing greenhouse gas (GHG) concentrations, several recent simulations performed with different middle atmosphere resolving climate models predict a strengthening of the BDC (e.g. Butchart et al., 2006; Li et al., 2008; Garcia and Randel, 2008; Karpechko and Manzini, 2012). Observational datasets of mixing ratios of atmospheric trace species used to derive the age of stratospheric air (see Section 3.4 for more details), however, do not support the robust model results. The longest available observational age-of-air time series, covering the period 1975-2005 and obtained from sulphur hexafluoride (SF_6) and carbon dioxide (CO_2) concentrations in the northern mid-latitudes at 24 km (30 hPa) altitude (Engel et al., 2009), indicates a slight decrease in BDC strength. Cook and Roscoe (2009), on the other hand, derived a slight BDC increase from nitrogen dioxide (NO_2) measurements over the Antarctic in 1990-2007. However, the obtained trends in both studies are not significant due to large uncertainties in the measurements, so that the model results cannot be disproved by observational data (Engel et al., 2009).

Monge-Sanz et al. (2012) and Diallo et al. (2012) derived the age of stratospheric air from simulations with chemistry transport models (CTMs) using the new reanalysis dataset of the European Centre for Medium-Range Weather Forecasts (ECMWF), ERA-Interim, as input data. The simulation of stratospheric transport processes shows improved performance in ERA-Interim compared to ERA-40, the previous ECMWF reanalysis dataset. The obtained age-of-air data indicate a BDC decrease (Monge-Sanz et al., 2012), which is significant above 24 km (30 hPa) throughout the northern hemisphere. In the same model, however, the age of air derived from ERA-Interim reflects a slight non-significant BDC increase in the lower stratosphere (below 30 hPa). Generally, the BDC trend obtained from age-of-air data strongly depends on the considered region in the stratosphere, both in CTM simulations with ERA-Interim data (Monge-Sanz et al., 2012; Diallo et al., 2012) as well as in observational datasets (Stiller et al., 2012). The BDC trend directly inferred from ERA-Interim via the tropical upwelling at 70 hPa indicates a significant BDC increase of roughly 5% per decade, which is, however, considered to be unreliable due to the inconsistent temperature trend in ERA-Interim (Seviour et al., 2012).

Following Birner and Bönisch (2011), Bönisch et al. (2011) investigated the trend in the advective part of the overall transport over the last 30 years by using the concept of residual circulation trajectories, which was originally described by Rosenlof (1995). They separated the residual circulation, representing the advective part of the overall transport, into a shallow and a deep branch. For the shallow branch, which is primarily associated with synoptic and planetary-scale wave breaking in the subtropical lower stratosphere, they found that different observational datasets indeed indicate a steady strengthening, reflected by a decrease in transit times of roughly 1 month/decade. The strength of the deep branch, more associated with planetary waves breaking in the middle to upper stratosphere, remains unchanged.

Implications of BDC changes. Changes in the strength and pattern of the BDC would have direct implications for the adiabatic heating and cooling. Besides this direct impact on the temperature, BDC changes are also expected to modify the stratospheric composition (Butchart and Scaife, 2001). Particularly, a modification in transport of ozone itself and ozone-depleting substances, such as chlorofluorocarbons (CFCs), would alter the stratospheric ozone distribution. For example, Jiang et al. (2007) found that a GHG-induced BDC strengthening leads to a decrease in ozone concentrations in the tropics, and an increase in ozone concentrations in the high latitudes.

Another important stratospheric constituent is water vapour. On the one hand, the tropical upwelling induces a systematic phase lag in the mean water vapour mixing ratios between the tropical tropopause and the levels above (the water vapour *tape recorder*; Mote et al., 1996) and, thus, yields a measure of the tropical upwelling velocity. On the other hand, although the stratosphere is very dry (Brewer, 1949), as only a small fraction of the tropospheric water vapour is transported through the cold tropopause, stratospheric water vapour plays a key role in stratospheric ozone production and destruction cycles. Particularly, Kirk-Davidoff et al. (1999) showed that ozone loss in the Arctic vortex in late winter and spring depends critically on the water vapour concentrations. An increase in stratospheric water vapour, as indicated by the longest available observational time series (Oltmans et al., 2000) and some other datasets (Rosenlof et al., 2001), would enhance ozone loss in the tropical lower stratosphere (Stenke and Grewe, 2005), and increase the temperature threshold for the formation of polar stratospheric clouds (PSCs) causing enhanced stratospheric ozone loss at high latitudes (Kirk-Davidoff et al., 1999; Tabazadeh et al., 2000).

Both a redistribution of stratospheric ozone as well as a modification of ozone production and destruction cycles would not only yield feedback mechanisms for stratospheric dynamics, but also affect the penetration of UV radiation into the troposphere (e.g. Rind et al., 1990; Hegglin and Shepherd, 2009). So, in summary, in order to improve the accuracy of model simulations with regard to the future evolution of climate and chemical composition of the atmosphere, a good estimation of the change in BDC strength is important.

Drivers of the BDC and its trend. Within the first phase of the Chemistry-Climate Model Validation activity (CCMVal-1; Eyring et al., 2005) the BDC strength and its trend were analysed in many different Chemistry-Climate Models (CCMs) and their underlying General Circulation Models (GCMs). In the second phase of the CCMVal activity (CCMVal-2; Eyring et al., 2008) the results obtained from CCMVal-1, in terms of the BDC driving in the multi-model mean, were corroborated: The resolved waves were found to account for roughly 70% of the driving of the annual-mean total upward mass flux at 70 hPa, while the remaining 30% are largely due to orographic and non-orographic gravity waves (Butchart et al., 2011). However, a wide spread between the models in the contributions from different types of wave drag was obtained. The CCMVal-1 models indicated that also the origin of the trend in the 70 hPa upward mass flux from the troposphere to the stratosphere varies among CCMs (Butchart et al., 2010). In some CCMs the resolved wave drag yields the major contribution, in other models the contribution of unresolved wave drag is predominant. While in the multi-model mean of the GCM Reality Intercomparison Project (GRIPS; Pawson et al., 2000) for the SPARC (Stratospheric Processes and their Role in Climate) programme resolved waves were found to cause 60% of the trend at 70 hPa (Butchart et al., 2006), their contribution is roughly 40% in the multi-model mean of the CCMVal-1 models (Butchart et al., 2010). Since in most of the models involved in these studies, different representations of the stratosphere are used, particularly with regard to the vertical resolution and the vertical model extent, a dependency of the obtained results on the configuration of a model cannot be ruled out. The parameterisation scheme applied in a model to account for the unresolved orographic and non-orographic gravity wave drag is also a possible source for the unequal importance of the parameterised wave drag contribution among the models.

It was argued by Garcia and Randel (2008) that the mechanism responsible for the strengthening of the BDC originates from the GHG-induced increase in tropospheric and decrease in stratospheric temperatures. Via thermal wind balance the increase of the meridional temperature gradient strengthens the upper flank of the subtropical jets and, thus, the conditions for wave propagation are modified. Particularly, the dissipation level of orographic gravity waves is shifted upward (McLandress and Shepherd, 2009). Also the critical layers for resolved wave dissipation on the equatorward side of the jets underlie an upward shift, causing more resolved wave activity to penetrate into the subtropical lower stratosphere (Shepherd and McLandress, 2011).

Deckert and Dameris (2008) found in the E39C CCM (Dameris et al., 2005) the tropical upwelling in the lower stratosphere to increase due to higher tropical sea surface temperatures (SSTs). The increase in tropical SSTs on the summer hemisphere amplifies deep convection locally and, thus, enhances the convective excitation of quasi-stationary waves. In a modified version of the same CCM, Garny et al. (2011) identified the strengthening and upward shift of the subtropical jets as another contributor to the acceleration of the BDC.

Longterm trend and natural variability. In order to derive a robust BDC trend from observational datasets covering only a few decades, it is essential to analyse the natural variability of the BDC. As observational time series are generally too short, comprehensive middle atmosphere resolving climate models, which are capable of realistically simulating the BDC, need to be used to assess the natural BDC variability via multi-decadal and multi-centennial model simulations. Butchart et al. (2000) found decadal variability in the high latitudes of the northern hemisphere stratosphere to overshadow trends derived from their 60-year model integrations. They attributed this decadal variability to internal atmospheric variability, connected with a change in the frequency of sudden stratospheric warmings (SSWs, see Section 1.1.2).

Besides the internal variability of the atmosphere, there are also external factors, which may induce significant longterm stratospheric variability. Kodera and Kuroda (2002) found the 11-year solar cycle to impact the BDC. Schimanke et al. (2011) obtained significant longterm variability in the occurrence of SSWs at a period of 52 years from a multi-centennial simulation with their coupled atmosphere-ocean GCM, coinciding with a signal in the ocean-atmosphere heat flux. A link between low-frequency variations in the stratosphere and the Atlantic thermohaline circulation could also exist (Reichler et al., 2012). The 62-year cycle in proxy records of North Atlantic SSTs (Fischer and Mieding, 2005), the decadal (12-13 year) Atlantic variability, as well as century-scale variability of the tropical Atlantic (Black et al., 1999) also yield potential implications for the stratosphere via vertical coupling processes (see Section 1.1.3). García-Herrera et al. (2006) identified the mechanism responsible for the connection between the El Nino Southern Oscillation (ENSO) and the BDC. They found enhanced vertical propagation of planetary waves during warm ENSO events to force an enhancement of the BDC winter branch. Marsh and Garcia (2007) found stratospheric circulation changes to lag changes in the NINO3.4 index, representing SST anomalies in the central Pacific, by a few months. An alignment of ENSO and solar-cycle signals was found to cause a tropical pacific quasi-decadal oscillation (TPQDO; White and Liu, 2008). Misios and Schmidt (2012) found a TPQDO-like signal also in simulations with constant solar forcing, indicating that there might exist an internal mode of variability with a similar period in their model.

The discrepancy between model results and observational data with regard to the behaviour of the BDC strength in a changing climate is a crucial open question in terms of the validation of comprehensive middle atmosphere resolving climate models. In order to investigate both significance and origin of this discrepancy, a robust estimation of the natural BDC variability is necessary. This is, however, still lacking. The mechanisms involved in the driving of the BDC can - at least to a certain degree - be considered to be understood. However, their relative contribution to the BDC change simulated by the models for a GHG-induced changing climate is still uncertain. In this context, also the impact of the model configuration, in particular the representation of the stratosphere in a GCM, has not yet been systematically investigated.

1.1.2 Extreme stratospheric events

Following the picture of Kodera and Kuroda (2002), in early winter the stratosphere can be considered to be in a rather radiatively controlled state, while in late winter the stratospheric state is more dynamically controlled. In the winter hemisphere, the zonal-mean zonal wind field in the stratosphere is characterised by a strong wind regime, which is referred to as the polar vortex. This wind regime, induced by the combined effects of differential solar heating and the Coriolis force, acts as a transport barrier and prevents air parcels travelling along the pathways of the BDC from reaching the winter pole. The strength of the polar vortex is controlled by the breaking and dissipation of atmospheric waves originating from the troposphere. Due to the large land-sea contrast on the northern hemisphere, fluxes of large-scale waves are generally larger here compared to the southern hemisphere. In extreme cases, anomalously strong wave fluxes can even lead to the breakdown of the vortex, causing the warm air from the middle latitudes to enter the polar region and, thus, triggering the occurrence of a major sudden stratospheric warming (SSW, see Section 3.5.1 for more details) event. These events occur roughly six times per decade in the northern winter hemisphere (Charlton and Polvani, 2007), and exhibit a stratospheric polar cap temperature anomaly of up to 30 K or more (see Section 3.5.1). In some cases, the temperature increase may even exceed 60 K within a few days in a confined latitudinal band in the polar middle stratosphere (e.g. Harada et al., 2010). On the southern hemisphere, these events are extremely rare. So far, only one SSW event was detected here, which took place in 2002 and is often referred to as the *ozone hole split* (Varotsos, 2002).

The stratospheric temperature increase and anomalous stratospheric winds associated with an SSW event were first discovered by Scherhag (1952). In an early modelling study of the interaction of vertically propagating waves with zonal winds the main mechanisms responsible for the occurrence of an SSW event were already described (Matsuno, 1971). Tung and Lindzen (1979) found planetary wave (PW) numbers 1 and 2 to be the main contributor to the drag, which decelerates the polar night jet and, thus, triggers an SSW event. A particularly large contribution of PW number 1 coincides with a displacement of the polar vortex off the pole as well as an elongation of the vortex. SSW events with relatively large contributions of PW number 2 are characterised by a vortex split. There are different ways to distinguish between these two types of events. An algorithm compiled by Charlton and Polvani (2007) uses the absolute vorticity for the classification of an SSW event, and was applied to both ERA-40 and NCEP/NCAR reanalysis data. The results of their method indicate dynamical differences between a vortex displacement and a vortex split, and showed that state-of-the-art GCMs are capable of simulating the dynamics required to produce SSWs realistically (Charlton et al., 2007). Matthewman et al. (2009) found these two types of SSWs to have a distinctive vertical structure. Another algorithm (Bancalá et al., 2012) classifies SSW events as vortex splits or displacements by analysing the preconditioning of an SSW event. It compares the amplitudes of PW numbers 1 and 2 during the onset of an event. The first sign of a mesospheric precursor to an SSW event was found by Quiroz (1969), who discovered a mesospheric cooling preceding an SSW event. The mechanisms involved in this cooling of the mesosphere were explained by Holton (1983).

A measure for the stability of the polar vortex is the Northern Annular Mode (NAM) index on the northern hemisphere, and the Southern Annular Mode (SAM) index on the southern hemisphere. SSW events coincide with negative anomalies in the NAM/SAM index (Limpasuvan et al., 2004), while positive index anomalies reflect time periods of an anomalously strong polar vortex. If the polar vortex is stable for a long time period during the winter, ozone-depleting substances (such as CFCs) effectively reduce the amount of ozone under the cold conditions in the center of the polar vortex. In the southern hemispheric polar vortex this leads to the occurrence of an ozone hole every year at the end of the winter. On the northern hemisphere long periods of a stable polar vortex are rare, however, in these cases severe ozone loss, such as in spring 2011, occurs also over the Arctic (Manney et al., 2011).

External factors, such as the ENSO phase, the solar cycle, and the quasi-biennial oscillation (QBO) of the zonal-mean zonal winds in the equatorial stratosphere, are suggested to have an influence on the occurrence frequency of SSW events. For example, Holton and Tan (1980) found that the easterly phase of the QBO is often associated with a warm and weak stratospheric polar vortex in the northern hemisphere, while the westerly phase coincides with a cold and stable polar vortex. Labitzke and van Loon (1988) concluded that the solar cycle modifies the QBO influence, so that SSWs are more likely to occur under solar minimum conditions. Also Schmidt et al. (2010) found in a modelling study that in late northern hemispheric winter the solar cycle influence on the stratospheric polar vortex significantly depends on the QBO phase. Additionally, van Loon and Labitzke (1987) suggested a connection between ENSO and the occurrence of SSW events.

While it seems that many different processes may play a role in the triggering of an SSW event, single events can have various different origins. Ayarzagüena et al. (2011)

performed case studies for the two major SSW events in 2009 and 2010. By applying a wave flux decomposition method (Nishii et al., 2009) they found the event in 2009 to be caused by strong anomalies associated with planetary wave packets originating from a deep ridge over the Eastern Pacific. On the other hand, for the occurrence of the SSW event in 2010, an ENSO event played an important role.

Reanalysis datasets covering only a few decades do not show a significant change in both the stability of the polar vortex and the occurrence frequency of SSW events, as decadal variability is too large (Charlton and Polvani, 2007). Different model studies contradict each other in terms of the SSW frequency in a GHG-induced changing climate. Mahfouf et al. (1994) found an increase in SSW frequency under doubled CO_2 concentrations, while Rind et al. (1998) found a decrease. Butchart et al. (2000) showed that a change in SSW frequency may just be a manifestation of internal atmospheric variability. This is supported by Schimanke et al. (2011), who found significant multi-decadal variability in the occurrence of SSWs at a period of 52 years. Schimanke et al. (2011) also found significant coherence between the SSW frequency and parameters of the troposphere-surface system, such as snow cover. This suggests a connection between the stratosphere and the tropospheric state during the occurrence of a stratospheric disturbance.

Due to large decadal variability in the frequency of SSW events a potential change in SSW occurrences under a changing climate is hardly obtainable from transient model simulations or observational datasets covering a few decades. In order to detect statistically significant changes in the cause-and-effect relationship of processes involved in the triggering of SSW events in a GHG-induced changing climate, multi-centennial simulations of different climate states with comprehensive middle atmosphere resolving climate models appear to be required.

1.1.3 Stratosphere-troposphere coupling

After Charney and Drazin (1961) investigated the “possibility” that a planetary-scale tropospheric disturbance may propagate into the stratosphere, and found that the effective index of refraction for planetary waves depends primarily on the zonal-mean zonal wind, Matsuno (1970) computed numerical solutions to the linearized equation for wave propagation by assuming a realistic profile of zonal winds. The upward transport of energy via planetary-scale waves from the troposphere to the stratosphere is one of the various dynamical, radiative and chemical processes that are involved in the coupling of the stratosphere and the troposphere.

CO_2 and other GHGs emitted in the troposphere indirectly heat up the troposphere-surface system. However, when they are transported to the stratosphere via tropical upwelling, and follow the transport trajectories of the BDC, they have a net radiative cooling effect in the stratosphere. Thus, the warming effect of $\mathrm{CO_2}$ in the troposphere coincides with radiative cooling due to $\mathrm{CO_2}$ in the stratosphere. A more detailed description of global-scale aspects of stratosphere-troposphere exchange of mass and chemical species can be found in Holton et al. (1995).

Stratosphere-troposphere dynamical coupling is most significant during the weeks before and after the occurrence of an extreme stratospheric event (see Section 1.1.2).

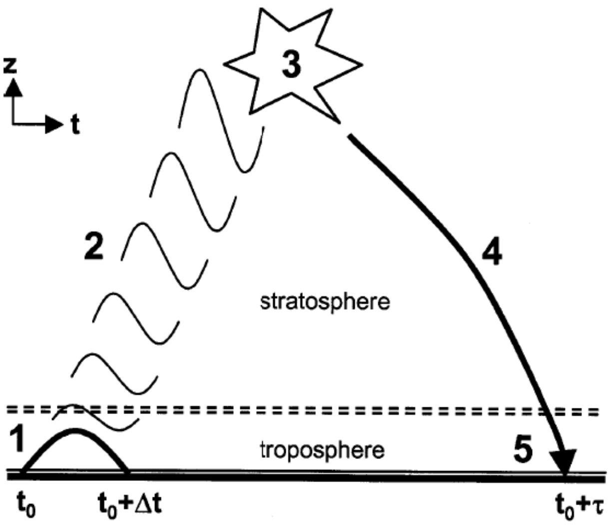

Figure 1.3: A sketch of stratosphere-troposphere dynamical coupling in the course of a weak vortex event is shown. A planetary-wave pulse occurring from time t_0 to $t_0+\Delta t$ (1) propagates upward from the troposphere to the stratosphere (2). Wave dissipation and breaking (3) decelerates the polar vortex, and the stratospheric anomaly propagates downward causing a tropospheric response at time $t_0 + \tau$, where $\tau > 0$. [Figure from Reichler et al. (2005)]

Time periods of anomalously strong (weak) large-scale atmospheric wave fluxes from the troposphere to the stratosphere, initiate weak (strong) stratospheric polar vortex events. Reichler et al. (2005) used a simple GCM to study the response of the coupled stratosphere-troposphere system to planetary wave activity pulses from the troposphere. When the planetary wave pulses dissipate and break in the stratosphere, a zonal-mean circulation anomaly propagates downward (see Fig. 1.3), often reaching the troposphere-surface system at lags of 30-100 days. However, it is important to note that the timescales of the processes involved in stratosphere-troposphere dynamical coupling during extreme stratospheric events vary significantly from case to case. Thus, it is often difficult to determine the exact cause-and-effect relationship and to significantly distinguish between upward and downward coupling processes.

A downward propagation of the stratospheric disturbance after extreme stratospheric events is also visible in the NAM index (Baldwin and Dunkerton, 1999, 2001), which is based on geopotential height. Different definitions of the NAM index (see Section 3.5.2 for more details) are evaluated and compared in Baldwin and Thompson (2009). Smith et al. (2010) investigated the impact of linear interference between the planetary wave response to surface cooling, induced by downward propagating NAM anomalies, and the background climatological wave. If both components are in phase, the wave activity into the stratosphere is amplified causing a negative NAM. If the two components are out of phase, the wave activity flux into the stratosphere is reduced and the NAM response is positive.

Polvani and Kushner (2002) as well as Gerber and Polvani (2009) found a coupling between the strength of the stratospheric polar vortex and the subtropical jets in the troposphere in their GCM. An anomalously strong polar vortex coincides with a shift of the associated tropospheric jet to higher latitudes, while a weak polar vortex is connected with an equatorward shift of the tropospheric jet. During a strong vortex event the shift of the subtropical tropospheric jet to higher latitudes leads to enhanced surface westerlies in the middle latitudes, coinciding with positive surface temperature anomalies. When an SSW event occurs, which is considered as an extreme case of a weak vortex event, the subtropical tropospheric jet is shifted equatorward causing suppressed surface westerlies coinciding with negative temperature anomalies at the surface (e.g. Tomassini et al., 2012). The surface region affected by the stratospheric disturbance depends on where the NAM anomaly reaches the troposphere-surface system. If the negative NAM anomaly (a high-pressure anomaly) propagates downward after a weak vortex event and reaches the Arctic region, the high-pressure anomaly causes the advection of cold air from the north towards lower latitudes coinciding with a negative shift in the North Atlantic Oscillation (NAO, see Section 3.5.3 for more details) index (Jung et al., 2011). In case the high-pressure anomaly, which propagated downward after a weak vortex event, is situated more over Scandinavia or Siberia, it acts as an atmospheric blocking high (Croci-Maspoli and Davies, 2009). During winter, blocking highs can be accompanied with cold spells, e.g., over Europe and Eurasia (Hoskins and Sardeshmukh, 1987), while they are sometimes connected to droughts and heat waves during summer (e.g. Black et al., 2004). In both cases, the westerly flow regime over the North Atlantic is disturbed. Such a disturbance can extend through the entire troposphere. Whether the described connection between SSWs and blocking highs is statistically significant, however, is still under investigation. Taguchi (2008) found no significant connection between these two types of events in the NCEP/NCAR reanalysis dataset when treating all SSW events. On the other hand, Bancalá et al. (2012) found a statistically reliable connection in their coupled atmosphere-ocean GCM. They concluded that Euro-Atlantic blocking highs precede PW number 1 SSWs, while Pacific blocking highs mostly precede PW number 2 SSWs.

The response of the stratosphere-troposphere coupling processes to a changing climate induced by increasing GHG concentrations is also still under investigation. Spangehl et al. (2010) found a shift in the NAO to more positive phases from the Maunder minimum to the present day, and attributed it to the anthropogenic increase in GHGs. It is so far not entirely clear how the representation of the middle atmosphere in a GCM impacts the simulation of stratosphere-troposphere coupling mechanisms. Scaife et al. (2012) emphasized that especially winter regional climate change may be systematically different in climate models that have a good representation of the middle atmosphere compared to those that do not.

Due to the large variation in the timescales involved in stratosphere-troposphere coupling processes during extreme stratospheric events, a potential change in the behavior of stratosphere-troposphere coupling under a GHG-induced climate change is difficult to detect in the relatively short observational datasets. The tropospheric processes affecting the stratospheric state, e.g. by triggering extreme stratospheric events, can be considered to be understood to a certain extent. The significance of the downward propagating stratospheric anomaly after extreme events in polar vortex strength, however, is still under debate. It is also not clear how the cause-and-effect relationship of the processes involved in extreme stratospheric events reacts to a changing climate. In order to detect a potential change in stratospheric dynamics under a changing climate, and in order to assess its impact on the tropospheric state and the other components of the Earth System, long simulations of different climate states with middle atmosphere resolving Earth System Models appear to be necessary.

1.2 Aim and outline of this thesis

In this thesis the response of stratosphere-troposphere dynamical coupling to a changing climate is investigated. The state-of-the-art atmospheric GCM ECHAM6 (see Section 2.1) is used to perform multi-decadal simulations under different stationary climate states, in order to derive the behaviour of the relative contributions of the different mechanisms that drive the stratospheric meridional overturning circulation, the BDC, in a changing climate. The impact of the representation of the stratosphere in ECHAM6 on the simulated BDC and its change under a GHG-induced climate change, is for the first time systematically investigated and quantified by applying different configurations of the same GCM. Both significance and origin of the prominent discrepancy between model results and observational data in terms of the BDC trend are investigated by comparing observed BDC trends with the natural BDC variability derived from a multi-centennial preindustrial control simulation performed with the Max Planck Institute Earth System Model (MPI-ESM, see Section 2.2). The behaviour of stratospheric dynamics and stratosphere-troposphere coupling in a changing climate is studied by analysing MPI-ESM future scenario simulations. It is evaluated how a simulated future change in stratospheric dynamics, reflected by a change in the occurrence frequency of extreme stratospheric events, may affect the troposphere-surface system via stratosphere-troposphere coupling processes.

To validate the results derived from the model simulations, different reanalysis datasets (see Section 2.3), which are considered to provide a good approximation to the real world on the global scale for a large range of altitudes, are used in several sections of this thesis. The model simulations performed and/or analysed in the context of this thesis are described in Section 2.4.

In order to obtain a measure of the strength and pattern of the BDC, which is the main feature of stratospheric dynamics, the residual mean meridional circulation is computed from both model and reanalysis datasets. This residual mean meridional circulation, as formulated by Andrews et al. (1987) in the Transformed Eulerian Mean (TEM) framework (see Section 3.1), is considered to provide a good approximation to the BDC in the middle atmosphere. To evaluate the impact of different types of wave drag on the driving of the BDC, the Eliassen-Palm Flux (Eliassen and Palm, 1961) is calculated, representing the drag originating from the breaking and dissipation of resolved waves (see Section 3.1.2). The downward-control principle (see Section 3.2) is used to compute the contribution of a specific drag term to the BDC. The water vapour tape recorder (see Section 3.3) is evaluated from the model output data to obtain another measure of the tropical upwelling velocity. In order to assess the strength of the global-scale BDC the age of stratospheric air (see Section 3.4) is extracted from the model. By analysing all these measures of the BDC strength in different climate states and model configurations, the behaviour of the BDC and its drivers under a changing climate is quantified together with the impact of the model configuration (see Section

4). The results of this investigation were published already in Bunzel and Schmidt (2013). Several parts of this article are included in different sections of this thesis. Additionally, the natural BDC variability is assessed and compared to present-day and future BDC trends by analysing a set of simulations performed with MPI-ESM (see Section 5). With the obtained natural BDC variability the prominent discrepancy between model results and observational datasets is discussed.

Extreme stratospheric events are well suited to investigate the dynamical coupling between the stratosphere and troposphere, as the stratospheric anomaly involved in these events is large and usually persists for several days to weeks. The definition used for the detection of a sudden stratospheric warming (see Section 3.5.1), an extreme case of a weak stratospheric polar vortex event, follows Charlton and Polvani (2007). To distinguish between vortex splits and displacements an algorithm based on geopotential height was developed in the context of this thesis (see Appendix). A similar version of this algorithm is used in Miller et al. (2013). In order to investigate the occurrence frequency and the tropospheric impact of both weak and strong anomalies in the stratospheric polar vortex (see Section 6.1), the Northern Annular Mode (NAM) index is evaluated for model output data (see Section 3.5.2), and compared to reanalyses. Weak and strong vortex events are separated into downward propagating and non-downward propagating events. The impact of the stratospheric disturbance on the troposphere-surface system (see Section 6.2) is evaluated by deriving the North Atlantic Oscillation index (see Section 3.5.3), which was previously found to be affected by downward propagating NAM index anomalies (e.g. Baldwin and Dunkerton, 1999). ECHAM6 sensitivity simulations combined with the long preindustrial control run as well as future scenario simulations with MPI-ESM, provide a unique set of model simulations to analyse the occurrence frequency of extreme stratospheric events and the behaviour of the ratio of downward to non-downward propagating events in a changing climate. Additionally, these model simulations allow for an investigation of the mechanisms involved in stratosphere-troposphere dynamical coupling, which are still not fully understood.

Chapter 2

Description of models, reanalysis datasets and simulation strategy

The impact of the model configuration on stratospheric dynamics and stratosphere-troposphere coupling in a changing climate is investigated in this study with the stand-alone atmospheric General Circulation Model (GCM) ECHAM6 (see Section 2.1). A set of 9 time-slice simulations, which were performed within this study, was designed to account for different model configurations and climate states (see Section 2.4.1). In order to assess the natural variability of the stratospheric circulation and its drivers, a multi-centennial preindustrial control simulation, conducted with the coupled atmosphere-ocean-land GCM MPI-ESM (see Section 2.2) in the context of the Coupled Model Intercomparison Project 5 (CMIP5, see Section 2.4.2), was analysed. The stationary climate state in the preindustrial control simulation provides a comprehensive basis to assess stratospheric long-term variability and, thus, evaluate the significance of trends derived from both model and observational data. As measurement campaigns usually neither extend over long time periods nor cover several atmospheric layers on a global scale, so-called reanalysis datasets are commonly used to validate the features of the simulated large-scale circulation in global climate models. Thus, the reanalysis datasets relevant for the context of this thesis are also described in the following (see Section 2.3).

2.1 The ECHAM6 General Circulation Model

ECHAM6 (Stevens et al., 2013) represents the sixth generation of the General Circulation Model (GCM) ECHAM. In the horizontal the basic prognostic variables of the model, such as vorticity and divergence, are represented by truncated series of spherical harmonics (Roeckner et al., 2003). In this study the horizontal resolution *T63* (truncation at wave number 63) was used, corresponding to a horizontal resolution of about 1.9° x 1.9°. The model physics are calculated on a grid. Also tracer concentrations, such as the specific humidity, are represented in grid point space.

The vertical model domain follows the orography from the surface up to an altitude of roughly 70 hPa. In this altitude range σ-hybrid coordinates are used, while the model layers above are represented purely by pressure levels. Generally, model simulations with ECHAM6 can be performed with different vertical resolutions and with two different model lids. Climate simulations carried out with older generations of the ECHAM GCM, such as the CMIP3 simulations performed with ECHAM5, were run with a model lid at 10 hPa (*low-top*), while for the recent CMIP5 simulations performed with ECHAM6 a vertical model domain extending upward to 0.01 hPa (*high-top*) was used to resolve the middle atmosphere and to account for a better representation of stratosphere-troposphere coupling processes. In order to internally generate the quasi-biennial oscillation (QBO) of zonal-mean zonal winds in the equatorial stratosphere, the vertical resolution is a crucial parameter. In a model configuration with 95 levels (*L95*) the QBO is successfully generated internally. Details on the features of the QBO generated in the ECHAM6 GCM can be found in Krismer et al. (2013).

The maximum time step of a model simulation is specified considering the combination of horizontal and vertical model resolution, according to the Courant criterion (Courant et al., 1928). The sensitivity of the simulated climate to both horizontal and vertical resolution was studied by Roeckner et al. (2006) for the ECHAM5 low-top GCM. The performance of the middle atmosphere version of the same GCM was analysed by Manzini et al. (2006). Besides the height of the model lid, major changes from ECHAM5 to ECHAM6 comprise the shortwave radiative transfer (Stevens et al., 2013). In ECHAM6 the present-day climate state is at least as well simulated as in ECHAM5, with the most prominent improvements being found in the extratropical circulation. Also the response to increasing GHG concentrations is similar in ECHAM6 compared to ECHAM5. More details on the simulated climate in ECHAM6 can be found in Stevens et al. (2013).

The response of the middle atmosphere to anthropogenic and natural forcings was already comprehensively described in Schmidt et al. (2013). In order to validate in addition the realistic simulation of large-scale wave amplitudes in ECHAM6, the present-day climate state simulated with ECHAM6 is compared to the ERA-Interim (see Section 2.3.1) reanalysis dataset. A realistic simulation of large-scale atmospheric waves is important, as their dissipation and breaking, on the one hand, contributes to the generation of a stratospheric meridional overturning circulation, the Brewer-Dobson Circulation (BDC). On the other hand, it triggers extreme weak polar vortex events in the Northern winter stratosphere, which in extreme cases correspond to sudden stratospheric warmings (SSWs).

Figure 2.1 shows that both the seasonality and amplitudes of planetary wave number 1 at 10 hPa are realistically simulated by ECHAM6 in the present-day climate state. The most prominent difference between ECHAM6 and ERA-Interim data is the larger wave number 1 amplitude obtained from ERA-Interim for the southern late winter. This bias in the southern hemisphere, however, can be considered to have relatively small impact on most of the processes studied in this thesis, such as the occurrence of extreme vortex events in the northern hemisphere.

The climatological-mean planetary wave number 2 amplitudes are shown in Figure 2.2. It is readily apparent that seasonality and amplitudes of wave number 2 are well simulated by ECHAM6 in the present-day climate state. The differences in wave number 2 amplitudes between ECHAM6 and ERA-Interim are equally small on both

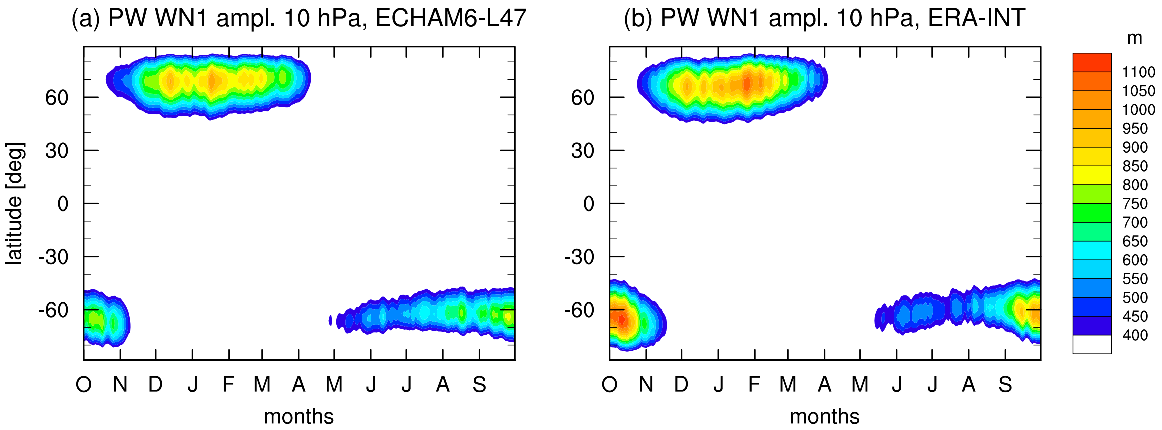

Figure 2.1: The climatological-mean planetary wave number 1 amplitude at 10 hPa is shown. The data was derived from daily-mean geopotential height as simulated in the ECHAM6 GCM for the present-day climate state (50-year time slice) in the T63L47 configuration (a), and as obtained from ERA-Interim reanalysis data (b).

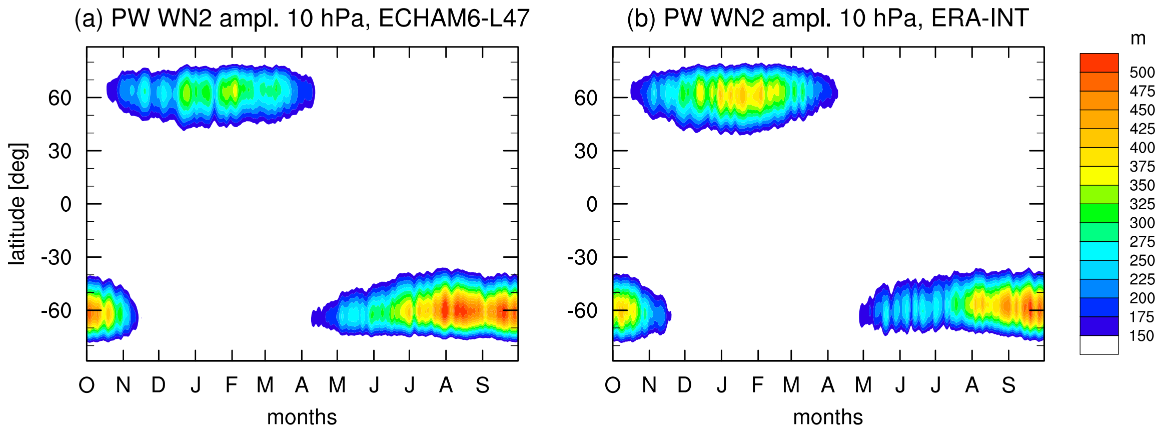

Figure 2.2: The climatological-mean planetary wave number 2 amplitude at 10 hPa is shown. The data was derived from daily-mean geopotential height as simulated in the ECHAM6 GCM for the present-day climate state (50-year time slice) in the T63L47 configuration (a), and as obtained from ERA-Interim reanalysis data (b).

hemispheres. As the state of the northern winter stratosphere is important for most of the processes studied in this thesis, we shall compare in the following the NDJFM-mean amplitude of wave number 1 and 2 in the vertical profile, as simulated with ECHAM6 in the northern midlatitudes, to ERA-Interim data.

The evaluation of planetary wave number 2 amplitudes in the vertical profile (see Fig. 2.3) shows that the amplitudes simulated with ECHAM6 for the present-day climate state are very similar to the associated ERA-Interim reanalysis data from the surface up to the lower stratosphere. In the middle and upper stratosphere both wave numbers investigated exhibit slight deviations from ERA-Interim data. However, as observational data is sparse at these altitudes, it is not entirely clear whether the reanalysis data is more realistic at these altitudes than the ECHAM6 model data.

In order to account for the impact of small-scale atmospheric waves, which are not resolved by the model grid, ECHAM6 uses a gravity wave parameterisation scheme

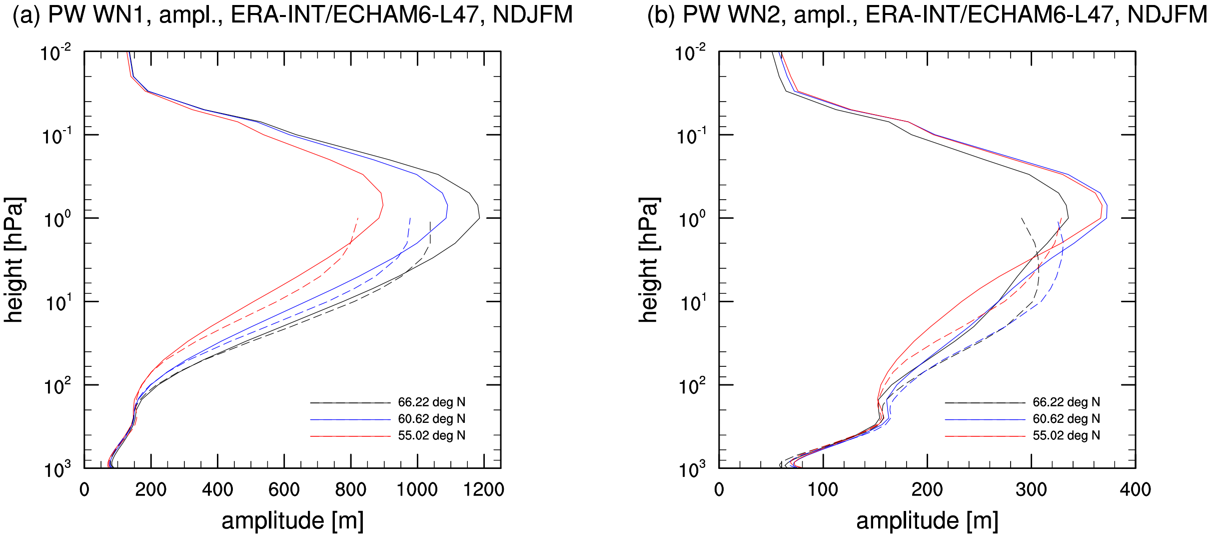

Figure 2.3: The climatological NDJFM-mean planetary wave number 1 (a) and 2 (b) amplitude is shown in the vertical profile. The data was derived from daily-mean geopotential height at three different latitudes, as simulated in the ECHAM6 GCM for the present-day climate state (50-year time slice) in the T63L47 configuration (solid lines), and as obtained from ERA-Interim reanalysis data (dashed lines).

following Lott and Miller (1997). This scheme captures the impact of gravity waves originating from subgrid-scale orography. In the high-top ECHAM6 model configuration, effects originating from non-orographic gravity waves are also accounted for. A parameterisation scheme after Hines (1997) is used.

Special care has to be taken to avoid spurious wave reflection at the model lid. Thus, in all model configurations the momentum carried by the resolved waves is damped into the uppermost 5 model layers (for T63: from 90 hPa upward) by enhancing the horizontal diffusion (Roeckner et al., 2003). While the momentum carried by non-orographic gravity waves is damped into the uppermost layers of the high-top model by setting the momentum flux to zero in the uppermost level, the orographic gravity wave momentum flux is not conserved. More details about the gravity wave parameterisation scheme used in ECHAM6, its differences to ECHAM5, as well as the performance of ECHAM6 (as the atmospheric component of MPI-ESM) with regard to the middle atmosphere can be found in Schmidt et al. (2013).

2.2 The MPI Earth System Model

The Max Planck Institute Earth System Model (MPI-ESM) is a state-of-the-art coupled atmosphere-ocean-land climate model, which constitutes the successor of the well-known atmosphere-ocean GCM ECHAM5/MPIOM (Roeckner et al., 2003; Marsland, 2003). In MPI-ESM the atmosphere, ocean, and land surface are coupled through the exchange of energy, momentum, water, and trace gases (see Fig. 2.4). The atmospheric component, ECHAM6, was extensively described in Section 2.1. The characteristics of the ocean component, the Max Planck Institute Ocean Model (MPIOM; Jungclaus

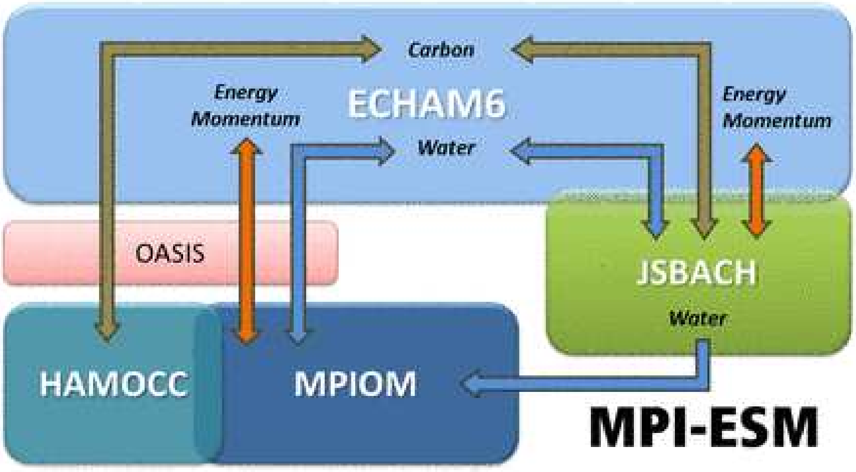

Figure 2.4: A sketch of the interaction between the different components of the Max Planck Institute Earth System Model (MPI-ESM) is depicted. [Figure from the MPI-ESM website (*http://www.mpimet.mpg.de/en/science/models/mpi-esm.html*)]

et al., 2006), are described by Jungclaus et al. (2013). The ocean biogeochemistry is represented by the HAMOCC model (Ilyina et al., 2013), while JSBACH (Raddatz et al., 2007) was used as the land surface component of MPI-ESM. The vegetation cover as well as land-surface albedo in MPI-ESM are evaluated in Brovkin et al. (2013). The different components of MPI-ESM are coupled via the OASIS3 coupling software (Valcke, 2013).

MPI-ESM was used to perform model simulations in the framework of the Coupled Model Intercomparison Project 5 (CMIP5; Taylor et al., 2012), which constitute the German contribution to the 5th Assessment Report of the Intergovernmental Panel on Climate Change (IPCC). In this study CMIP5 simulations (see Section 2.4.2) performed with MPI-ESM in two different model configurations (*LR* and *MR*) are analysed. In the LR (low resolution) model configuration ECHAM6 is run in the T63L47 setup, while for MPIOM a bi-polar grid with 1.5° horizontal resolution and 40 levels in the vertical is used. In the MR (mixed resolution) configuration for ECHAM6 the T63L95 setup, which allows for the internal generation of the QBO, is used, while MPIOM is run on a tri-polar grid with 0.4° resolution and 40 levels.

The changing climate from 1850 to 2100, as simulated in the CMIP5 simulations with MPI-ESM, is investigated by Giorgetta et al. (2012). The response of the middle atmosphere to anthropogenic and natural forcings is analysed in Schmidt et al. (2013). In this study the CMIP5 simulations performed with MPI-ESM are specifically investigated with regard to the strength of the stratospheric meridional overturning circulation, the Brewer-Dobson Circulation (BDC), as well as the occurrence of extreme stratospheric events with the associated downward propagating dynamical disturbances.

2.3 Reanalysis datasets

As it is hardly feasible to carry out observational campaigns covering a long time period with good spatial resolution on a global scale from the surface up to the middle atmosphere, observational datasets are usually not as well-resolved as the model output of global climate simulations. In order to, nevertheless, allow for a comprehensive investigation of global-scale processes and mechanisms also in (a reasonable approximation to) the real world, models are used to extend the existing observational time series to global datasets with high temporal and spatial coverage. These datasets are referred to as *reanalysis* datasets. The reanalysis datasets which are often referred to later in this study - ERA-40, ERA-Interim, and NCEP/NCAR - are described in the following. While the high-resolution state-of-the-art ERA-Interim dataset is particularly useful to validate planetary wave amplitudes in the ECHAM6 model (see Section 2.1) and to assess the quality of the residual circulation simulated in ECHAM6 (see Section 4), the ERA-40 and NCEP/NCAR datasets are valuable to obtain good statistics for the evaluation of the occurrence frequency of sudden stratospheric warmings (see Section 6.1.2), as these datasets cover a particularly long time period.

More details about the available reanalysis datasets can be found at the website of the project *Reanalysis.org - Intercomparison and Observations (http://reanalyses.org).*

2.3.1 ERA-40 and ERA-Interim

The European Centre for Medium-Range Weather Forecasts (ECMWF) 40-year Re-Analysis dataset (ERA-40) extends the former ERA-15 dataset (1979-1993) by covering the period from September 1st 1957 to August 31st 2002. ERA-40 is a 6-hourly dataset produced with the ECMWF Integrated Forecasting System in the T159L60 configuration with a vertical domain extending from the surface to 1 hPa. Satellite datasets were used from 1972 onwards, when the first observational campaigns provided radiometer data. Cloud motion winds were used starting in 1979. Thus, with regard to the middle atmosphere - at least before the 1970s - ERA-40 data can almost entirely be considered to be model data.

The most state-of-the-art ECMWF reanalysis dataset is referred to as ERA-Interim. It extends over a time period from January 1st 1979 until the present day. Compared to the ERA-40 reanalysis, ERA-Interim uses an increased horizontal resolution of T255. Additionally, an improvement was achieved in the model physics. For producing the ERA-Interim reanalysis a similar set of observational datasets as acquired for ERA-40 has been used, complemented by some observational time series covering the later years, which are not included in ERA-40.

All given information on the ECMWF reanalysis products has been acquired from the ECMWF website (*http://www.ecmwf.int*), which the reader is referred to for more details.

2.3.2 NCEP/NCAR

The reanalysis project of the National Centers for Environmental Prediction (NCEP) and the National Center for Atmospheric Research (NCAR) elaborated a reanalysis dataset covering the period from 1948 until the present day by using an analysis and forecast system (Kalnay et al., 1996). The horizontal resolution is $2.5° \times 2.5°$, while in the vertical domain 17 pressure levels distributed between the surface and 10 hPa are used. The temporal coverage is 4-times daily.

More specific information on the NCEP/NCAR reanalysis dataset can be found in Kalnay et al. (1996).

2.4 Simulation strategy

2.4.1 Sensitivity simulations with ECHAM6

The ECHAM6 GCM (Stevens et al., 2013) was used in the time-slice mode to perform sensitivity simulations under stationary boundary conditions for preindustrial (1860), present-day (1990), and future (2050) climate states. For each time slice 50 years were simulated after a spin-up time of 5 years. Associated input data for greenhouse gas (GHG) concentrations (including also CFCs), sea surface temperatures (SST), sea ice coverage (SIC), ozone distribution, and aerosols were applied to simulate the different climate states. For the future time-slice, the RCP4.5 scenario (van Vuuren et al., 2011) was the reference. Both SST and SIC input data were taken from the output of coupled atmosphere-ocean GCM simulations performed with ECHAM5 (Roeckner et al., 2003) coupled to MPIOM (Max Planck Institute Ocean Model; Marsland, 2003), which were carried out for CMIP3. The Special Report on Emissions (SRES) A1B scenario (Nakicenovic and Swart, 2000) was used here to compile input data for SST and SIC fields, as the associated CMIP5 simulations were not completed by the start of the experiments performed in the context of this work.

In order to address the impact of the vertical resolution and the vertical extent of the model, each time-slice simulation was performed in three different model configurations. The high-top model version was used in a low-resolution (47 levels, hereafter: L47) and in a high-resolution mode (95 levels, hereafter: L95). Additionally, all simulations were also performed with the low-top version of the model using 31 levels (hereafter: L31). Up to the tropopause the levels in the L31 configuration are the same as in the L47 model. The Quasi-Biennial Oscillation (QBO) is simulated only in the L95 configuration, where it is internally generated (Krismer et al., 2013). In our simulations the QBO period is roughly 27 months. In all simulations the horizontal resolution is T63 (1.9° x 1.9°).

The mean age of stratospheric air was derived via a passive tracer with linearly increasing concentrations (see Section 3.4), which was initialized at the surface. Following Manzini and Feichter (1999), who calculated the age of air for MAECHAM4, the 110 hPa level at the equator is used as the reference point for the age. In the simulations performed within this study, additionally, the age spectrum is derived via tracer pulses

Table 2.1: An overview about the ECHAM6 50-year sensitivity simulations, performed and analysed in this study, is given.

Model	Climate states	SST / SIC data for future run	GHG / ozone / aerosols for future run
ECHAM6 L95 (high-top)	1860 1990 2050	A1B SRES scenario from ECHAM5/MPIOM (CMIP3)	RCP4.5 scenario (for ozone: climatology over 2045-2055)
ECHAM6 L47 (high-top)	1860 1990 2050	A1B SRES scenario from ECHAM5/MPIOM (CMIP3)	RCP4.5 scenario (for ozone: climatology over 2045-2055)
ECHAM6 L31 (low-top)	1860 1990 2050	A1B SRES scenario from ECHAM5/MPIOM (CMIP3)	RCP4.5 scenario (for ozone: climatology over 2045-2055)

(see Section 3.4). 4 summer and 4 winter tracer pulses were injected in each time-slice experiment to determine the age spectrum of a stratospheric air parcel. Thus, the resulting age spectrum is built from 8 pulsed tracer injections.

2.4.2 CMIP5 simulations with MPI-ESM

Later in this study the CMIP5 simulations performed with MPI-ESM in the LR and MR (see Section 2.2) model configurations are evaluated. The CMIP5 simulations (Taylor et al., 2012) analysed in this study comprise a 1000-year control simulation under stationary preindustrial conditions performed in the LR configuration (500 years in MR), a historical simulation covering the period 1850 to 2005, and future simulations following the RCP4.5 as well as the RCP8.5 scenario (Meinshausen et al., 2011). While the historical period and the near future until the end of the 21st century were simulated with three independent ensemble members in both model configurations, the remote future (2100-2300) was simulated only with one ensemble member in the LR configuration.

The different Representative Concentration Pathway (RCP; e.g. Meinshausen et al., 2011) future scenarios are distinguished by the radiative forcing exerted on the Earth's climate system. Here the radiative forcing describes the change in net irradiance quantified at the tropopause, calculated to occur in response to an imposed perturbation after allowing for stratospheric temperatures to readjust to radiative equilibrium (Ramaswamy et al., 2001). The perturbation may comprise a change in, e.g., the incident solar radiation, greenhouse gas (GHG) concentrations, or aerosols. Thus, the different RCP future scenarios were compiled by assuming the future evolution of anthropogenic emissions of radiatively active gases and aerosols. For example, in the RCP4.5 scenario the radiative forcing exerted on the Earth's climate system at the end of the 21st century is 4.5 W/m^2. The radiative forcing assumed for the different RCP future scenarios is shown more detailed in Figure 2.5.

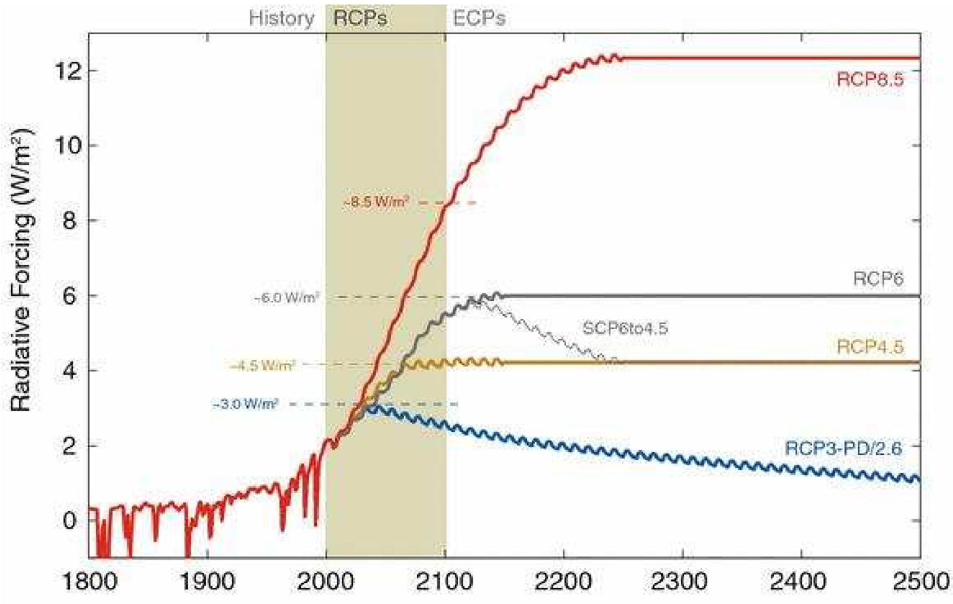

Figure 2.5: The total radiative forcing (anthropogenic plus natural) is depicted for the past and as extrapolated for the different RCP future scenarios. The decadal-scale oscillations reflect the 11-year cycle of the solar irradiance. [Figure from Meinshausen et al. (2011)]

In order to contrast changes in the BDC derived from ECHAM6 model simulations (see Section 2.4.1) and observational time series (e.g. Engel et al., 2009) with the natural BDC variability, the long-term BDC variability is assessed from the multi-centennial CMIP5 preindustrial control simulation performed with MPI-ESM (see Section 5). The transient CMIP5 simulations covering the historical and future periods are investigated to evaluate, particularly, the simulated stratosphere-troposphere dynamical coupling in a changing climate (see Section 6).

Chapter 3

Measures of dynamical stratosphere-troposphere coupling

There are two common methods to describe the dynamics of the middle atmosphere: The transformed Eulerian-mean (TEM) framework and the generalized Lagrangian-mean (GLM) theory. While the TEM formalism comprises averaging over a set of coordinates, the GLM theory involves taking averages along the trajectories of fluid parcels (Andrews et al., 1987). Both methods have advantages and disadvantages. In the TEM framework, the net mass transport in a zonal-mean flow with relatively small wave-like disturbances is well described. For wave-like phenomena of large amplitude the GLM method is more appropriate. However, the practical application of the GLM method can involve several difficulties (Andrews et al., 1987). In this thesis the residual mean meridional circulation is evaluated in the TEM framework (see Section 3.1), as the approximations involved in the TEM theory were found to be mostly applicable. The validity and deficiencies of the TEM theory with regard to its application to climate datasets are assessed in the appendix.

The TEM zonal momentum equation relates the drag originating from different types of atmospheric waves in the middle atmosphere to the induced meridional transport of air parcels. The wave drag resolved by a dataset can be evaluated via the so-called Eliassen-Palm flux (see Section 3.1.2). Other drag terms are associated with small-scale processes exerting a drag on the zonal-mean flow. By applying the downward-control principle (Haynes et al., 1991) the contributions of the different wave drag terms to the residual mean meridional circulation can be separated (see Section 3.1.1).

The vertical velocity calculated via the TEM formalism provides a measure for the strength of the tropical upwelling, which in the lower stratosphere is often used as a measure of the BDC. As especially observational datasets often have sparse spatial coverage, low temporal resolution and large errors, and the average tropical upwelling velocity lies in the order of 10^{-4} m/s, it is important to evaluate also other measures of the BDC. In the tropics, seasonal anomalies in the water vapour mixing ratio are transported from the troposphere to the stratosphere. The tropical upwelling induces a systematic phase lag in the mean water vapour mixing ratios between the tropical tropopause and the levels above, which can be used as another measure for the tropical upwelling velocity and, thus, the BDC (see Section 3.3).

Another type of measure for the strength of the BDC is provided by the age of air (see Section 3.4). While the mean age of air describes the transit time of an air parcel from the tropical tropopause to any location in the stratosphere and above, the age spectrum provides insight into transport and mixing processes.

3.1 The transformed Eulerian-mean (TEM) framework

In order to investigate the dynamical processes taking place in the middle atmosphere, the first necessary step is to derive an appropriate set of equations of motion. Air parcels in the Earth's atmosphere are exposed to the pressure gradient force $\vec{F_p}$ and the Earth's gravitational force $\vec{F_g}$. Additionally, the two fictitious forces, the Coriolis force $\vec{F_C}$ and the centrifugal force, originate from the non-inertial frame of reference represented by the rotating Earth. The equations of motion in the rotating system are then described by the following set of first order partial differential equations:

$$\frac{d\vec{v}}{dt} = \underbrace{-2\,\vec{\Omega} \times \vec{v}}_{\vec{F_C}/m}\; \underbrace{-\frac{1}{\rho} \cdot \vec{\nabla} p}_{\vec{F_p}/m}\; \underbrace{-\,\vec{\nabla}\Phi}_{\vec{F_g}/m}\ , \tag{3.1}$$

$$\text{with} \quad \frac{d\vec{v}}{dt} = \frac{\partial \vec{v}}{\partial t} + (\vec{v} \cdot \vec{\nabla}) \cdot \vec{v}\ . \tag{3.2}$$

The Earth's angular velocity is described by $\vec{\Omega}$, while t is time, and $\vec{v}$, m, ρ, p, and Φ represent velocity, mass, density, pressure, and geopotential of an air parcel, respectively. The centrifugal force is not accounted for, since in the middle atmosphere it is generally small compared to the component of the Earth's gravitational force, which points in the opposite direction. After division by mass Equation 3.1 gives the Euler equations of motion for a fluid exposed to the Earth's gravity field, which represent a special case of the Navier-Stokes equations, as both viscosity and thermal conductivity are neglected.

For the study of middle atmosphere dynamics it turns out to be beneficial to use a spherical coordinate system. A sketch of the most commonly used coordinate system for this purpose is given in Figure 3.1. It is important to emphasize here that this coordinate system differs from the standard spherical coordinate system used in many physical applications. The coordinate axes represent longitude (λ), latitude (ϕ), and height above the Earth's surface ($z' \equiv r - a,\ a$: Earth radius). With the unit vectors $\vec{i}, \vec{j}, \vec{k}$ being directed eastward, northward, and upward, respectively, the relative velocity can be expressed as

$$\vec{V} \equiv u\vec{i} + v\vec{j} + w\vec{k}\ , \tag{3.3}$$

with the components

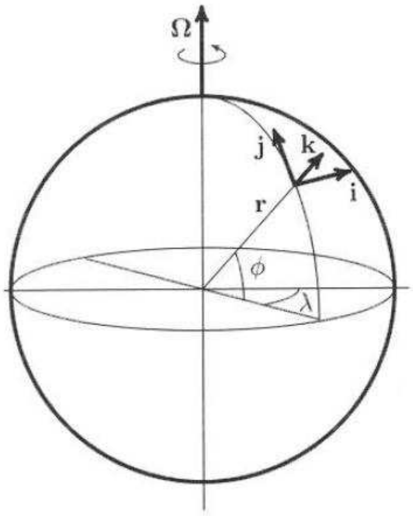

Figure 3.1: A sketch of the spherical coordinate system, used to describe middle atmosphere dynamics, is shown. The coordnate axes represent longitude (λ), latitude (ϕ), and height above the Earth's surface ($z' \equiv r - a, a$: Earth radius), respectively. The unit vectors are $\vec{i}, \vec{j}, \vec{k}$. The Earth's angular velocity is indicated by Ω. [Figure from Etling (2002)]

$$u \equiv a \cos\phi \, \frac{d\lambda}{dt} \; , \quad v \equiv a \, \frac{d\phi}{dt} \; , \quad w \equiv \frac{dz'}{dt} \; . \tag{3.4}$$

For the next steps it turns out to be convenient to replace the geometric height z' with the so-called *log-pressure height* z (for more details see e.g. Andrews et al., 1987). The construction of the vertical coordinate z makes use of the hydrostatic equation,

$$\frac{\partial p}{\partial z'} = -\rho g \; , \tag{3.5}$$

where z' represents the geometric height and g is the magnitude of the gravity acceleration ($g \approx 9.81$ m/s^2), as well as the ideal gas law,

$$p = \rho R T \; , \tag{3.6}$$

where T is temperature and R represents the gas constant for dry air ($R \approx 8.31$ J/mol/K). The log-pressure height z is then defined as

$$z \equiv -H \cdot \ln\left(\frac{p}{p_s}\right) \; . \tag{3.7}$$

Here p_s is the mean sea-level pressure ($p_s \approx 1013.25$ hPa), and H is a mean scale height, which is set to a constant value and could be expressed as follows:

$$H = \frac{RT}{g} \; . \tag{3.8}$$

In middle atmosphere studies it is common to use $H = 7$ km, corresponding to a reference temperature of $T_s \approx 240$K (compare Fig. 1.1) with g set to the global average of gravity at mean sea level. Additionally, a *basic density* (Andrews et al., 1987) can be defined as

$$\rho_0(z) \equiv \rho_s e^{-\frac{z}{H}} \quad \text{or} \quad \rho_0 \equiv \frac{p}{RT_s} \; . \tag{3.9}$$

A comprehensive description of the coordinate system used here is given in Holton (1992). With the above assumptions the horizontal components of the equation of motion (Eq. 3.1) in the spherical coordinate system (see Fig. 3.1) can be written as

$$\frac{\partial u}{\partial t} + \frac{u}{a\cos\phi}\,\frac{\partial u}{\partial \lambda} + \frac{v}{a}\,\frac{\partial u}{\partial \phi} + w\frac{\partial u}{\partial z} - \left(f + \frac{u\; tan\phi}{a}\right) v + \frac{1}{a\cos\phi}\,\frac{\partial \Phi}{\partial \lambda} = X \; , \tag{3.10}$$

$$\frac{\partial v}{\partial t} + \frac{u}{a\cos\phi}\,\frac{\partial v}{\partial \lambda} + \frac{v}{a}\,\frac{\partial v}{\partial \phi} + w\frac{\partial v}{\partial z} + \left(f + \frac{u\; tan\phi}{a}\right) u + \frac{1}{a}\,\frac{\partial \Phi}{\partial \phi} \qquad = Y \; , \tag{3.11}$$

$$\text{with} \quad f \equiv 2\;|\vec{\Omega}|\;\sin\phi \tag{3.12}$$

being the Coriolis parameter. The terms X and Y comprise all additional mechanical forcings. The vertical momentum equation is commonly replaced by hydrostatic balance, which writes

$$\frac{\partial \Phi}{\partial z} = \frac{R\Theta}{H}\; e^{\frac{-\kappa z}{H}} \; , \tag{3.13}$$

$$\text{with} \quad \Theta \equiv T \cdot \left(\frac{p_s}{p}\right)^{\kappa} \tag{3.14}$$

representing the potential temperature, and

$$\kappa \equiv \frac{R}{c_p} \; , \tag{3.15}$$

with c_p being the specific heat of air at constant pressure ($c_p \approx 1005.46$ J/kg/K). Together with the continuity of mass,

$$\frac{1}{a\cos\phi}\,\frac{\partial u}{\partial\lambda}+\frac{1}{a\cos\phi}\,\frac{\partial}{\partial\phi}\,(v\cos\phi)+\frac{1}{\rho_0}\,\frac{\partial}{\partial z}\,(\rho_0 w)=0\ , \tag{3.16}$$

and the thermodynamic energy equation (e.g. Andrews et al., 1987),

$$\frac{d\Theta}{dt}=\frac{\partial\Theta}{\partial t}+\frac{u}{a\cos\phi}\,\frac{\partial\Theta}{\partial\lambda}+\frac{v}{a}\,\frac{\partial\Theta}{\partial\phi}+w\frac{\partial\Theta}{\partial z}=Q\ , \tag{3.17}$$

Equations 3.10, 3.11, and 3.13 are also referred to as the *primitive equations.* In Equation 3.17 the term Q is a diabatic heating term, which can be expressed as

$$Q\equiv\left(\frac{J}{c_p}\right)\ e^{\frac{\kappa z}{H}}\ , \tag{3.18}$$

where J represents the diabatic heating rate per unit mass.

In this form the primitive equations account for the atmosphere as a shallow envelope of compressible gas surrounding a spherical rotating Earth.

3.1.1 The residual mean meridional circulation

In order to quantify stratospheric dynamics and transport it is a common method to compute the residual mean meridional circulation, which is a good approximation to the Brewer-Dobson Circulation (BDC, see Section 1.1.1), the stratospheric meridional overturning circulation. The first step is to derive the Eulerian-mean of the primitive equations (Eqs. 3.10, 3.11, 3.13, 3.16, 3.17) by taking the zonal mean on both sides of the equations after separating all variables into the zonal mean,

$$\overline{A}(\phi,z,t)=\frac{1}{2\pi}\int\limits_0^{2\pi}A(\lambda,\phi,z,t)d\lambda\ , \tag{3.19}$$

and the departure from the zonal mean:

$$A(\lambda,\phi,z,t)=\overline{A}(\phi,z,t)+A'(\lambda,\phi,z,t)\ . \tag{3.20}$$

Due to the zonal averaging, so-called eddy-forcing terms, $\overline{A'B'}$, emerge in the following way:

$$\overline{AB}=\overline{(\overline{A}+A')(\overline{B}+B')}=\overline{\overline{A}\overline{B}+\overline{A}B'+A'\overline{B}+A'B'}=\overline{A}\overline{B}+\overline{A'B'}\ . \tag{3.21}$$

In order to account for both parts of the meridional transport, the transport due to the mean meridional circulation as well as the eddy contribution, meridional and vertical transport velocities $(\overline{v}^*, \overline{w}^*)$ need to be defined. Most commonly the definition is formulated in a way that under certain assumptions (*quasi-geostrophy*, *β-plane* approximation; see Andrews et al., 1987) the eddy-forcing terms in the thermodynamic energy equation would cancel out exactly. In this formulation the meridional and vertical transport velocities are defined as

$$\overline{v}^* \equiv \overline{v} - \frac{1}{\rho_0} \frac{\partial}{\partial z} \left(\rho_0 \frac{\overline{v'\Theta'}}{\frac{\partial \overline{\Theta}}{\partial z}} \right) \ , \tag{3.22}$$

$$\overline{w}^* \equiv \overline{w} + \frac{1}{a \cos\phi} \frac{\partial}{\partial \phi} \left(\cos\phi \frac{\overline{v'\Theta'}}{\frac{\partial \overline{\Theta}}{\partial z}} \right) \ . \tag{3.23}$$

With these definitions a transformed version of the Eulerian-mean primitive equations can be obtained. The so-called transformed Eulerian-mean (TEM) of the zonal momentum equation (Eq. 3.10) and the thermodynamic energy equation (Eq. 3.17) take the following form:

$$\frac{\partial \overline{u}}{\partial t} + \overline{v}^* \left(\frac{1}{a \cos\phi} \frac{\partial}{\partial \phi} (\overline{u} \cos\phi - f) \right) + \overline{w}^* \frac{\partial \overline{u}}{\partial z} = \frac{1}{\rho_0 \ a \cos\phi} \vec{\nabla} \cdot \vec{F} + \overline{X} \ , \tag{3.24}$$

$$\frac{\partial \overline{\Theta}}{\partial t} + \frac{\overline{v}^*}{a} \frac{\partial \overline{\Theta}}{\partial \phi} + \overline{w}^* \frac{\partial \overline{\Theta}}{\partial z} = -\frac{1}{\rho_0} \frac{\partial}{\partial z} \left(\rho_0 \left(\frac{\overline{v'\Theta'}}{a \frac{\partial \overline{\Theta}}{\partial z}} \frac{\partial \overline{\Theta}}{\partial \phi} + \overline{w'\Theta'} \right) \right) + \overline{Q} \ . \tag{3.25}$$

The TEM thermodynamic energy equation (Eq. 3.25) shows that the eddy heat fluxes $\overline{v'\Theta'}$ and $\overline{w'\Theta'}$, together with the diabatic heating $\overline{Q}$, control the change of the potential temperature over time and cause meridional $(\overline{v}^*)$ and vertical $(\overline{w}^*)$ advection of air parcels. In the TEM zonal momentum equation (Eq. 3.24) the combined effect of the eddy heat flux $\overline{v'\Theta'}$ and eddy momentum fluxes $\overline{v'u'}$ and $\overline{w'u'}$, as well as other mechanical forcings $\overline{X}$ cause the change of the zonal mean flow over time and also induce meridional $(\overline{v}^*)$ and vertical $(\overline{w}^*)$ advection of air parcels. Here the eddy heat and momentum fluxes are contained in the term $\vec{\nabla} \cdot \vec{F}$, which represents the divergence of a flux $\vec{F} \equiv (0, F_\phi, F_z)$, the so-called *Eliassen-Palm flux* (EP flux, named after the pioneering work by Eliassen and Palm, 1961). In the above TEM formulation the EP flux takes the following form:

$$\vec{\nabla} \cdot \vec{F} \equiv \frac{1}{a \cos\phi} \frac{\partial}{\partial \phi} (F_\phi \cos\phi) + \frac{\partial F_z}{\partial z} \ , \tag{3.26}$$

with the components

$$F_\phi \equiv \rho_0 a \cos\phi \left(\frac{\partial \overline{u}}{\partial z} \frac{\overline{v'\Theta'}}{\frac{\partial \overline{\Theta}}{\partial z}} - \overline{v'u'} \right) \ , \tag{3.27}$$

$$F_z \equiv \rho_0 a \cos\phi \left(\left(f - \frac{1}{a\cos\phi}\, \frac{\partial}{\partial\phi}(\overline{u}\cos\phi) \right) \frac{\overline{v'\Theta'}}{\frac{\partial\overline{\Theta}}{\partial z}} - \overline{w'u'} \right) . \tag{3.28}$$

In contrast to the Eulerian-mean zonal momentum equation (e.g. Andrews et al., 1987), in the TEM framework the rectified eddy-forcing terms, represented by the divergence of the EP flux, reflect certain basic physical properties of the eddy disturbances. While $\vec{\nabla} \cdot \vec{F} = 0$ if the mean flow is conservative and the eddy disturbances are steady, linear, frictionless, and adiabatic, the eddy-forcing terms in the Eulerian-mean equations are generally non-zero. More details about the characteristics of the TEM framework can be found in Brasseur and Solomon (2005).

When applying the TEM framework to a dataset, the term containing the eddy forcing (the first term on the right hand side of Eq. 3.24), can be considered as the tendency in zonal mean zonal wind induced by atmospheric waves resolved by the dataset. In global datasets, these waves usually comprise large-scale planetary and synoptic-scale waves, and the drag they exert on the mean flow is often referred to as the Eliassen-Palm flux drag (EPFD). The drag originating from other processes, such as small-scale gravity waves, is contained in the term $\overline{X}$. The impact of small-scale processes is usually parameterised in climate models, which enables the user to evaluate the output of each parameterised process separately. In the ECHAM6 GCM the term $\overline{X}$ can be considered to consist of the following contributions:

$$\overline{X} = \overline{X_{OGWD}} + \overline{X_{NGWD}} + \overline{X}^{*} + \overline{X'} . \tag{3.29}$$

$\overline{X_{OGWD}}$ and $\overline{X_{NGWD}}$ contain the contributions of parameterised orographic (OGWD) and non-orographic (NGWD) gravity wave drag. The term $\overline{X}^{*}$ accounts for the damping of resolved wave momentum into the upper model layers, which is performed to avoid wave reflection at the upper boundary of the model (Roeckner et al., 2003). Especially, in the low-top configuration (uppermost level at 10 hPa) of the ECHAM6 GCM this term becomes significantly large, as the momentum carried particularly by large-scale planetary waves is not negligible here (see Fig. 2.3). The term $\overline{X'}$, which represents other forcings such as unspecified horizontal components of friction, is usually small.

The residual mean meridional circulation $(\overline{v}^*, \overline{w}^*)$ can be considered to be driven by the drag terms on the right hand side of Eq. 3.24. This is particularly true in the steady state, where the zonal mean flow $\overline{u}$ does not change over time. The transport velocity components $\overline{v}^*$ and $\overline{w}^*$ can be used to define a “directly calculated” streamfunction $\psi(\phi, z)$ (e.g. Haynes et al., 1991) so that

$$\overline{v}^* = -\frac{1}{\rho_0 \cos\phi}\, \frac{\partial\psi}{\partial z} , \tag{3.30}$$

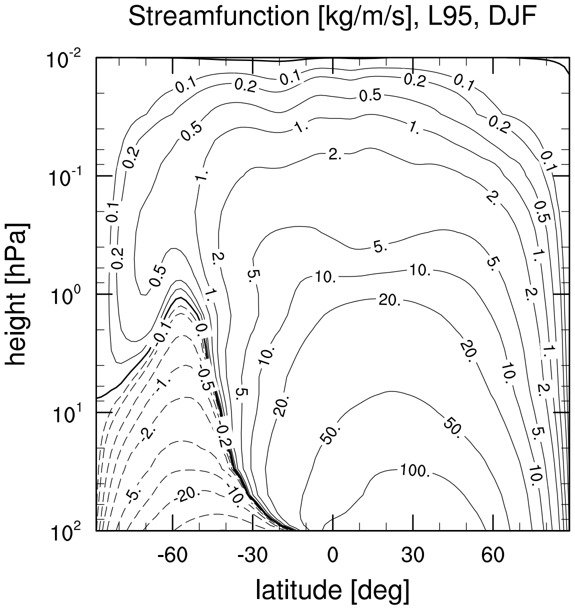

Figure 3.2: The DJF-mean streamfunction $\psi(\phi, z)$ of the residual mean meridional circulation, derived from the 50-year present-day time-slice simulation performed with the ECHAM6 GCM using 95 levels, is presented. Solid lines indicate clockwise movement, while dashed lines indicate counterclockwise movement of air parcels.

$$\overline{w}^* = \frac{1}{a\rho_0\cos\phi}\,\frac{\partial\psi}{\partial\phi}\;. \tag{3.31}$$

An example of such a streamfunction is shown in Figure 3.2. This streamfunction was directly calculated from the output of a 50-year model simulation performed with the ECHAM6 GCM, and is a commonly considered to yield a good approximation to the BDC in the DJF-mean.

3.1.2 The Eliassen-Palm flux

The drag exerted by resolved atmospheric waves on the zonal mean flow is described by the first term on the right hand side of Equation 3.24. This term contains the divergence of the Eliassen-Palm flux (EP flux), which represents the net propagation of wave activity in the atmosphere. Its divergence reflects the magnitude of eddy processes, and describes the transfer of momentum from resolved waves to the mean flow. Additionally, in the quasi-geostrophic approximation, the divergence of the EP flux is proportional to the northward flux of potential vorticity (e.g. Andrews et al., 1987). In this study, however, the original formulation of the EP flux (Eqs. 3.27, 3.28) is used for higher accuracy.

The practical handling of the EP flux and its divergence comes along with a few difficulties (e.g. Edmon et al., 1980). Depicting the EP flux at different levels extending from the troposphere far into the middle atmosphere, involves a broad range of arrow magnitudes. At the same time, the drag exerted by the EP flux divergence, or the

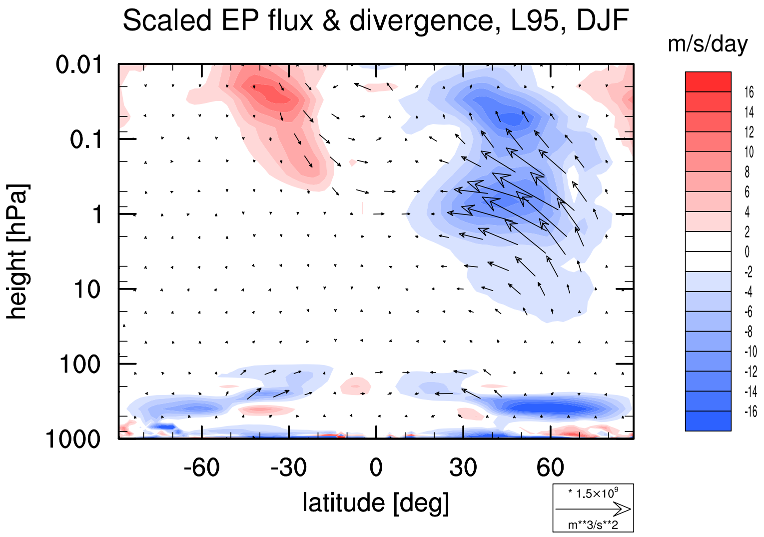

Figure 3.3: The DJF-mean scaled EP-flux is plotted over the drag exerted by resolved atmospheric waves on the zonal mean flow (see text for more information). The data was computed from the 50-year present-day time-slice simulation performed with the ECHAM6 GCM using 95 levels.

resolved atmospheric waves, on the mean flow covers many orders of magnitude less. As the density of the atmosphere decreases roughly exponentially with height (see Eq. 3.9), the dissipation of a certain eddy disturbance has a much smaller impact on the zonal mean flow in the troposphere compared to the middle atmosphere. Thus, in this study the EP flux components (Eqs. 3.27, 3.28) are divided by the density ρ_0, and plotted over the EP flux drag (first term on the right hand side of Eq. 3.24), in order to visualise the EP flux vectors over the contours representing the impact of the EP flux divergence on the zonal mean flow. It is important, however, to emphasise that in this case the contours do not directly reflect the divergence of the arrows. Figure 3.3 shows an example of the described plot depicting EP flux vectors over resolved wave drag contours. The upward propagation of wave activity and subsequent wave dissipation in the middle atmopshere in the DJF-mean is visible.

3.2 The downward-control principle

By using the downward-control principle (Haynes et al., 1991), according to which the meridional circulation at each level is controlled only by the forces acting above it, the streamfunction originating from a certain drag exterted on the mean flow can be derived. In this way the contributions of resolved and parameterised wave drag to the residual mean meridional circulation and thus, the BDC, can be evaluated separately. The resulting expression for the streamfunction derived under the downward-control assumption writes

$$\psi(\phi, z) = \int_z^\infty \left\{ \frac{\rho_0 a^2 \overline{D} \cos^2 \phi}{\overline{\tau}_\phi} \right\}_{\phi=\phi(z')} dz', \tag{3.32}$$

where $\overline{D}$ represents the respective drag term, to be evaluated (Haynes et al., 1991). Above the model lid, the drag terms associated with different wave types are treated differently in the ECHAM6 GCM (see Section 2.1). In order to simplify the calculation of the latitude derivative of the zonal-mean angular momentum $\overline{\tau}_\phi$ along a contour of constant $\overline{\tau}$, the zonal-mean angular momentum is often assumed to be constant with height at extratropical latitudes. However, to improve accuracy $\overline{\tau}_\phi$ is calculated here at every latitude in the lowermost model level, and lines of constant angular momentum are followed by linear interpolation of $\overline{\tau}_\phi$. A comparison to the more simplified approach showed slight deviations in the subtropics and negligible differences at higher latitudes.

The mass streamfunction ψ_m we obtain by

$$\psi_m(\phi, z) = 2\pi a \cdot \psi(\phi, z). \tag{3.33}$$

Following McLandress and Shepherd (2009) and Okamoto et al. (2011), we derive the net upward mass flux through a level z_l by the difference in mass streamfunction at the turnaround latitudes:

$$M_{z_l} = \psi_m(\phi_t^{NH}, z_l) - \psi_m(\phi_t^{SH}, z_l). \tag{3.34}$$

The turnaround latitudes ϕ_t^{NH} and ϕ_t^{SH} on the northern (NH) and southern (SH) hemisphere, respectively, are defined as the latitudes where the residual vertical velocity $\overline{w}^*$ changes sign.

3.3 The water vapour tape recorder

Although only a small fraction of the tropospheric water vapour is transported upward through the cold tropical tropopause, the water vapour remaining in the stratosphere plays an important role in stratospheric dynamics, as it affects the ozone production and destruction cycles (e.g. Kirk-Davidoff et al., 1999). On the other hand, the water vapour entering the lower stratosphere via tropical upwelling allows for an independent estimation of the tropical upwelling velocity and, thus, the strength of the BDC in the lower stratosphere. As seasonal anomalies of tropospheric water vapour concentrations are transported upward through the tropopause, a systematic phase lag in water vapour concentrations between the tropical tropopause and the levels above is observed. This effect is often referred to as the water vapour *tape recorder* (e.g. Mote et al., 1996). Under the assumption of limited horizontal mixing, which turned out to hold in a confined altitude range between 100 and 10 hPa, the systematic phase lag in ascending H_2O anomalies reflected by the water vapour tape recorder, can be used to derive an independent estimation of the tropical upwelling velocity.

Figure 3.4 shows the H_2O tape recorder, as it is simulated by the ECHAM6 GCM with 95 levels in the 50-year time-slice simulation under stationary present-day boundary

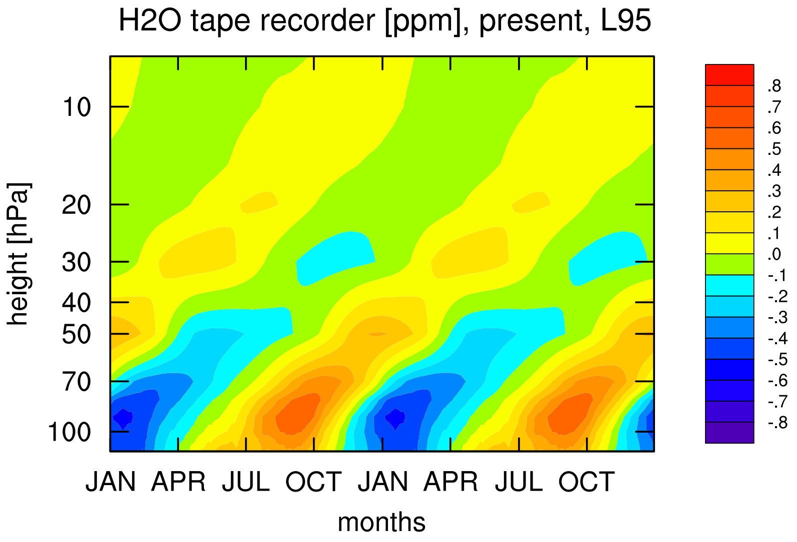

Figure 3.4: The water vapour tape recorder, i.e. the zonal-mean climatological anomalies in specific humidity averaged from 15°S to 15°N, are shown. The data was derived from the model output of the 50-year present-day time-slice simulation performed with the ECHAM6 GCM using 95 levels.

conditions. Following Schoeberl et al. (2008), the tropical ascent rates of H_2O and, thus, the tropical upwelling velocity can now be evaluated by cross-correlating the H_2O concentration anomalies for each level with the level above. The peak in the correlation function reflects the time lag of the anomalies between the two levels, which gives an estimation of the mean upwelling velocity between these two levels. By linear interpolation to the original levels of the data grid, the obtained ascent rates can be compared to the ones calculated via the TEM framework (see Section 3.1). For model data, this method also provides an opportunity to test how realistically tracers are transported through the stratosphere, and to quantify the impact of artificial diffusion effects in a given model configuration.

3.4 The age of air

Using the tracer interface of the ECHAM6 GCM we implemented an approach to derive the mean age of a stratospheric air parcel as well as its associated age spectrum. Following the work of Hall and Plumb (1994), passive tracers were injected during a model simulation, which are transported by the winds and interacting with neither chemistry nor radiation.

In order to obtain the mean age of an air parcel, a tracer with linearly increasing concentrations is injected into the lowermost model level at every grid point between -5 and +5 degrees latitude. The tracer species is then transported by the winds on various BDC pathways with different transit times, before it is recirculated. After an initialisation time of about 20 years, to a good approximation all possible transit times for air parcels are covered, and the tracer circulation can be considered to be in equilibrium.

If the mixing ratio of a conserved tracer, $n = n(P, t)$, is prescribed at the injection point P_0, and $n(P_0, t) = 0$ for $t < 0$, then the tracer mixing ratio at some other point P can be derived by

$$n(P,t) = \int_0^t n(P_0, t - t')G(P, P_0, t')dt', \tag{3.35}$$

where the Green's function $G(P, P_0, t')$ represents the distribution of transit times from P_0 to P, i.e. the age spectrum (Hall and Plumb, 1994). The mean age Γ of an air parcel can then be defined as the average of the component transit times:

$$\Gamma(P, P_0) = \int_0^\infty t \cdot G(P, P_0, t)dt. \tag{3.36}$$

Using a linearly increasing passive tracer, all information on single air parcels is lost, which is due to irreversible mixing processes. The age spectrum $G(P, P_0, t')$ is unknown. If one would neglect the mixing of air parcels in the stratosphere, the Green's function could be replaced by Dirac's delta distribution, $G(P, P_0, t') = \delta(t - t_0)$, where t_0 would represent the transit time of an air parcel from point P_0 to some other point P (Hall and Plumb, 1994). Applying this to Equation 3.36 a measure of the age of air, Γ, in the absence of mixing processes could simply be obtained by the lag time t_0 of tracer concentrations from point P_0 to point P. Hall and Plumb (1994) showed that in the more general case, when stratospheric mixing processes are considered and, thus, the age spectrum of an air parcel has a finite width, this result also holds in the long-time limit for a linearly increasing passive tracer. Figure 3.5 shows that the age of a stratospheric air parcel can be derived in this way from the ECHAM6 GCM. It depicts the zonal-mean concentration of a passive tracer at one grid point in the high-latitude lower stratosphere and the prescribed tracer concentration at the surface. A systematic time lag in tracer concentrations is apparent, which is modulated by an annual cycle originating from the annual cycle in the residual circulation. After an initialisation time of 20 years the time lag in the annual-mean tracer concentration between any grid point in the stratosphere and the prescribed tracer concentrations at the surface turns out to be constant to a good approximation. Thus, after 20 simulated years with a passive tracer initialised, all following years of the simulation can be used to derive the mean age of air.

Although the passive tracer is usually initialised at the surface, the tropical tropopause is commonly used as the reference point for the age of a stratospheric air parcel. As tracers are distributed rapidly within the troposphere, the reference point can simply be set to a certain location close to the tropical tropopause by subtracting the tracer concentration at the reference grid point from any grid point above. Following Manzini and Feichter (1999) we use the 110 hPa level at the equator as the reference grid point to calculate the age of air. The zonal-mean age of air, obtained from all grid points above this reference level in the 50-year present-day time-slice simulation with ECHAM6, is shown in Figure 3.6. The depicted age of air distribution reflects the transport of air parcels along the residual circulation trajectories in a coherent way.

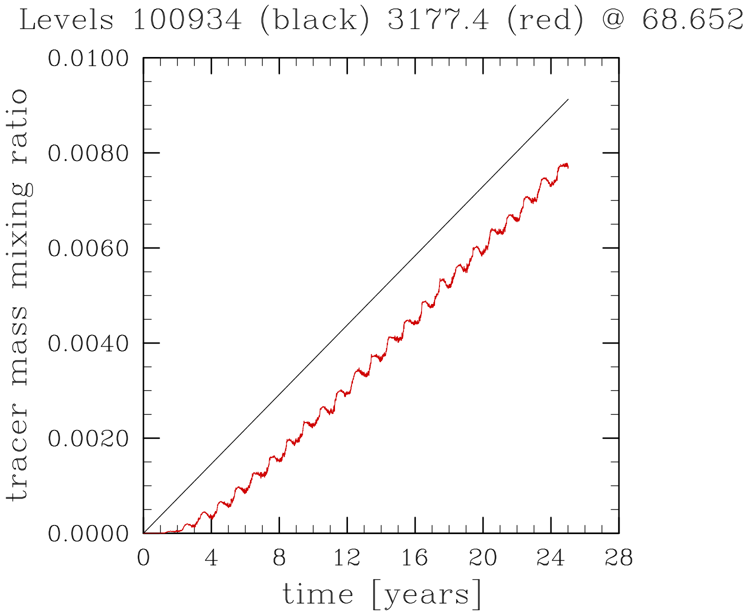

Figure 3.5: The concentration of a passive tracer over time is shown at two different levels at ≈ 69°N in a model simulation performed with an early version of the ECHAM6 GCM under stationary present-day boundary conditions. The time lag between the concentrations can be used to derive the transport time of an air parcel from one grid point to the other and, thus, the age of air.

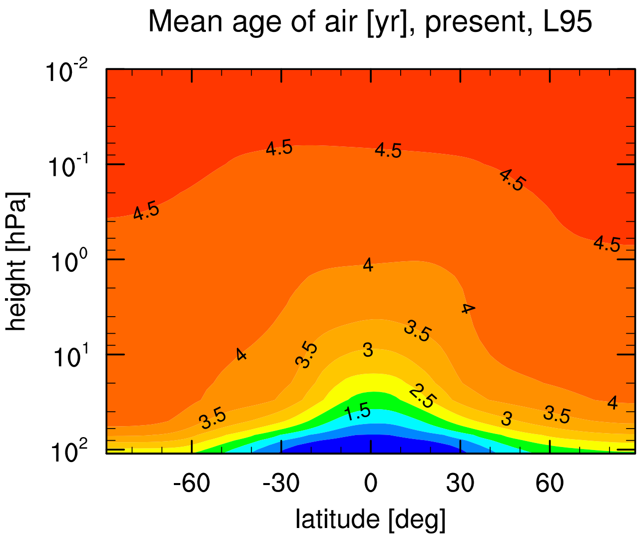

Figure 3.6: The mean transit time of an air parcel originating from the tropical tropopause, i.e. the mean age of air, is shown. As in Manzini and Feichter (1999), the reference grid box is the 110 hPa level at the equator. The data represents the mean over the 50-year present-day time-slice simulation performed with the ECHAM6 GCM using 95 levels.

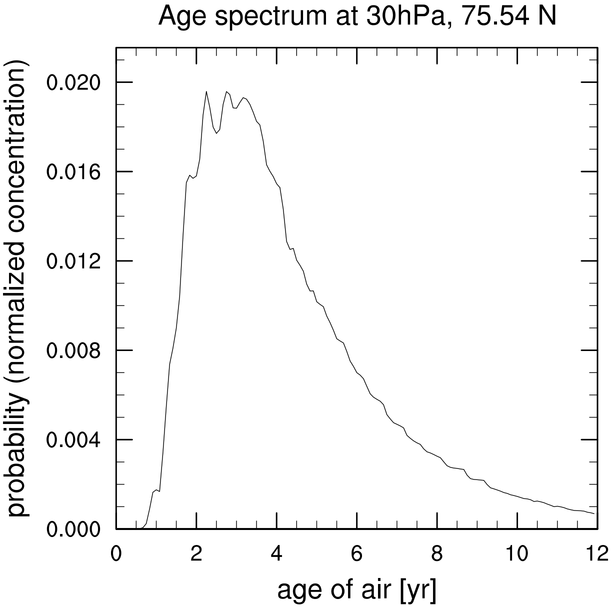

Figure 3.7: The age spectrum of an air parcel located at 30 hPa and 75°N is shown. The data was derived from the 50-year present-day time-slice simulation performed with the ECHAM6 GCM using 95 levels.

Following Hall and Plumb (1994) we derive the age spectrum of an air parcel by injecting a tracer pulse into the model. For a single time step the mixing ratio of a passive tracer is set to 1 at every grid point between -5 and +5 degrees latitude in the lowermost model level. Before and after this time step the mixing ratio is forced to zero at the same grid points. In this way the tracer concentration in the injection grid points simulates a "scaled" Dirac's delta distribution. Applying all this to Equation 3.35 shows that the age spectrum at some grid point P can be obtained by the tracer concentration in that grid point. A certain amount of this tracer pulse escapes the injection grid points between the injection and the following time step. In order to normalise the age spectrum it is divided by the total abundance of the tracer species left in the model at the time step, at which the age spectrum is read out. To account for seasonal differences in transport, one tracer pulse is injected on January 1 and another one on July 1. Every 12 years tracer concentrations are being reset, and a new pulse is injected. By building the mean age spectrum of several tracer pulses, effects originating from possible special atmospheric states can be reduced. Figure 3.7 shows the zonal-mean age spectrum of an air parcel at one grid point in the high-latitude lower stratosphere in the 50-year present-day time-slice simulation with ECHAM6, calculated by using the method described above. The age spectrum peaks at roughly 2.5 years, while the long tail of the spectrum reflects recirculated air parcels with an age of up to the maximum age of 12 years (as tracer concentrations are being reset after 12 years, see above).

3.5 Extreme stratospheric events and downward propagating anomalies

In order to allow for a comprehensive evaluation of the impact of a change in stratospheric dynamics on the troposphere-surface system later in this thesis (see Section 6), a few measures of stratosphere-troposphere dynamical coupling are defined in the following. Although the atmospheric layers above the tropopause can be considered to be important for the troposphere, e.g. by shielding it to a large extent from solar UV radiation, it is not straightforward at all to assume that this relatively small amount of about 20% of the entire atmosphere's mass can also significantly affect the troposphere-surface system dynamically. In case any significant dynamical downward coupling exists between the stratosphere and the troposphere, it can most likely be identified after the occurrence of an extreme stratospheric event in the strength of the stratospheric polar vortex. The strongest of these events almost exclusively occur in the northern winter hemisphere, when the stratosphere evolved from a more radiatively controlled to a more dynamically controlled state (Kodera and Kuroda, 2002). The amplitude of these events is commonly characterised by the change in strength of the stratospheric polar vortex. The polar vortex is the prominent westerly wind regime extending through the entire middle-to-high latitude winter stratosphere (see Fig. 3.8 for the DJF season). It acts as a transport barrier and, thus, in the middle stratosphere prevents the warmer tropical air from reaching the high latitudes (see Fig. 3.9). The most extreme case of a weak polar vortex event is the breakdown of the polar vortex, which coincides with a so-called sudden stratospheric warming (SSW, see Section 3.5.1). During SSW events the absence of the transport barrier leads to a reversal of the temperature gradient from the pole to the midlatitudes. Generally, the index of the Northern (Southern) Annular Mode is a good indicator for the strength of the polar vortex on the respective hemisphere (see Section 3.5.2). After an extreme stratospheric event occurs on the northern hemisphere a stratospheric anomaly in the Northern Annular Mode (NAM) index sometimes propagates downward to the surface, where it can significantly alter the index of the North Atlantic Oscillation (see Section 3.5.3).

3.5.1 Sudden stratospheric warmings

Sudden stratospheric warming (SSW) events represent a prominent feature of the dynamical upward coupling between troposphere and stratosphere. The dissipation and breaking of large-scale atmospheric waves propagating upward from the extratropical troposphere into the stratosphere, causes a deceleration of the polar vortex in the winter stratosphere. As these waves, also referred to as planetary or Rossby waves, are capable to propagate only in a certain range of westerly zonal-mean zonal wind speeds (Charney and Drazin, 1961), they generally do not reach the middle atmosphere in the summer hemisphere (see Fig. 3.8). Moreover, the planetary wave activity reaching the stratosphere in the southern hemisphere is much less, compared to the northern hemisphere, since the large-scale land-sea contrast produces much lower stationary planetary wave amplitudes on the southern hemisphere. This implies that the largest

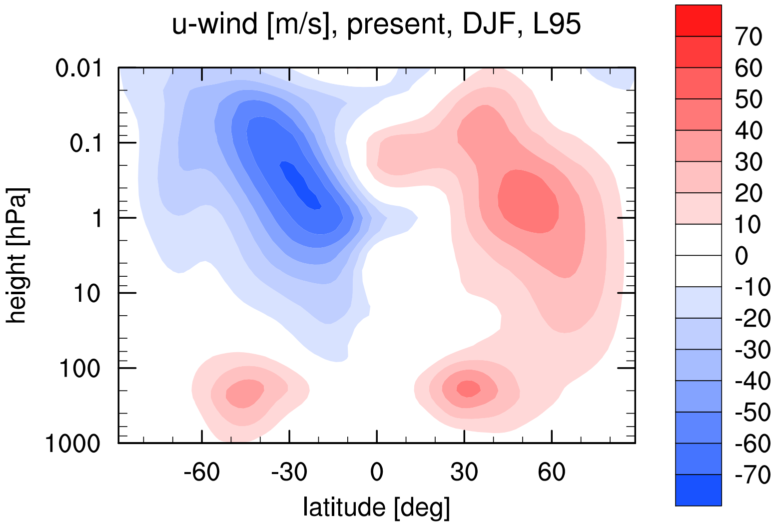

Figure 3.8: The DJF-mean zonal-mean zonal wind field, as derived from the 50-year present-day time-slice simulation performed with the ECHAM6 GCM using 95 levels, is shown.

amount of planetary wave activity reaches the middle atmosphere in northern hemispheric winter. It is in this season when the most extreme stratospheric events occur on the northern hemisphere, the so-called sudden stratospheric warmings. After the definition by the *World Meteorological Organisation (WMO)*, such an event occurs, when the zonal-mean zonal wind at 60°N and 10 hPa turns easterly in the daily mean on any day from November to March, coinciding with a positive zonal-mean temperature gradient from 60°N to the North Pole (Charlton and Polvani, 2007) at 10 hPa on the same day. The event described by this definition is sometimes also referred to as a *major* stratospheric warming (MSW), while a *minor* stratospheric warming describes only the reversal of the temperature gradient without reversal of the polar vortex at 60°N. When we discuss sudden stratospheric warmings (SSWs) in this study, we always refer to major warming events. As sometimes the reversals of the wind and the temperature gradient are separated by a few days, while the dynamical processes acting in the stratosphere are basically the same as during all the other events, we allow also time lags between the reversals of up to 5 days. Additionally, we require 10 consecutive days of westerly winds at 60°N and 10 hPa before a new event can be defined.

SSW events may cause an increase in the polar cap temperature at 10 hPa of up to 30 K or more within a few days. Figure 3.10 shows the zonal-mean zonal wind at 60°N and 10 hPa for one winter simulated with ECHAM6 compared to the climatological year of the 50-year present-day time-slice simulation. The associated polar cap temperature is shown in Figure 3.11. The breakdown of the polar vortex coinciding with a sudden increase in polar cap temperature by about 30 K is readily apparent.

Generally, two different types of SSW events with comparable frequency of occurrence are distinguished. During some events the dissipation and breaking of large-scale waves originating from the troposphere merely causes a displacement of the stratospheric polar vortex off the pole (see Fig. 3.12). In other cases the polar vortex splits up into two or more daughter vortices (see Fig. 3.13). As a vortex displacement reflects a zonal wavenumber 1 pattern, SSW displacement events are sometimes referred to

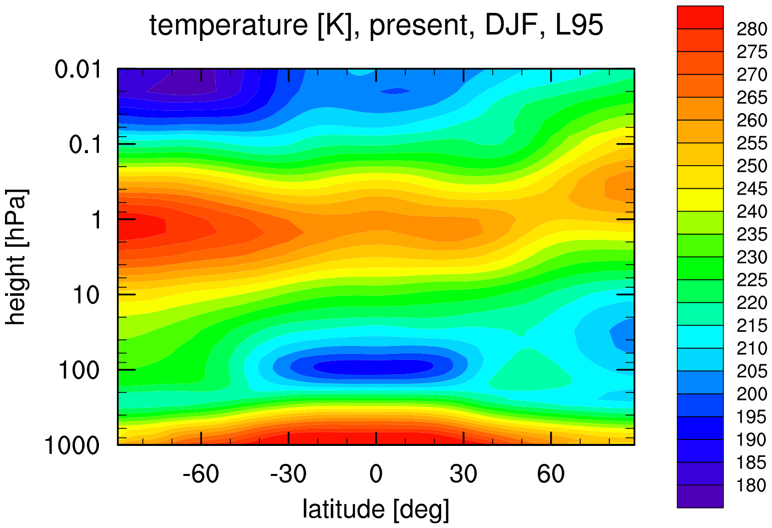

Figure 3.9: The DJF-mean zonal-mean temperature field, as derived from the 50-year present-day time-slice simulation performed with the ECHAM6 GCM using 95 levels, is shown.

as *wavenumber 1 events*. Consequently, vortex splitting events are associated with *wavenumber 2 events*. The dynamical differences between these two types of SSW events were investigated by Charlton and Polvani (2007) by analysing both ERA-40 and NCEP/NCAR reanalyses datasets. They found vortex splitting events to have a stronger impact on the stratospheric state compared to vortex displacement events, while the impact on the troposphere turned out to be largely insensitive to the type of the event. Matthewman et al. (2009) studied the vertical structure of the polar vortex during SSW events, while the capability of different GCMs to simulate the dynamical features of SSWs was investigated by Charlton et al. (2007).

There are different ways to distinguish vortex splitting from vortex displacement SSW events. For example, Charlton and Polvani (2007) use the absolute vorticity on pressure surfaces to compile a classification algorithm comprising a few tunable parameters, which were empirically determined to give the best agreement with a subjective analysis of the 10 hPa fields during an event. Bancalá et al. (2012) calculated planetary wave amplitudes and associate vortex splitting events to large positive wavenumber 2 anomalies. In this study an SSW classification algorithm, based on a more geometric approach involving the 10 hPa field of the geopotential height, was developed. The compiled algorithm is described in the appendix. A similar version of this algorithm was used in Miller et al. (2013).

3.5.2 The Northern Annular Mode

The index of the Northern Annular Mode (NAM) is a comprehensive measure for the strength of the stratospheric polar vortex on the northern hemisphere. While SSWs reflect a prominent feature of the dynamical upward coupling between the troposphere and stratosphere, composite plots of the NAM index after extreme stratospheric events suggest that a stratospheric disturbance could also propagate downward via stratosphere-troposphere dynamical downward coupling. The NAM is commonly

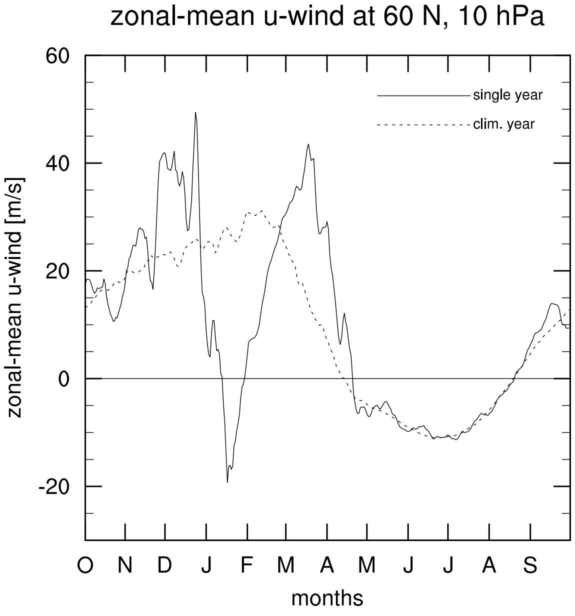

Figure 3.10: The annual cycle of the zonal-mean zonal wind at 10 hPa and 60°N is shown for a single year (solid line) of the 50-year present-day time-slice simulation performed with the ECHAM6 GCM using 95 levels, and the climatological year (dotted line) of the simulation.

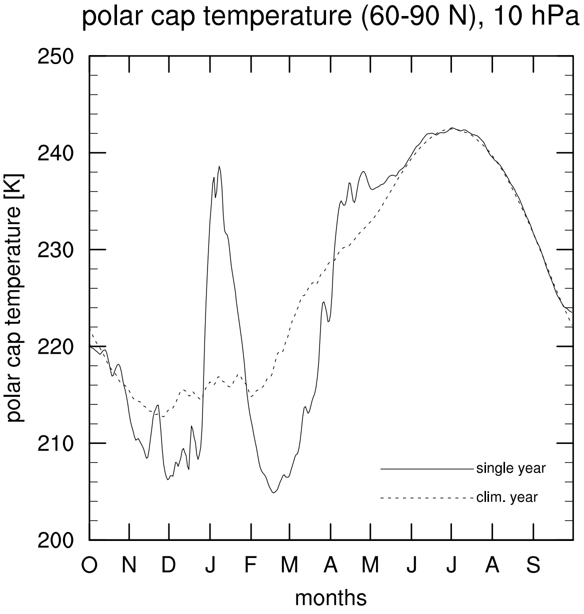

Figure 3.11: The annual cycle of the polar cap temperature is shown for a single year (solid line) of the 50-year present-day time-slice simulation performed with the ECHAM6 GCM using 95 levels, and the climatological year (dotted line) of the simulation.

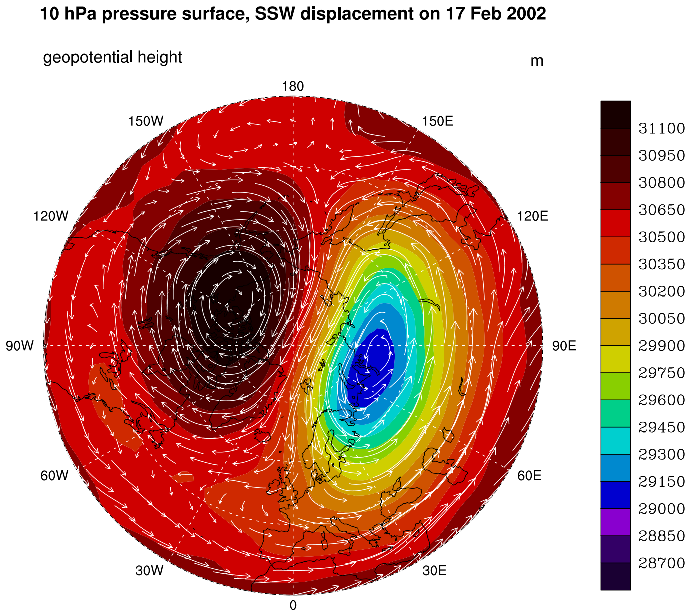

Figure 3.12: The geopotential height (contours, in meters) at 10 hPa on 17 Feb 2002, the central date of an SSW displacement event, is depicted. The arrows indicate the horizontal wind direction. ERA-40 reanalysis data is shown.

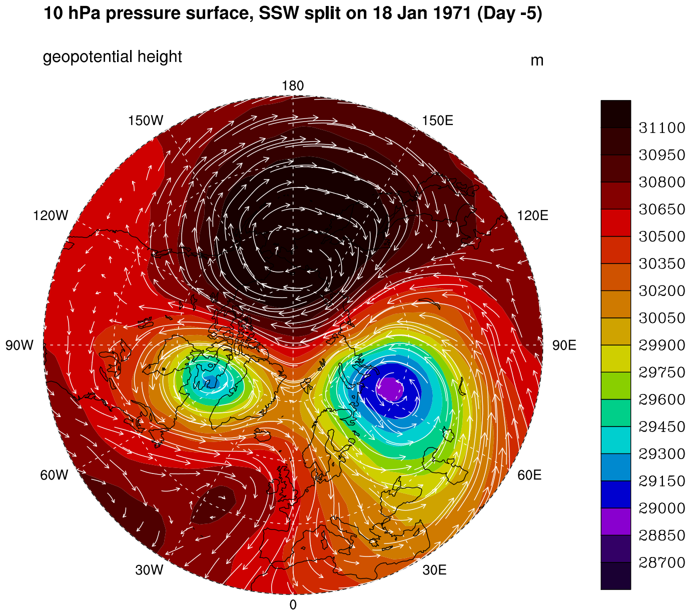

Figure 3.13: The geopotential height (contours, in meters) at 10 hPa on 18 Jan 1971, 5 days before the central date of an SSW split event, is depicted. The arrows indicate the horizontal wind direction. ERA-40 reanalysis data is shown here.

defined as the leading mode of low-frequency variability of geopotential height in the northern hemisphere on a given pressure level. Baldwin and Dunkerton (1999) referred to a downward propagation of the Arctic Oscillation, when they first identified the descent of anomalies in the geopotential from the stratosphere to the troposphere. Baldwin and Dunkerton (2001) built composite plots of weak and strong vortex events, defined by the NAM index exceeding certain threshold values in the lower stratosphere.

There are different ways to define the NAM and the associated NAM index (Baldwin and Thompson, 2009). In this study we use the method of zonal-mean EOFs, which is applied to each level of the data grid separately. Following Baldwin and Thompson (2009) an $(n \times p)$ data matrix Z of year-round zonal-mean geopotential height, which contains n observations in time (here: daily-mean values) at p latitudes on the northern hemisphere, can be expressed as the sum of the products of EOFs $e_1, e_2, ...$ and PC time series $y_1, y_2, ...$:

$$Z = \sum_{i=1}^{r} y_i e_i^{\mathrm{T}} \ . \tag{3.37}$$

Here r is the rank of the data matrix Z. As the EOFs are functions of latitude only, the zonally varying NAM spatial pattern can be obtained by regressing the data matrix Z onto the PC time series:

$$e = \frac{Z^{\mathrm{T}} y}{y^{\mathrm{T}} y} \ . \tag{3.38}$$

Figure 3.14 shows the spatial pattern of the first EOF, i.e. the NAM pattern, as obtained from ERA-40 reanalysis data on the 3 hPa pressure surface. The pattern reflects the polar vortex centered over the north pole by negative anomalies in the geopotential height. A positive value in the associated PC1 time series, i.e. the NAM index, implies an enhancement of this pattern and, thus, a stronger (than average) polar vortex.

The NAM index is represented by y_1 in units of its standard deviation. By calculating the NAM index separately for each level, and building a composite plot of all extreme NAM events occuring at 10 hPa, the downward propagation of a stratospheric disturbance can be visualised (see Fig. 3.15). For the computation of the NAM index, it is common to use an equatorward boundary for the geopotential height field, which is used as an input for the calculation. In this study we set this boundary to 20°N. Baldwin and Thompson (2009) used different positions of this equatorward boundary between 0° and 30°N in order to evaluate its impact on the results. They found, however, the computed NAM index to be largely insensitive to the location of the boundary within this interval. Moreover, in some studies a 90-day low-pass filter was applied to the geopotential height input data, in order to reduce the noise originating from variability on longer timescales. In this study, however, we did not apply any filter, as the filtering did not seem to introduce a significant improvement of the signal.

Downward and non-downward propagating NAM events can be separated, e.g., by

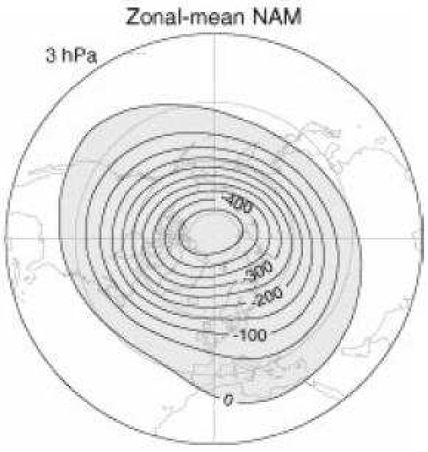

Figure 3.14: The NAM spatial pattern on the 3 hPa pressure surface, derived after the zonal-mean NAM method (Baldwin and Thompson, 2009), is shown. Units are meters of geopotential height. The data shown here was derived from 90-day low-pass filtered ERA-40 reanalysis data. [Figure from Baldwin and Thompson (2009)]

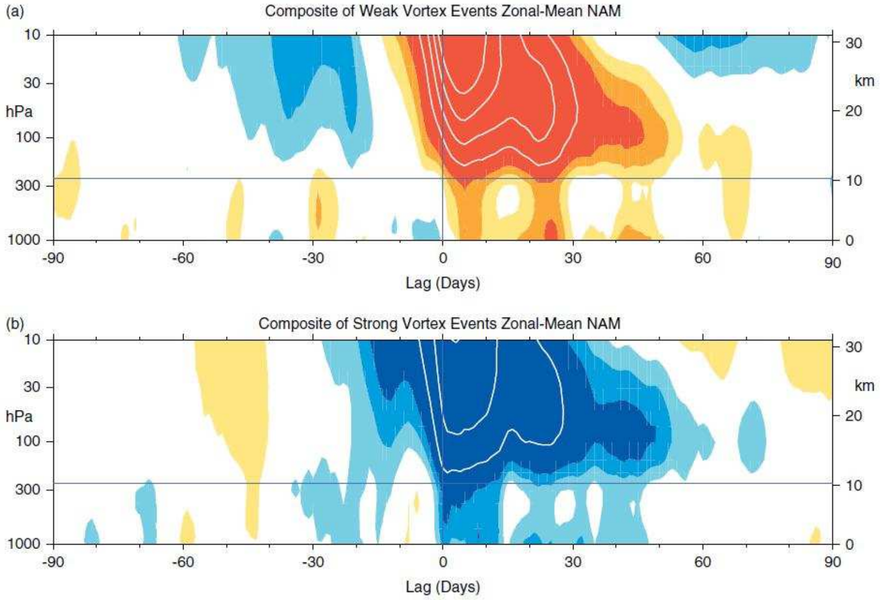

Figure 3.15: The NAM index composite over 29 weak vortex events (a) and 29 strong vortex events (b), derived after the zonal-mean NAM method (Baldwin and Thompson, 2009), is shown. Weak vortex events are here defined to occur, if the NAM index at 10 hPa exceeds -3.0, while the NAM index threshold for strong vortex events was set to 2.0. The contour interval for the colour shading is 0.25, and 0.5 for the white contour lines. Values between -0.25 and 0.25 are unshaded. The thin vertical line indicates the central date of the events, while the thin horizontal line shows the approximate tropopause. The data shown here was derived from 90-day low-pass filtered ERA-40 reanalysis data. [Figure from Baldwin and Thompson (2009)]

introducing a NAM threshold at a tropospheric level, after the initial stratospheric disturbance occurred. In this study, an approach similar to the one of Runde (2012) is used, by considering an extreme NAM event as *non-downward* propagating, if the NAM index at 700 hPa does not exceed +2.0 (or -2.0 for weak vortex events) standard deviations on at least one of the 60 days after the occurrence of the stratospheric disturbance.

3.5.3 The North Atlantic Oscillation

The North Atlantic Oscillation is a prominent pattern of atmospheric circulation variability. Particularly in the DJF season, it reflects a large part of the climate variability in the North Atlantic region, and can be considered as a key climate index for the weather and climate in Europe. Baldwin and Dunkerton (1999) referred to a downward propagation of the Arctic Oscillation (AO) from the stratosphere to the troposphere, when they first identified that downward propagating anomalies in the strength of the polar vortex may significantly alter the northern hemispheric sea-level pressure field. Their definition of the AO index is very similar to the one used by Baldwin and Dunkerton (2001) for the NAM index. As previous studies (e.g. Schnadt and Dameris (2003)) found a high correlation between the surface NAM (or AO) and the NAO, in northern winter the index of the NAO yields a considerable manifestation of stratosphere-troposphere dynamical coupling. Hurrell et al. (2003) point out different methods to derive the NAO index. In some studies the difference in sea level pressure obtained from stations at Iceland and the Azores is used as a proxy for the NAO index. Another common method is to calculate the first EOF and the associated PC1 time series of seasonal mean anomalies in the sea level pressure field averaged over the North Atlantic. In the DJF season the first EOF usually accounts for roughly 37 % of the total variance. In this study, the sea-level pressure anomalies in the region 20°N to 70°N and 90°W to 40°E, as suggested by e.g. Hurrell et al. (2003), are used to perform an EOF calculation. Similarly to the computation of the NAM spatial pattern (see Section 3.5.2), the hemispheric NAO pattern can be obtained by regressing the hemispheric sea-level pressure anomalies on the PC1 time series. Figure 3.16 shows the NAO pattern derived from the DJF means of 100 years of the preindustrial control simulation performed with MPI-ESM. The pattern reflects amplitudes of the DJF-mean sea level pressure variability, and shows a negative pressure anomaly with maximum amplitude over Iceland surrounded by positive pressure anomalies with a peak close to Portugal. This shows that using the difference in sea-level pressure at the stations on Iceland and the Azores to calculate the NAO index would yield similar results. Both the spatial pattern and the variability explained by the first EOF in the MPI-ESM model simulation, are comparable to the NAO inferred from NCEP/NCAR reanalysis data Hurrell et al. (2003). Thus, the pattern of the NAO can be considered to be realistically simulated by MPI-ESM.

The time series associated with the first EOF of North Atlantic sea level pressure anomalies, i.e. the NAO index, is shown in Figure 3.17 in units of its standard deviation. A positive NAO index reflects an enhancement of the associated spatial pattern (see Fig. 3.16), implying an enhanced meridional pressure gradient coinciding with stronger

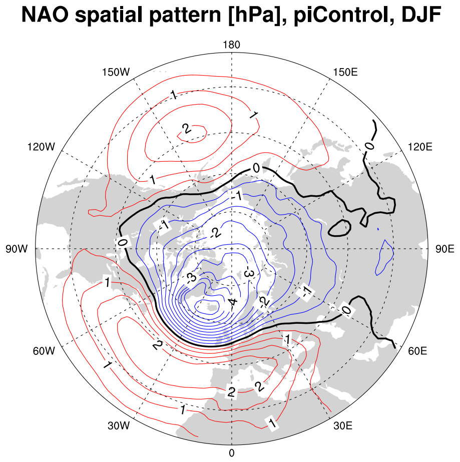

Figure 3.16: The NAO spatial pattern derived from the sea-level pressure field in DJF is depicted (see text for details). The data was computed from model output covering 100 years of the preindustrial control simulation performed with the MPI-ESM model in the MR configuration.

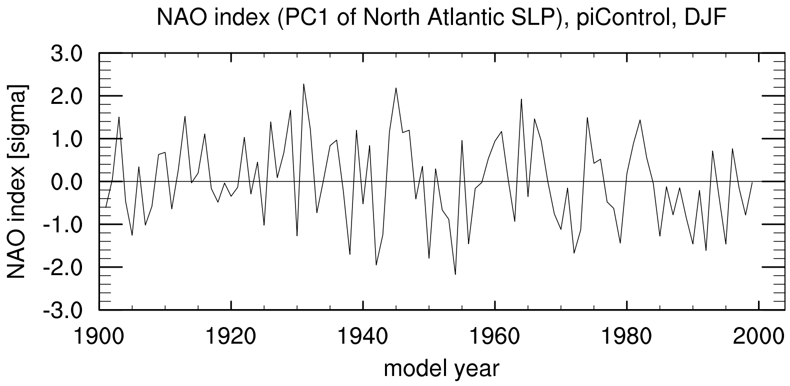

Figure 3.17: The NAO index derived from the sea-level pressure field in DJF is depicted (see text for details). The data was computed from model output covering 100 years of the preindustrial control simulation performed with the MPI-ESM model in the MR configuration.

westerlies over the North Atlantic. As the westerlies over the North Atlantic bring warm moist air to Europe, positive NAO phases coincide with relatively mild winters, particularly over central and northern Europe and Eurasia. On the other hand, during the negative phase of the NAO, the meridional pressure gradient is reduced and, thus, the westerlies over the North Atlantic are suppressed, causing negative temperature anomalies over Europe (e.g. Hurrell et al. (2003)).

Chapter 4

The Brewer-Dobson Circulation: Impact of the model configuration

The Brewer-Dobson Circulation (BDC) represents the stratospheric part of the meridional overturning circulation. On its pathways air masses are transported from the tropics to the middle and high latitudes. A change in the BDC, e.g. induced by a changing climate due to increasing GHG concentrations, would yield direct implications for the adiabatic heating and cooling, but also modify the stratospheric composition (Butchart and Scaife, 2001). Particularly, the distribution of ozone, as well as ozone production and destruction cycles would be affected by a change in the BDC (e.g. Jiang et al., 2007). This would imply not only feedback mechanisms for stratospheric dynamics, but also affect the penetration of UV radiation into the troposphere (e.g. Rind et al., 1990). Thus, in order to improve the accuracy of model simulations in terms of the chemical composition of the atmosphere as well as the future evolution of climate, a realistic simulation of the BDC and its response to a changing climate is important.

The vast majority of the state-of-the-art middle atmosphere resolving climate models predicts a strengthening of the BDC in a changing climate. Observational datasets covering the last 30 years, on the other hand, do not show any significant change in BDC strength (Engel et al., 2009). The driving forces of the BDC, the dissipation and breaking of different types of atmospheric waves in the middle atmosphere, were investigated in several studies with various state-of-the-art climate models. These studies indicate that the origin of the simulated BDC strengthening shows a large spread among the applied models. In some models, the resolved large-scale wave drag yields the primary contribution to the BDC strengthening, in other models the parameterised small-scale gravity wave drag yields the primary contribution. In order to perform for the first time a systematical investigation of the impact of the model configuration on the simulated BDC and its response to a changing climate, we shall evaluate in the following a set of time-slice simulations (see Section 2.4.1) performed with the ECHAM6 GCM in different configurations with regard to the representation of the stratosphere.

All of the applied ECHAM6 model configurations indicate a GHG-induced increase in tropospheric temperature, and a decrease in stratospheric temperature from the preindustrial to the future climate state (see Fig. 4.1a-c for the DJF season). The

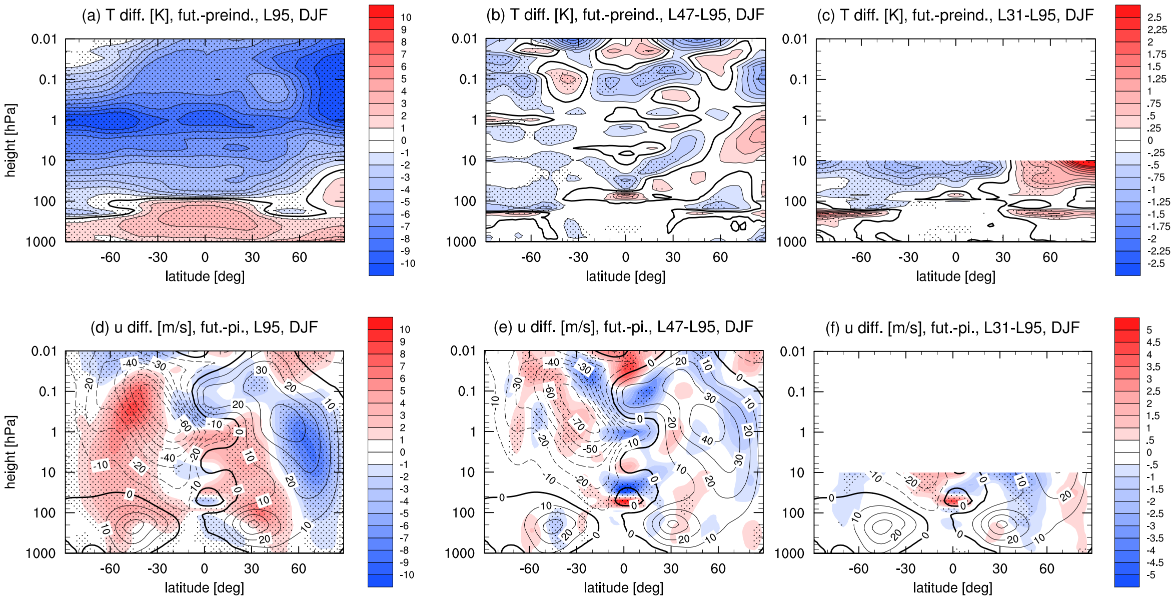

Figure 4.1: The difference in annual mean temperature (a-c) and zonal-mean zonal wind (d-f) between preindustrial and future time-slices, as simulated in the L95 configuration (a,d), is shown. The impact of the model configuration is reflected by subtracting these differences from the associated differences in the L47 (b,e) and the L31 configurations of the model (c,f). Black contour lines in the lower panels show the preindustrial zonal-mean zonal wind field in the L95 configuration. Dotted areas indicate significance at the 95% confidence level after a t-test. Note that the color contours of the plots comparing different model configurations use four (two) times lower values for the temperature (zonal wind) field than the contours of the L95 configuration plot.

temperature change in northern hemispheric (NH) winter is significant at the 95% confidence level (after a t-test) everywhere except for the NH polar lower-to-middle stratosphere. This was also reported by previous studies, e.g. Butchart et al. (2000), who attributed the distinct behaviour of the polar lower-to-middle stratosphere to significant interannual variability resulting from planetary wave forcing from the troposphere. In the ECHAM6 time-slice simulations, the slight temperature increase in this region, which is not significant at the 95% confidence level, could be related to an increasing number of sudden stratospheric warming (SSW) events, as the SSW frequency is found to increase in the future climate state by roughly 50% in both high-top model configurations.

Via thermal wind balance the change in the meridional temperature gradient, which is present in all model configurations (see Fig. 4.1d-f for the L95 configuration), is expected to cause a modification of the zonal-mean zonal wind field. As a response to the latitude dependency of the change in the temperature field, which is prominent especially in the tropopause region, a strengthening of the upper flank of the subtropical jets is simulated in all seasons (see Fig. 4.1d-f for the DJF season). This strengthening was previously reported by several other modelling studies (e.g. Rind et al., 1998; Sigmond et al., 2004; Lu et al., 2008; McLandress and Shepherd, 2009), and is found to be largest in the DJF season in all model configurations. Shepherd and McLandress (2011) argue that the strengthening of the upper flank of the subtropical jets leads to an upward shift of the critical layers for wave dissipation. This would allow more wave activity to penetrate into the subtropical lower stratosphere, inducing a strengthening of the BDC. Garcia and Randel (2008) identified that enhanced wave propagation and dissipation in the subtropical lower stratosphere due to the strengthening of the subtropical jets leads to an acceleration of the BDC.

In the tropics the change in the zonal-mean zonal wind field between preindustrial and future climate states reveals differences in the simulated QBO. As we find that the largest total upward mass fluxes at 70 hPa in NH winter mostly occur when the QBO is in the easterly phase at 30 hPa, differences in the simulated QBO could affect the strength of the tropical upwelling via the Secondary Meridional Circulation (e.g. Plumb and Bell, 1982). Plumb and Eluszkiewicz (1999) argued that the QBO modulation of the tropical angular momentum structure could be significant. During the easterly phase of the QBO, this potentially enhances the tropical upwelling (Semeniuk and Shepherd, 2001).

By comparing zonal-mean zonal wind and temperature changes in L47 and L95 model configurations (see Fig. 4.1), the combined effect of increasing the vertical resolution and the simulation of the QBO, which is generated only in the L95 configuration, can be evaluated. A typical QBO-like pattern is apparent throughout the entire tropical stratosphere. Significant differences in the extratropics in both zonal wind and temperature changes might originate from the Secondary Meridional Circulation, which is induced by the QBO. The meridional gradient in the temperature change is found to be slightly larger in the L47 configuration compared to the L95 configuration of the model, possibly explaining the larger strengthening of the upper jet flank on the NH in DJF (see Fig. 4.1e). This could lead to an acceleration of the meridional circulation. For the strength of the total upward mass flux, however, a modulation of the QBO might have a stronger effect.

The most significant differences in DJF temperature change in the L31 model compared to the L95 model occur in the uppermost model levels, where the horizontal diffusion is artificially enhanced (see Section 2.1). Here the temperature drop from the preindustrial to the future climate state is significantly stronger than in the L95 model except for the northern high-latitudes. With regard to the critical layers for wave dissipation, the weaker change in zonal-mean zonal winds in the L31 model implies a weaker BDC response.

Table 4.1 shows the seasonal total upward mass flux through the 70 hPa pressure surface for the different model configurations. While all models simulate the peak upward mass flux in DJF with a similar magnitude in both high-top configurations, the mass flux is significantly lower (by roughly 25%) in the L31 model in all seasons. Changes in the upward mass flux from the preindustrial to the future climate state (see Table 4.2) reveal an increase in all seasons and model configurations. The L31 model simulates the weakest increase in upward mass flux, which is consistent with the findings of Karpechko and Manzini (2012), who found a stronger response in tropical upwelling under increased GHG concentrations in the ECHAM5 high-top model compared to the low-top configuration. Since in our simulations both the strongest upward mass flux as well as the highest increase in upward mass flux from the preindustrial to the future climate state take place in NH winter, and the wave activity is expected to be the

Table 4.1: The seasonal 70 hPa upward mass flux in the present-day (1990) climate state, derived from time-slice simulations in the L31 model configuration (left), L47 version (middle), and the L95 configuration of the model (right), is presented. Units are 10^8 kg s^{-1}. Numbers in brackets are one standard deviation.

Season	T63L31 (low-top)	T63L47 (high-top)	T63L95 (high-top)
DJF	74.2 (± 3.0)	99.8 (± 3.8)	95.8 (± 3.8)
MAM	60.9 (± 1.8)	77.4 (± 2.4)	75.4 (± 2.7)
JJA	49.9 (± 2.3)	67.1 (± 3.0)	65.4 (± 3.2)
SON	65.6 (± 2.9)	82.4 (± 4.5)	80.5 (± 3.5)
Annual	59.9	76.4	74.1

Table 4.2: The seasonal increase in 70 hPa upward mass flux from the preindustrial (1860) to the future (2050) climate state, derived from time-slice simulations in the L31 model configuration (left), L47 version (middle), and the L95 configuration of the model (right), is presented. Units are 10^8 kg s^{-1}. Numbers in brackets show the relative increase.

Season	T63L31 (low-top)	T63L47 (high-top)	T63L95 (high-top)
DJF	10.1 (14.4 %)	12.7 (13.4 %)	14.9 (16.5 %)
MAM	7.7 (13.2 %)	10.3 (13.7 %)	11.7 (16.3 %)
JJA	6.1 (12.9 %)	8.4 (12.9 %)	8.8 (13.7 %)
SON	6.2 (09.9 %)	7.4 (09.3 %)	8.0 (10.3 %)
Annual	7.1 (12.7 %)	9.5 (12.9 %)	10.7 (15.1 %)

highest on the NH in DJF, the following investigations are focused on the DJF season.

In Figure 4.2 the impact of different types of wave drag on the BDC pattern, studied through the downward-control principle, is evaluated in the L95 model configuration. The directly calculated total circulation pattern of the DJF-mean BDC is similar to the January-mean BDC obtained by Manzini and McFarlane (1998) with MAECHAM4. Also the parameterised gravity wave drag contribution shows the same main features in MAECHAM4 and ECHAM6.

The downward-control streamfunction reproduces the directly calculated streamfunction fairly well (see Fig. 4.2a,b). Only the vertical extent of the summer hemisphere's cell is slightly underestimated. This behaviour is in agreement with the results presented by Okamoto et al. (2011), who applied the downward-control principle to their CCM output data. It is also conspicuous that the stratospheric winter circulation is primarily controlled by EPFD with second-order effects of OGWD. The NGWD mainly controls the mesospheric part of the meridional circulation and, together with the EPFD, builds up the summer upwelling branch in the stratosphere. These findings are in good agreement with ERA-Interim data (Okamoto et al., 2011) on all middle atmospheric pressure levels covered by ERA-Interim.

In Figure 4.3 the age of air, as derived from the different time-slice simulations, is compared to measurements of the age of stratospheric air in the mid-latitudes carried

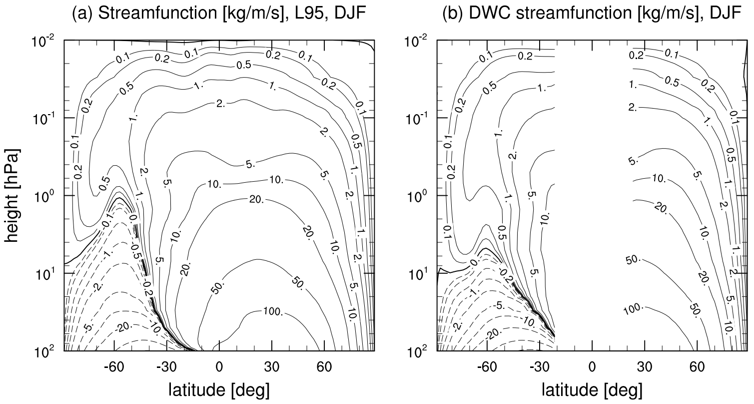
(a) Streamfunction [kg/m/s], L95, DJF

(b) DWC streamfunction [kg/m/s], DJF

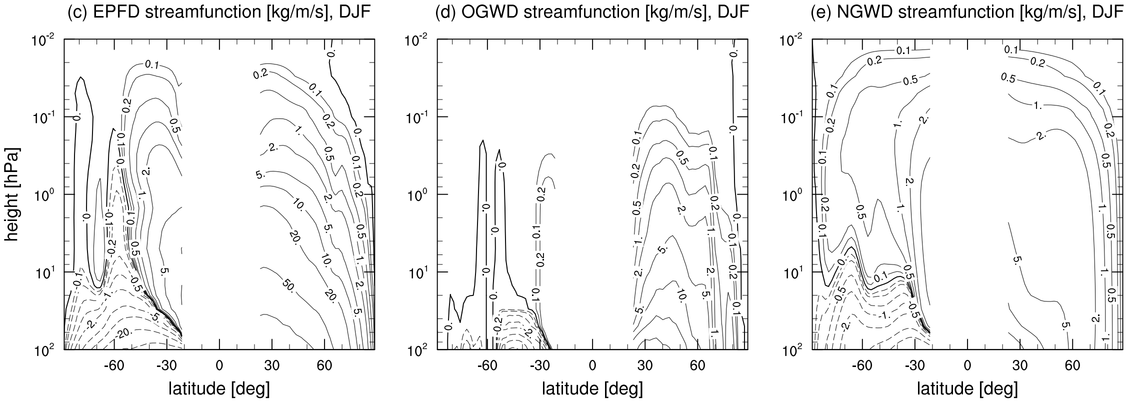
(c) EPFD streamfunction [kg/m/s], DJF

(d) OGWD streamfunction [kg/m/s], DJF

(e) NGWD streamfunction [kg/m/s], DJF

Figure 4.2: The directly calculated mass streamfunction, the downward-control mass streamfunction with combined forcings from all types of wave drag (DWC), as well as the contribution of different wave drags separated via downward control (EPFD, OGWD, NGWD) are presented for the present-day time slice of the L95 model configuration. Tropical latitudes are masked, as the downward-control principle is not applicable here.

out by Engel et al. (2009), which depict the longest available observational time series. In all model configurations the decrease in age of air is relatively small from the preindustrial to the present-day climate state, followed by a more rapid decrease in the future. This behaviour coincides with a weak increase in tropical upwelling in the past, and a stronger increase in the future (not shown), which is roughly in line with the relationship between reciprocal age of air and tropical upwelling found by Austin and Li (2006). The total age of air decrease from the preindustrial to the future climate state is 0.5-0.7 years, depending on the model configuration (see Fig. 4.3). Observational data (Engel et al., 2009) show a slight increase in age of air, however, the uncertainties in measurements are too high to disprove the model results (Garcia et al., 2011).

From Figure 4.3 three main findings with regard to the age of air can be obtained, which we will focus on in the following sections:

1. An offset for different model configurations in all time slices (see Section 4.1),
2. a similar change between the time slices in all model setups (see Section 4.2), and
3. a difference between model and observational data (see discussion in Section 7.1).

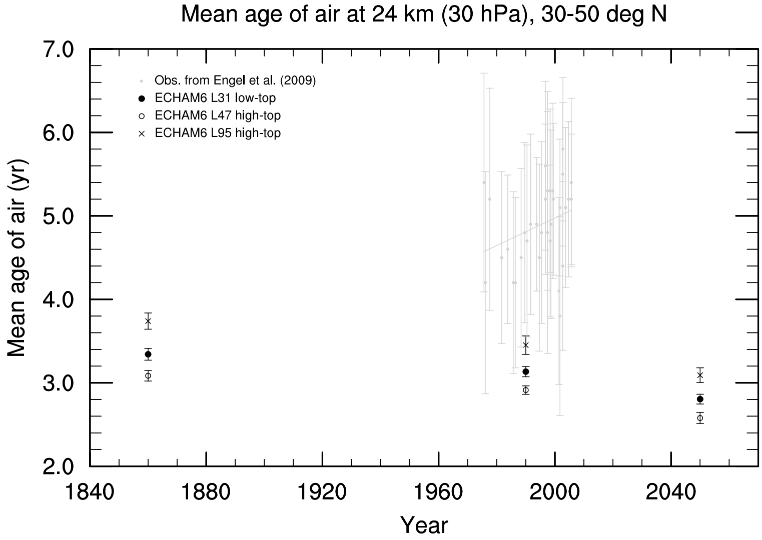

Figure 4.3: Annual-mean age of air as derived from our model simulations is presented together with an observational reference dataset (grey; Engel et al., 2009). Error bars indicate one standard deviation for the model data, and show the total error of the measurements. The solid line shows an unweighted linear regression computed from the observations.

4.1 The BDC as simulated in different model configurations

Figure 4.3 shows that decreasing the vertical resolution in the high-top model from L95 to L47 leads to a difference in age of air of up to 20% in the mid-latitudes. In the L31 model the obtained age of air in this region lies between the values associated with the two high-top model configurations, while the tropical upwelling is 25% slower in the L31 model compared to the two high-top models (see Tab. 4.1).

The present-day mean age of air distribution in the L95 model configuration (see Fig. 4.4a) reveals a comparable structure as the age of air derived from the different CCM simulations in Butchart et al. (2010), and looks similar to the age of air distribution obtained by Manzini and Feichter (1999) with the MAECHAM4 GCM.

The differences in mean age of air distributions between different model configurations are evaluated in Figure 4.4b,c. Both the L47 as well as the L31 present-day time-slice simulations are compared to the same time-slice in the L95 model configuration. In the high-top model decreasing the vertical resolution leads to a decrease in age of air at almost every grid point above the tropopause (see Fig. 4.4b), which makes the BDC appear faster for lower vertical resolution. As the regions of the largest differences are located right above the extratropical tropopause, we attribute the origin of these differences primarily to higher numerical diffusion through the extratropical tropopause in the L47 model configuration due to lower vertical resolution. Additionally, increased recirculation due to higher vertical resolution could also contribute to larger age of air in the L95 model.

For the L31 model significantly older air compared to the L95 model configuration

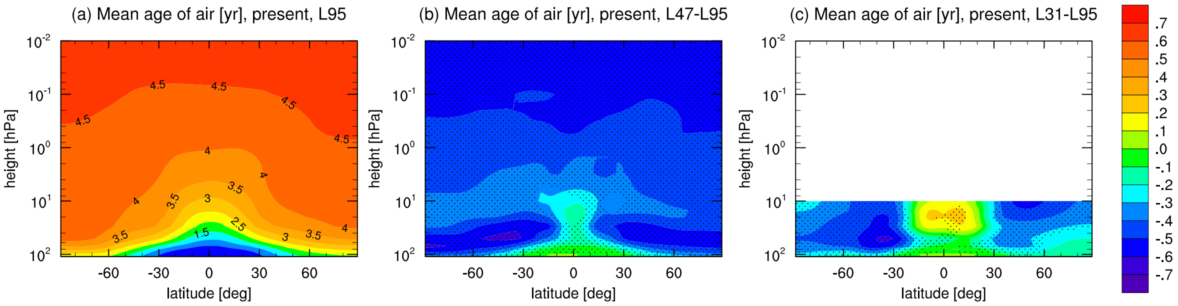

Figure 4.4: Present-day annual mean age of air as simulated in the L95 model configuration (a) is shown together with differences to the L47 version (b), and the L31 configuration (c) of the model. Dotted areas indicate significance at the 95% confidence level after a t-test.

is found in the tropical lower stratosphere (see Fig. 4.4c), indicating a significantly slower tropical upwelling in the L31 model. Regions of significantly younger air in the L31 model, compared to the L95 version, show up above the extratropical tropopause in both hemispheres, which may be the result of strong mixing processes due to the enhanced horizontal diffusion in the L31 model. As in the L47 model, increased numerical diffusion through the extratropical tropopause in the L31 model compared to the L95 configuration might also contribute to these differences.

The differences in mean age of air between the L31 and the high-top configurations are also reflected by the age spectrum. Figure 4.5 shows the age spectrum extracted at the tropical and extratropical stratosphere. The large abundance of young air transported recently from the troposphere to the stratosphere via tropical upwelling is clearly visible in both high-top model configurations. In the mid-latitudes the age spectrum shows a much smoother distribution, which originates from quasi-horizontal transport and mixing (Waugh and Hall, 2002). In the L31 model, however, the age spectrum shows much less difference between the tropical and the extratropical stratosphere (see Fig. 4.5). Here the significantly lower tropical upwelling leads to a relatively larger impact of horizontal transport and mixing already during the ascent of air in the tropics, causing the fresh young air to be distributed to higher latitudes much earlier. In the high-top model, increasing the vertical resolution leads to a slight shift of the age spectrum towards older ages. This shift could reflect both increased recirculation of air and reduced numerical diffusion through the tropopause in the L95 model configuration.

In order to evaluate the impact of the model configuration on the BDC pattern, the present-day residual streamfunctions in both the L47 (see Fig. 4.6) as well as the L31 model (see Fig. 4.7) are compared to the respective streamfunction in the L95 model configuration (see Fig. 4.2). The difference in the directly calculated streamfunction reveals that decreasing the vertical resolution in the high-top model causes an acceleration of the residual circulation in the stratosphere, and a deceleration in the mesosphere. Both EPFD as well as OGWD are identified as the origin of the difference in stratospheric circulation pattern. In the upper stratosphere and mesosphere the difference in the BDC is induced by combined effects of EPFD and NGWD (see Fig. 4.6). In the tropical part of the circulation, differences are particularly likely to be caused by the Secondary Meridional Circulation induced by the QBO.

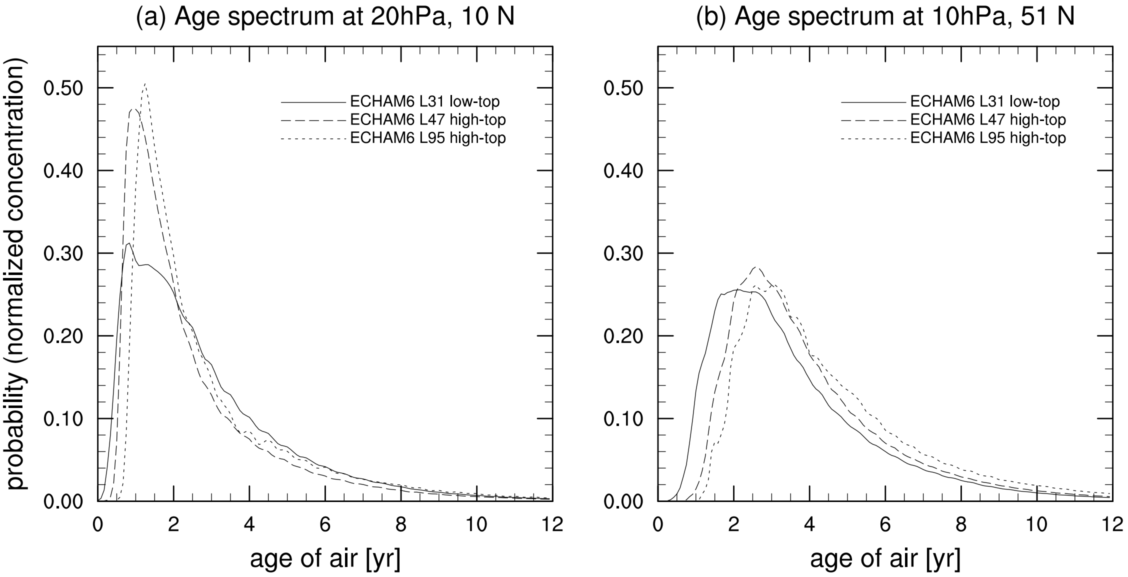

Figure 4.5: Present-day age of air spectra extracted at the tropical (a, 20 hPa, 10 N) and the extratropical stratosphere (b, 10 hPa, 51 N) are shown for all model configurations.

Comparing the BDC pattern in L31 and L95 model configurations, a three-cell structure in streamfunction differences (see Fig. 4.7a) is obtained. Generally, the BDC is slower in the L31 configuration, however, a polar cell shows up in the NH, indicating a faster BDC in the northern high-latitudes. Figure 4.7b also shows that this polar cell does not appear in the streamfunction differences derived via downward control. Both EPFD and OGWD contribute to the weaker BDC at all latitudes in the L31 configuration of the model. As the NGWD is not incorporated into the L31 model, and yields a positive contribution to the BDC in the NH polar stratosphere in the L95 model (see Fig. 4.2e), an additional force must be acting in the L31 model configuration, which cannot be inferred by downward control.

A close-up of the streamfunction on the 70 hPa pressure surface in the L31 model (see Fig. 4.8a) depicts the conspicuous difference between the directly calculated streamfunction and the downward-control streamfunction in the northern high-latitudes. As the impact of the additional force is particularly strong in the uppermost layers of the L31 model, we identify the enhanced horizontal diffusion (see Section 2.1) as the origin of this artificial force. Furthermore, the hemispheric difference in the 70 hPa DJF-mean streamfunction is apparent in all model configurations. In the two high-top models the downward-control principle yields a good approximation to the direct streamfunction at all extratropical latitudes (see Fig. 4.8b,c). Considering that generally the amplitudes of resolved waves are still large at the lid of the L31 model (10 hPa), while there is negligible resolved wave momentum left at the lid of the L47 and L95 models (0.01 hPa), it is coherent that the effect of damping the resolved wave momentum into the upper model layers is much more prominent in the L31 model. Since in the summer hemisphere planetary wave momentum flux is negligible above the middle stratosphere, the difference between the directly calculated streamfunction and the downward-control streamfunction is small also in the L31 model (see Fig. 4.8a). In the northern high-latitudes the difference of the directly calculated DJF-mean streamfunc-

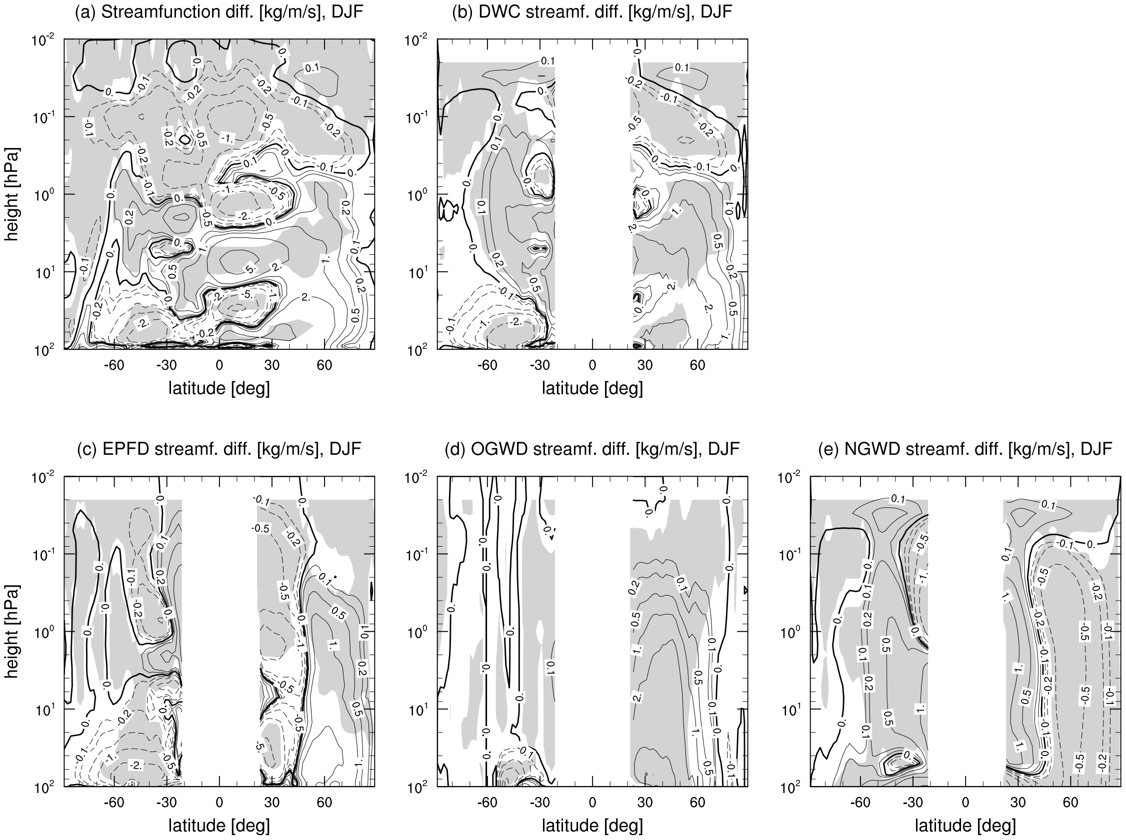

Figure 4.6: Streamfunction difference for the present-day time slice between different vertical resolutions of the high-top model (L47-L95) is shown. The directly calculated streamfunction, the downward-control streamfunction with combined forcings from all types of wave drag (DWC), as well as the contribution of different wave drags separated via downward control are presented (EPFD, OGWD, NGWD). Shaded areas indicate significance at the 95% confidence level after a t-test. Note that after application of the downward-control principle there are no significant differences in the uppermost model layer, as here the streamfunction is zero by definition.

tion and the downward-control streamfunction with combined forcings from all types of wave drag can be used to roughly quantify the impact of the enhanced horizontal diffusion on the residual circulation.

Figure 4.8 also shows an offset in the 70 hPa streamfunction for the different vertical extents of the model. In the L31 model version the streamfunction is roughly 25% weaker than in the L95 model configuration. This behaviour is reflected by the total upward mass flux (see Tab. 4.1 and Fig. 4.9), which is also consistent with the differences in mean age of air above the tropical tropopause (see Fig. 4.4c). In the mid-latitudes, the additional force originating from enhanced horizontal diffusion has accelerated the air parcels in the L31 model, so that the age of air obtained from the L31 model in the mid-latitudes lies between the values associated with the two high-top models (see Fig. 4.3).

The directly calculated streamfunction, simulated with different vertical extents of the model, shows a conspicuous difference in the tropics. While in the high-top model a

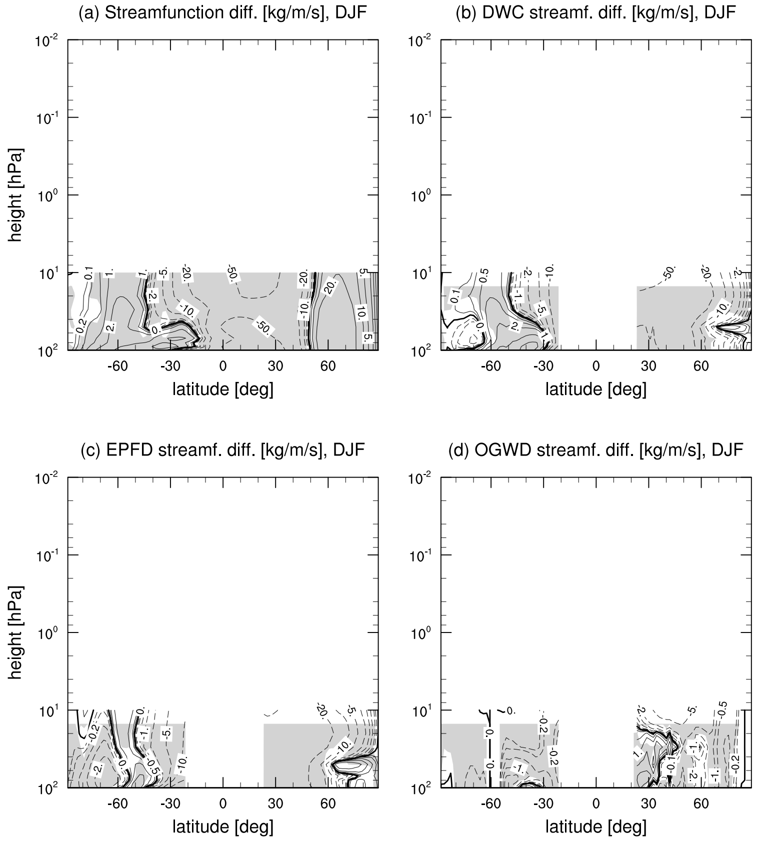

Figure 4.7: Streamfunction difference for the present-day time slice between different vertical extents of the model (L31-L95) is shown. The directly calculated streamfunction, the downward-control streamfunction with combined forcings from all types of wave drag (DWC), as well as the contribution of different wave drags separated via downward control (EPFD, OGWD) are presented. Shaded areas indicate significance at the 95% confidence level after a t-test.

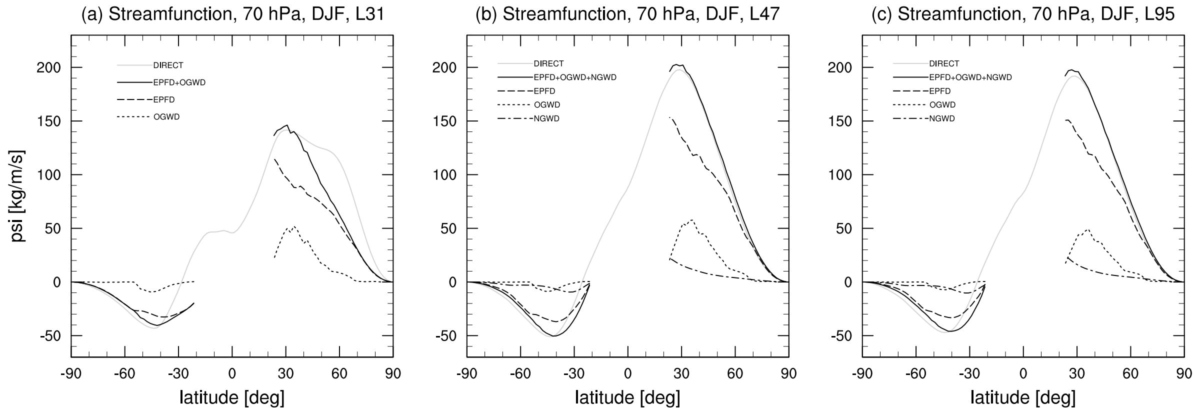

Figure 4.8: The DJF streamfunction at 70 hPa with contributions of different types of wave drag, as derived from the present-day time slice in the L31 (a), L47 (b), and L95 (c) model configurations, is presented.

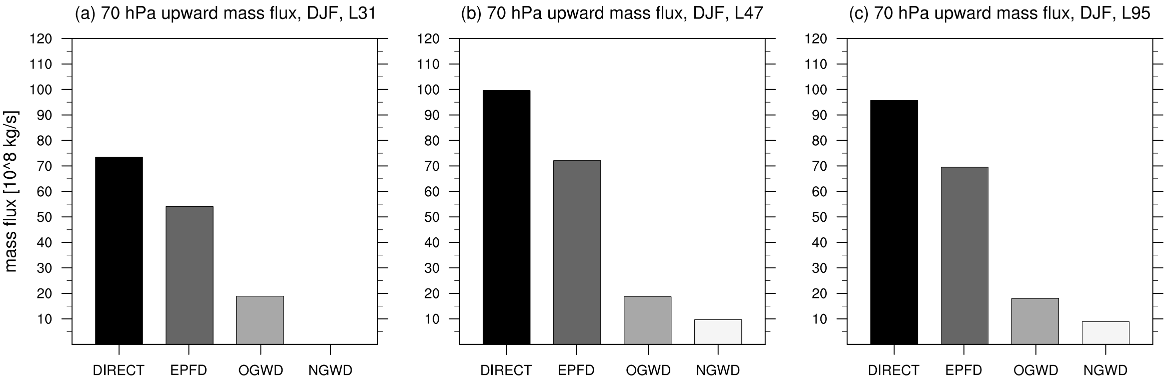

Figure 4.9: The DJF upward mass flux through the 70 hPa pressure surface together with contributions of different types of wave drag, as derived from the present-day time slice in the L31 (a), L47 (b), and L95 (c) model configurations, are presented.

relatively uniform tropical upwelling is simulated between the turnaround latitudes, the streamfunction is independent of the latitude in a confined latitude band close to the equator in the low-top model (see Fig. 4.8a), indicating a region of no tropical upwelling. It is not clear which mechanism causes this behaviour. Both the NGWD, which is important for the forcing of the easterly phase of the QBO in the L95 model (Giorgetta et al., 2006) and absent in the L31 model, as well as the modified horizontal diffusion scheme (see Section 2.1) in the low-top model might play an important role here.

Both high-top model configurations show comparable streamfunctions and upward mass fluxes (see Fig. 4.8b,c and 4.9b,c). The relatively small difference of less than 5% in the total upward mass flux at 70 hPa (see Tab. 4.1 and Fig. 4.9b,c) is caused by both resolved and unresolved wave drags with comparable relative contributions. The total upward mass flux in the L47 and L95 models is comparable in magnitude to the mass flux derived by Okamoto et al. (2011) and McLandress and Shepherd (2009) for similar periods in their CCMs. As in McLandress and Shepherd (2009) and the multi-model average of Butchart et al. (2011), the resolved wave drag yields the main contribution to the total upward mass flux at 70 hPa. Also the relative contributions of resolved and unresolved wave drag to the total upward mass flux are similar to the results of their CCM simulations. However, the contribution of resolved wave drag is higher in ECHAM6 than in the CCM used by Okamoto et al. (2011), which is compensated by a larger OGWD contribution in their model. As the horizontal resolution used by Okamoto et al. (2011) is lower than in our simulations and, thus, less waves are resolved in their model, the difference in contribution of different types of wave drag to the total upward mass flux could also be related to the different model setup.

A comparison of the mass fluxes obtained from the present-day time-slice simulation in the different model configurations (see Fig. 4.9) to ERA-Interim data, as evaluated by Seviour et al. (2012) and Okamoto et al. (2011), implies that the upward mass flux is overestimated in the high-top model by roughly 20%, which is due to an overestimation of the EPFD contribution. On the other hand, the OGWD contribution to the upward mass flux is much lower in all model configurations compared to ERA-Interim data (Okamoto et al., 2011). In the L31 configuration the total upward mass flux is com-

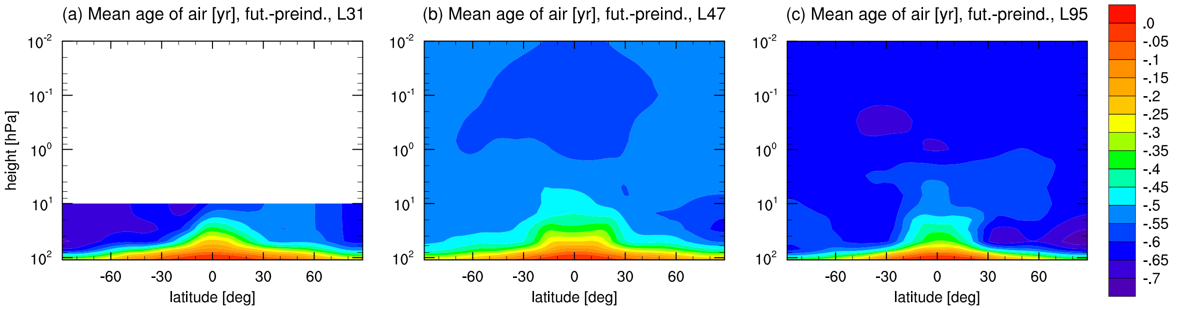

Figure 4.10: The annual-mean age of air difference between the preindustrial and the future climate state as simulated in the L31 (a), L47 (b), and L95 (c) model configurations is presented. In all model setups the differences are significant at the 95% confidence level in the entire model domain from 110 hPa upward.

parable to the values derived from ERA-Interim data. The reason for the difference between the models and ERA-Interim data in the relative contributions of resolved and unresolved wave drags to the upward mass flux, could be related to the coarser horizontal resolution of the ERA-Interim dataset used by Okamoto et al. (2011).

The model results evaluated in this section showed many similarities in the BDC simulated by the L47 and L95 models. However, in the low-top model the tropical upwelling at 70 hPa is roughly 25% slower and the enhanced horizontal diffusion leads to a distinct behaviour of the BDC in the upper model levels (starting at 90 hPa upwards) compared to the high-top models.

4.2 The simulated BDC change in different model configurations

The mean age of air decreases from the preindustrial to the future climate state in the entire model domain above the tropopause (see Fig. 4.10). This decrease is significant at the 95% confidence level in every model configuration, and indicates a strengthening of the BDC. The magnitude of the change in age of air depends on both height and latitude, but is generally smallest in the L47 configuration of the model. The distribution of the age change resembles in all configurations roughly the distributions obtained by Butchart et al. (2010) for several CCMs. The resemblance to their multi-model mean is highest in the L47 and L95 configurations, where the strongest age decrease occurs in the NH lower stratosphere. In the L95 model, the air is more than 270 days younger in the future than in the preindustrial state. Even though the L31 model does not resolve the entire stratosphere, a similar change in age of air as in the high-top configurations shows up. However, here the largest change is found in the SH. Generally, the change is larger in the L31 model compared to the L47 configuration, but smaller than in the L95 model version.

Streamfunction changes derived from the two high-top model configurations are very similar in the entire model domain (not shown). Except for slight differences in the tropics, which could be QBO-related, the change pattern is comparable between the two configurations.

The L31 model shows a change in the circulation pattern, which is similar in sign to the change in the L95 configuration (see Fig. 4.11). Both model versions show a strengthening of the BDC. Contributions of resolved and unresolved waves also have the same sign almost everywhere in the stratosphere, independent of the vertical extent of the model. Resolved waves consistently cause a BDC strengthening everywhere in the lower stratosphere as well as in the extratropical middle and upper stratosphere. In the subtropical middle and upper stratosphere, however, their impact leads to a more complex change in the circulation pattern. The change in unresolved wave drag, on the other hand, contributes to the BDC strengthening in the tropics and subtropics, but has a decelerating effect in the high latitudes of the winter hemisphere. The magnitude of the change in streamfunction and its attribution to different wave forcings, on the other hand, differ among the model configurations.

The BDC acceleration, as obtained from the change in pattern of the residual circulation, is in agreement with the study of Karpechko and Manzini (2012), who compared the response to doubled CO_2 concentrations in low-top and high-top versions of ECHAM5. However, Karpechko and Manzini (2012) found in both model configurations a BDC deceleration in the November-December mean streamfunction in the northern high-latitudes, which is absent in the DJF-mean streamfunction of our simulations. On the other hand, the pattern of the BDC acceleration (see Fig. 4.11) compares fairly well to the findings of McLandress and Shepherd (2009). Okamoto et al. (2011), however, found an additional cell of deceleration in the summer hemispheric subtropics of the middle stratosphere, which we do not observe in our simulations.

The change in streamfunction at the 70 hPa pressure surface as derived from the different model configurations (see Fig. 4.12) supports the findings obtained from the age of air (see Fig. 4.10). The L95 model simulates the strongest change in streamfunction. For the L31 model the streamfunction change is weak compared to the high-top model configurations, and an impact of the damping of resolved waves is again visible (see Fig. 4.12). Another conspicuous finding here is that in the mid-latitudes the EPFD contribution to the streamfunction change drops, while the OGWD contribution seems to compensate this drop. This compensation between EPFD and OGWD shows up in every model configuration, and is also visible in the CCM used by McLandress and Shepherd (2009).

As already indicated by the streamfunctions, the total upward mass flux change from the preindustrial to the future climate state at 70 hPa is the same in sign but different in magnitude for different model configurations (see Fig. 4.13). The EPFD contribution is more or less the same in both high-top model configurations, while slightly higher OGWD and NGWD contributions lead to a total mass flux change, which is roughly 15% larger in the L95 configuration. In the L31 model the total mass flux change at 70 hPa is roughly 30% lower than in the L95 model. However, taking into account that the total upward mass flux is generally also about 25% lower in the L31 model than in the high-top model (see Fig. 4.9), this is not a very surprising result. The most prominent finding here is that the origin of the change is primarily the EPFD in the L31 model, while the OGWD contribution is predominant for the upward mass flux change

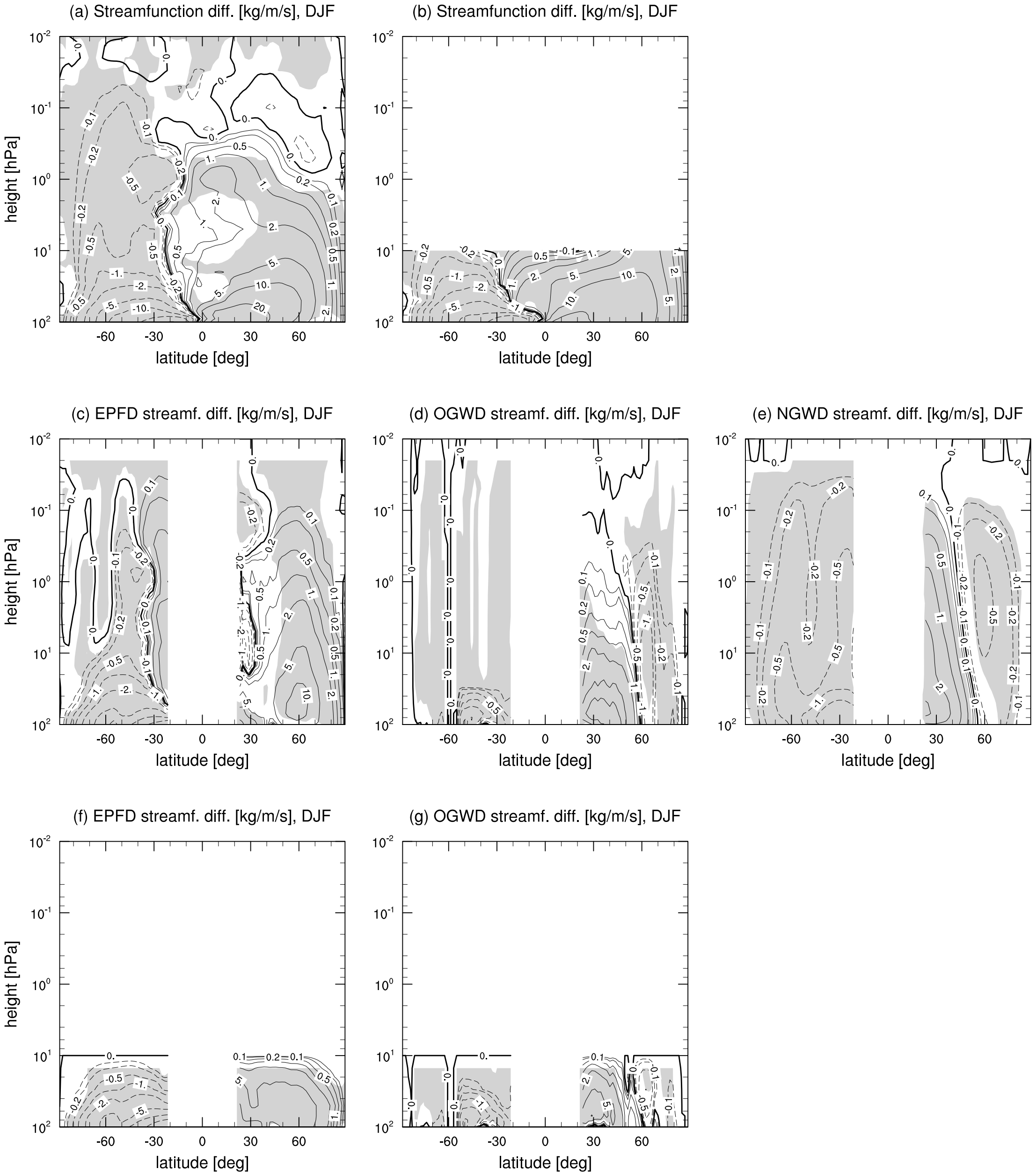
(a) Streamfunction diff. [kg/m/s], DJF

(b) Streamfunction diff. [kg/m/s], DJF

(c) EPFD streamf. diff. [kg/m/s], DJF

(d) OGWD streamf. diff. [kg/m/s], DJF

(e) NGWD streamf. diff. [kg/m/s], DJF

(f) EPFD streamf. diff. [kg/m/s], DJF

(g) OGWD streamf. diff. [kg/m/s], DJF

Figure 4.11: The mass streamfunction difference between preindustrial and future climate states, as derived from the L95 model configuration and for the L31 model version is shown. The directly calculated mass streamfunction (a,b), as well as the contribution of different wave drags separated via downward control (c-g) are presented. Shaded areas indicate significance at the 95% confidence level after a t-test.

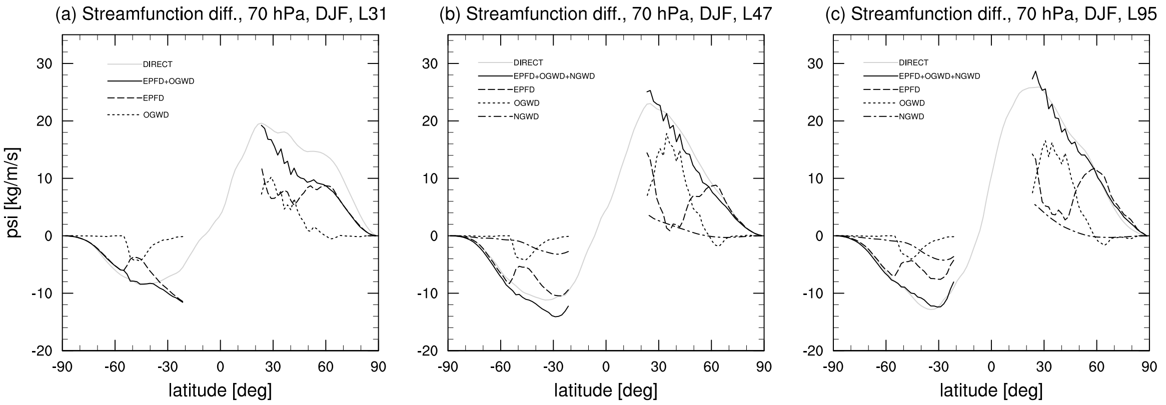

Figure 4.12: The streamfunction difference between preindustrial and future climate states together with contributions of different types of wave drag, as derived from the L31 (a), L47 (b), and L95 (c) model configurations, is presented.

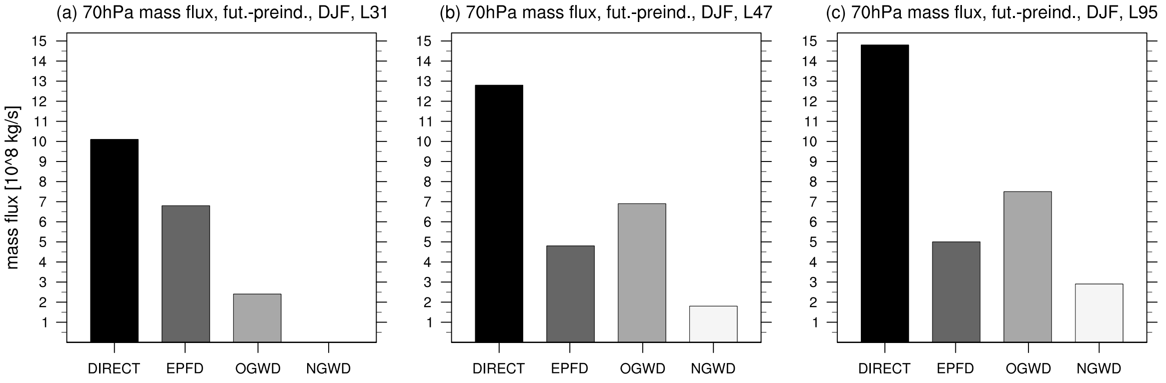

Figure 4.13: The 70 hPa DJF upward mass flux difference between preindustrial and future climate states together with contributions of different types of wave drag, as derived from the L31 (a), L47 (b), and L95 (c) model configurations, are presented.

at 70 hPa in both high-top model configurations. According to Equation 3.34 the sum of the absolute values of the streamfunction at the turnaround latitudes, located at roughly 30°N and 43°S (see Fig. 4.8), gives the total upward mass flux. While the difference in streamfunction changes at 43°S is small among the model configurations (see Fig. 4.12), the behaviour of the streamfunction at the northern turnaround latitude (30°N) is crucial for the different origin of the streamfunction change in low-top and high-top model versions. At 30°N, the OGWD yields the main contribution to the streamfunction change in the high-top models, causing the mass flux in the L47 and L95 models to be OGWD-dominated (see Fig. 4.13). On the other hand, in the low-top model OGWD and EPFD contributions to the streamfunction change at 30°N are comparable. Thus, the EPFD-dominated streamfunction change in the SH causes the mass flux to be EPFD-dominated in the L31 model.

In McLandress and Shepherd (2009) as well as in Garcia and Randel (2008) the EPFD contribution to the increase in the DJF-mean upward mass flux through the 70 hPa pressure surface was found to be roughly 70%. In both of these studies high-top CCMs were used, which contributed to the CCMVal activity of SPARC. Their result is in

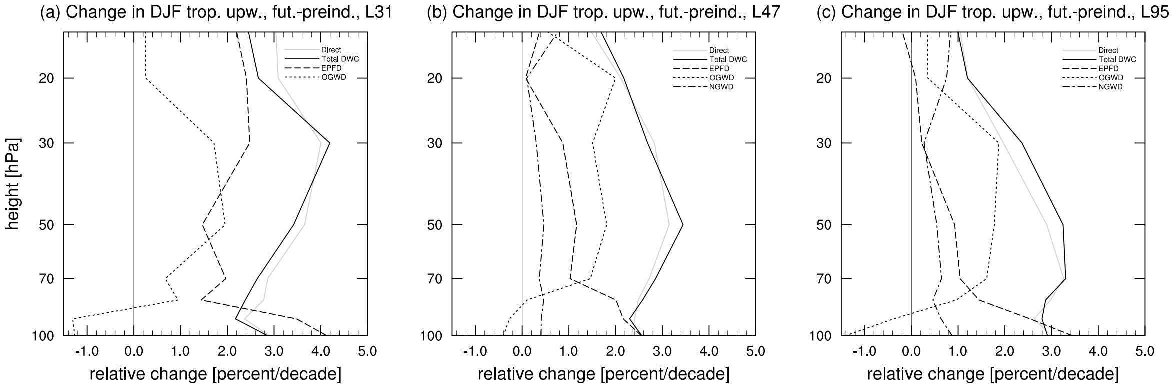

Figure 4.14: Relative change in DJF tropical upwelling from the preindustrial to the future climate state, together with contributions of different types of wave drag, as derived from the L31 (a), L47 (b), and L95 (c) model configurations, are presented.

good agreement with our L31 simulations (see Fig. 4.13), however, it contradicts the findings obtained from our high-top simulations. Garny et al. (2011) also found an EPFD-dominated 70 hPa upward mass flux increase in their low-top CCM. On the other hand, Butchart et al. (2010) found a large spread in the wave type contributions to the BDC trend simulated by the different CCMVal-1 models.

In order to see how this behaviour changes with height, the contribution of the different types of wave drag to the relative change in tropical upwelling is evaluated in the vertical profile (see Fig. 4.14). EPFD is identified as the main contributor to the change in tropical upwelling in the lowermost stratosphere (75-100 hPa) in every model configuration. From 100 hPa upward, the EPFD contribution decreases with height in all model versions. This decrease is compensated by an increase in the OGWD contribution. In the two high-top models the OGWD exceeds the EPFD contribution at roughly 75 hPa, and is the primary contributor to the upward mass flux increase up to 10 hPa. In the low-top model the OGWD exceeds the EPFD contribution only in a small altitude range at around 50 hPa. Above 50 hPa, here the EPFD is again the primary contributor to the increase in tropical upwelling.

The increase in parameterised wave drag in the middle stratosphere (10-70 hPa) as well as the increase in resolved wave drag in the lower stratosphere (70-100 hPa) are consistent with an upward shift of the breaking level of orographic gravity waves and the critical layers for resolved wave dissipation, caused by the modified zonal-mean zonal wind field (see Fig. 4.1).

While the model results discussed in Section 4.1 showed that the relative wave drag contributions to the driving of the BDC are similar among the model configurations, the evaluation of BDC changes indicated that simulations with different vertical model extents produce changes comparable in sign and magnitude, which originate from different causes.

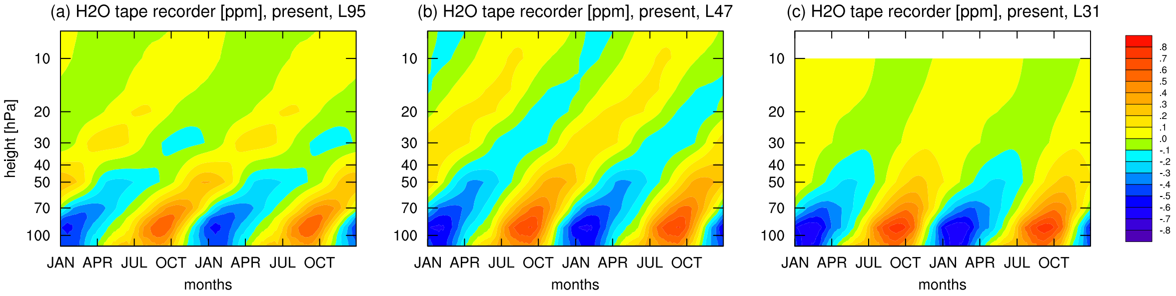

Figure 4.15: The water vapour tape recorder, i.e. the climatological mean anomalies in specific humidity for 12.5°S to 12.5°N, as derived from the 50-year present-day time-slice simulation performed with the ECHAM6 GCM in the L95 (a), L47 (b), and L31 (c) configurations, is shown.

4.3 The BDC inferred from the water vapour tape recorder

Another approach to derive the tropical upwelling velocity and, thus, obtain a measure of the BDC strength is to evaluate the speed of the upward propagating anomalies in H_2O concentrations, i.e. the water vapour tape recorder (see Section 3.3). Comparing the derived water vapour ascent rates among different model configurations provides an estimate of the ability of a given model configuration to simulate the transport of a tracer species realistically.

Figure 4.15 shows the water vapour tape recorder, as it is simulated in different ECHAM6 model configurations. It is readily apparent that the ascent rate of water vapour anomalies increases with decreasing vertical resolution in the stratosphere. In Figure 4.16 the H_2O ascent rates, derived as described in Section 3.3, are shown and compared to the tropical upwelling velocities derived from dynamics in the TEM framework (see Section 3.1). In the CCMVal report (Neu et al., 2010) these quantities were derived for many different CCMs, and the results were compared to observational data obtained from different proxies. For almost all CCMs a positive offset of ascent rates derived from H_2O anomalies, was found, compared to the TEM tropical upwelling velocity derived from model simulations. Neu et al. (2010) attributed this discrepancy to vertical diffusion, horizontal and vertical eddy fluxes, and other effects originating from the difference between transport and the residual circulation (Andrews et al., 1987). The TEM vertical velocities, on the other hand, lie within the uncertainties of the observational proxies for almost all the models. Also in all model configurations of ECHAM6 (see Fig. 4.16) the TEM tropical upwelling is comparable to the observations. A comparison between tropical upwelling velocities derived from ascending H_2O anomalies and those obtained via the TEM framework, shows that the positive offset of H_2O ascent rates also exists in ECHAM6. Here the discrepancy clearly increases with decreasing vertical resolution in the stratosphere. Thus, we attribute this discrepancy primarily to increased vertical diffusion due to lower vertical model resolution. Only in the L95 model configuration, the water vapour ascent rates lie within the uncertainties

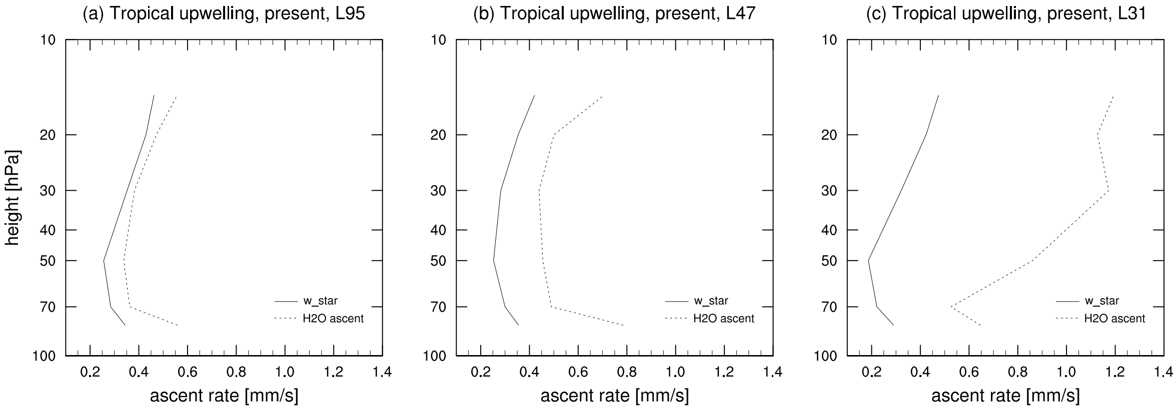

Figure 4.16: Vertical profiles of the vertical transport velocities derived from the water vapour tape recorder (see Section 3.3) are shown and compared to the tropical upwelling velocities calculated via the TEM framework (see Section 3.1). The data was obtained from 50-year present-day time-slice simulations performed with the ECHAM6 GCM in the L95 (a), L47 (b), and L31 (c) model configurations.

of the observations, implying that only in this configuration the transport of tracer species can be considered to be realistically simulated.

In Figure 4.17 the change in tropical ascent rates from the preindustrial to the future climate state is depicted, as derived from time-slice simulations with the ECHAM6 L95 model configuration. Both methods, the vertical transport velocity derived via the TEM framework as well as the H_2O ascent rate, reflect a strengthening of the tropical upwelling at 70 hPa, and also a positive trend at the levels above but with smaller amplitude. The behaviour of the change in the H_2O ascent rate below 70 hPa suggests that an upward shift of the tropopause induced by increasing GHG concentrations causes the derivation method of H_2O ascent rates not to be applicable here anymore in a future climate. The increase in tropopause height, which was found in both observations and model simulations (e.g. Kushner et al., 2001; Santer et al., 2003), invalidates the assumption of limited horizontal mixing in the region of the former lowermost stratosphere and, thus, severely affects the H_2O ascent rates derived from the water vapour tape recorder in the future climate state at these altitudes.

By evaluating the tropical ascent rates inferred from the water vapour tape recorder the BDC strength and its trend derived from other BDC measures (see Sections 4.1 and 4.2) was validated. Additionally, the analysis provided the opportunity for a comprehensive estimation of artificial vertical diffusion effects in the different model configurations, which also yield implications for the estimation of the mean age of air from model simulations derived from tracers. It turned out that only in the L95 model configuration the upward transport of water vapour is realistically simulated. This may explain also the differences in mean age of air derived from passive tracers in the different model configurations (see Fig. 4.4).

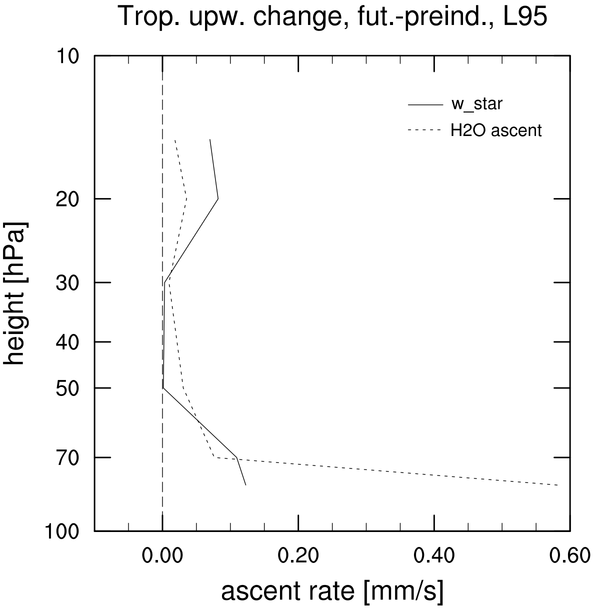

Figure 4.17: The vertical profile of the change in vertical transport velocities from the preindustrial to the future climate state, as derived from the water vapour tape recorder (see Section 3.3), are shown and compared to the associated change in tropical upwelling velocities calculated via the TEM framework (see Section 3.1). The data was obtained from 50-year time-slice simulations performed with the ECHAM6 GCM in the L95 (a), L47 (b), and L31 (c) model configurations.

Chapter 5

BDC trend versus natural BDC variability

The discrepancy between model and observational data in terms of the response of the BDC to a changing climate (Engel et al., 2009) shall be evaluated in this section by comparing BDC trends with the natural BDC variability. Butchart et al. (2000) found decadal variability in the high latitudes of the northern hemisphere stratosphere to overshadow trends derived from their 60-year model integrations. They attributed this decadal variability to internal atmospheric variability, connected also with a change in the frequency of sudden stratospheric warmings (SSWs), which will be investigated later in this thesis (see Section 6). Besides the internal atmospheric variability, there are also other factors which were found to cause longterm stratospheric variability. Kodera and Kuroda (2002) found the 11-year solar cycle to impact the BDC. García-Herrera et al. (2006) found a connection between warm ENSO events and the BDC, which may induce modes of low-frequency BDC variability. Marsh and Garcia (2007) corroborated this result by finding stratospheric circulation changes to lag changes in the NINO3.4 index, representing SST anomalies in the central Pacific, by a few months.

In the following it is investigated to what extent the BDC trend, derived from observational datasets or model simulations, can be considered to be significantly distinguishable from the natural variability of the BDC. As the longest age-of-air time series, which provides the best available observational proxy for the BDC strength, covers only a time period of roughly 30 years, it has been impossible so far to assess decadal and multi-decadal modes of natural BDC variability from observations. Thus, in this study the BDC natural variability is derived from the multi-centennial CMIP5 preindustrial control simulations performed with MPI-ESM in the LR and MR configuration (see Section 2.2 for model description), and provide a critical investigation of the significance of BDC trends derived from model and observational datasets. First it is evaluated to what extent the accessible measures of the BDC strength are capable to reflect BDC variability and trends (see Section 5.1). The significance of BDC trends is then analysed by contrasting the derived trends in BDC strength to the obtained natural BDC variability (see Section 5.2). Eventually, a potential tropospheric origin

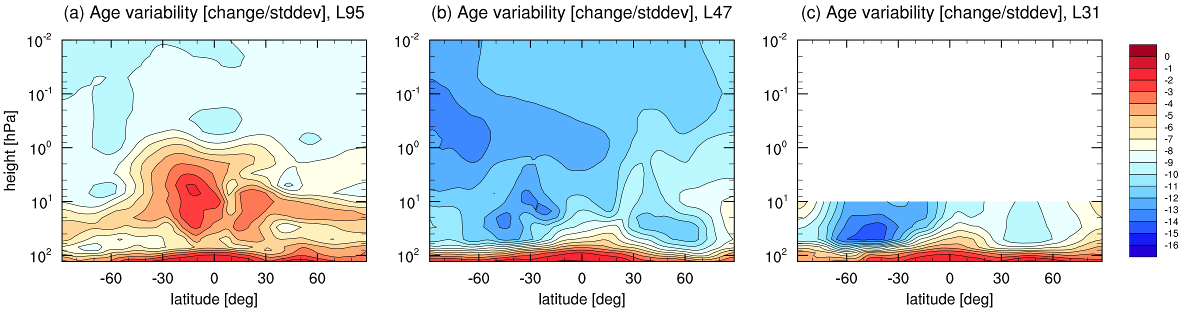

Figure 5.1: The variability of the age of air, i.e. the difference "future minus preindustrial" divided by the standard deviation of the age of air derived from the preindustrial simulation, is shown. The data was obtained from the 50-year time-slice simulations performed with the ECHAM6 GCM in the L95 (a), L47 (b), and L31 (c) configurations.

of the decadal-scale natural BDC variability is identified by investigating the connection between variability modes in the central Pacific SSTs and the BDC strength (see Section 5.3).

5.1 Measures of the BDC natural variability

In state-of-the-art climate models, the most common measure of the BDC strength is the 70 hPa tropical upwelling velocity as well as the age of stratospheric air. As tropical upwelling velocities usually lie in the order of millimeters per second in the global average, accurate measurements of the vertical transport velocity in the lower stratosphere turn out to be hardly feasible. The extratropical age of stratospheric air is commonly considered as the best observational proxy for the strength of the BDC, and commonly used to validate the realistic simulation of the BDC strength in state-of-the-art climate models. The longest available observational time series of the age of air (Engel et al., 2009) was derived from measurements of tracer concentrations at 30 hPa (24 km) between 30°N and 50°N. In the following we shall investigate to what extent a BDC trend obtained in this region can be distinguished from natural variability in the age of air and, thus, the BDC. The correlation between the extratropical age of air and the tropical upwelling at 70 hPa is first evaluated, in order to investigate if a signal in the age of air is also reflected in the 70 hPa tropical upward mass flux. As no age-of-air tracer was incorporated in the MPI-ESM model for the CMIP5 simulations, it is hereby shown that changes in the 70 hPa upward mass flux affect the BDC strength in the entire middle atmosphere in the ECHAM6 GCM, the atmospheric component of MPI-ESM.

In Figure 5.1 the change in age of air from the preindustrial to the future climate state divided by the standard deviation of the age in the preindustrial simulation is shown for the different model configurations of ECHAM6. As already seen in Figure 4.10 the age of air decreases in all model configurations at all levels above the tropopause, implying an increase in the BDC from the preindustrial to the future climate state. In the L95 configuration, the decreasing trend in the age of air is overshadowed by strong age variability (see Fig. 5.1) due to the secondary meridional circulation induced by

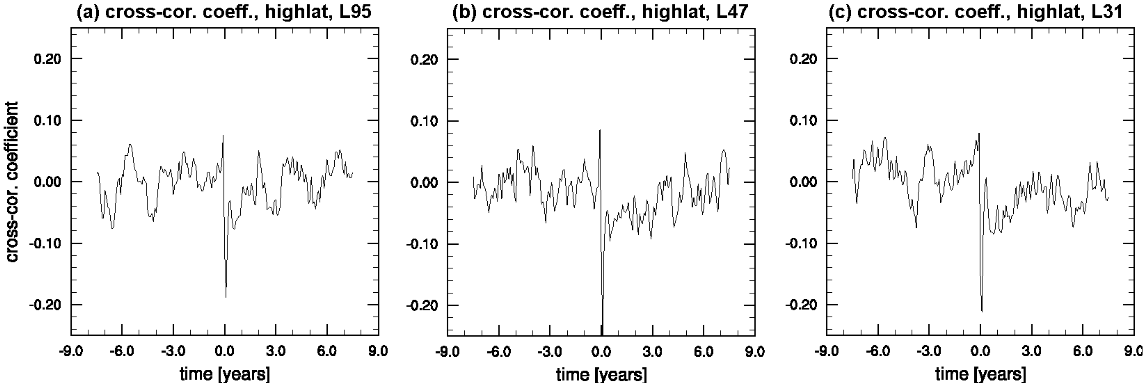

Figure 5.2: Cross-correlation coefficients between the 70 hPa total upward mass flux and the age of air at 30°-50°N and 30 hPa are shown. Positive time shifts indicate that the signal in the tropical upwelling leads the signal in the age of air. A negative cross-correlation coefficient implies that an increase in 70 hPa total upward mass is connected to decrease in age of air, or vice versa. The data was derived from the present-day time-slice simulation performed with ECHAM6 in the L95 (left), L47 (middle), and L31 (right) model configurations.

the internally generated QBO. In the L47 and L31 model configurations the age trend is more easily distinguishable from age variability, which we primarily associate with the missing QBO in these configurations. Generally, the age variability is lower on the southern hemisphere, which is likely to be related to the lower large-scale wave activity propagating upward from the troposphere to the stratosphere due to the lower land-sea contrast on the southern hemisphere. Moreover, in all ECHAM6 model configurations the obtained age variability implies that the extratropical lower stratosphere (30 hPa, 30°N to 50°N) is well suited to derive an age trend and, thus, a trend in the BDC, as this region is affected relatively little by internal BDC variability.

In order to investigate to what extent a signal in the age of air is related to a signal in the 70 hPa tropical upwelling in the ECHAM6 GCM, we evaluate the cross correlation of the 70 hPa upward mass flux and the age of air in the extratropical lower stratosphere (see Fig. 5.2) and in the equatorial upper stratosphere (see Fig. 5.3). In all model configurations a negative correlation exists between the tropical upwelling and the extratropical age of air at small time lags led by the tropical upwelling. This implies that a positive anomaly in the tropical upward mass flux is likely to be followed by a negative anomaly in the extratropical age of air. In the L47 and L31 model configurations the cross-correlation coefficient still reflects a connection between the two BDC measures for time lags of up to 7 years, with the signal again led by the tropical upwelling. This effect is likely to be due to the different trajectories of the BDC, as anomalies in the tropical upward mass flux may reach the extratropics via different circulation pathways. In the L95 model configuration this effect is not that large. Here, however, two confined intervals of enhanced amplitudes in the cross-correlation coefficient show up, separated by a time interval comparable to the period of the QBO. This might reflect that the QBO introduces a systematic time shift in BDC anomalies between the tropics and extratropics by inducing the secondary meridional circulation.

In the L47 model configuration the age of air in the equatorial upper stratosphere (see Fig. 5.2) also shows a negative correlation with the tropical upwelling. The time

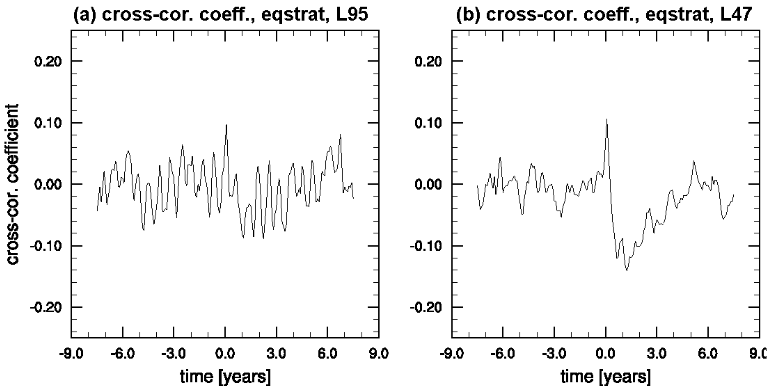

Figure 5.3: Cross-correlation coefficients between the 70 hPa total upward mass flux and the age of air at 20°S-20°N and 1 hPa are shown. Positive time shifts indicate that the signal in the tropical upwelling leads the signal in the age of air. A negative cross-correlation coefficient implies that an increase in 70 hPa total upward mass is connected to decrease in age of air, or vice versa. The data was derived from the present-day time-slice simulation performed with ECHAM6 in the L95 (left) and L47 (right) model configurations.

lag reaches up to 5 years with the signal led by the tropical upwelling. In the L95 configuration, however, the correlation between the two measures of BDC strength is substantially lower compared to the L47 configuration. The modulation of the tropical upwelling by the internally generated QBO is likely to diminish here the correlation between the upward mass flux and the age of upper stratospheric air.

We have seen that, in ECHAM6, anomalies in the extratropical age of air, which yields the best observational proxy for the BDC strength, are adequately reflected by anomalies in the 70 hPa tropical upward mass flux, especially in model configurations without an internally generated QBO.

5.2 Significance and origin of BDC trends

In Section 4.2 we have obtained from simulations with ECHAM6 in different model configurations that the BDC strength increases from the preindustrial to the future climate state. The primary origin of the positive BDC trend simulated by ECHAM6 was found to depend on the applied model configuration. In the L31 (low-top) configuration, the BDC increase was found to be primarily caused by resolved wave drag, whereas in the L47 and L95 (both high-top) configurations the BDC strengthening is primarily caused by parameterised wave drag. While these results turned out to be robust in multi-decadal model simulations under stationary boundary conditions, significant BDC trends are much more difficult to obtain from the slowly varying climate state of the real world. In order to investigate the significance and origin of BDC trends simulated for the second half of the 20th century, the BDC trend obtained from the transient CMIP5 simulations with the Earth System Model MPI-ESM (see Section 2.4.2) is in the following compared to the natural BDC variability in the associated preindustrial control run.

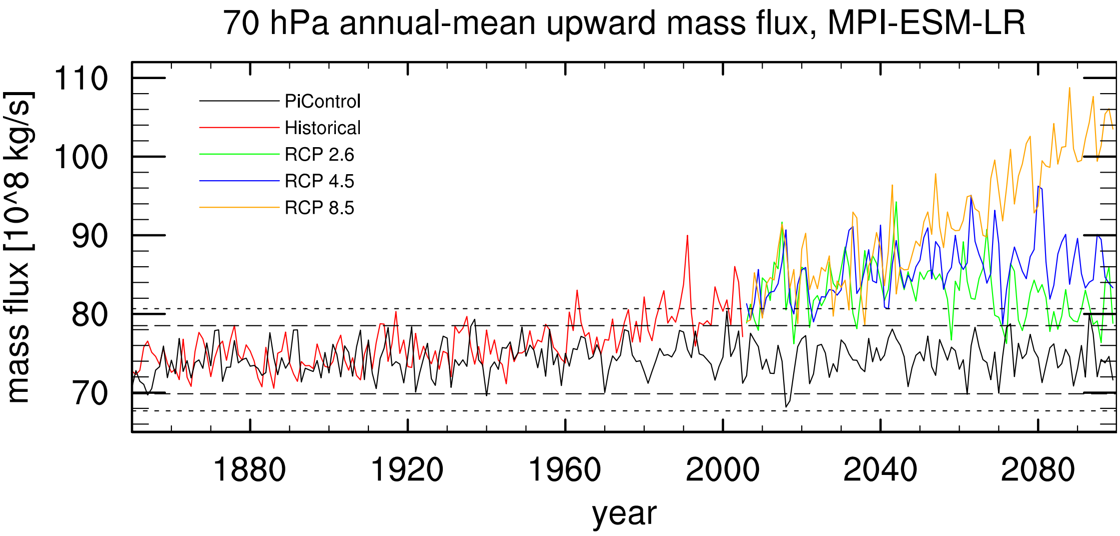

Figure 5.4: The annual-mean 70 hPa total upward mass flux, as derived from the CMIP5 simulations (see Section 2.4.2) performed with MPI-ESM (see Section 2.2) in the LR model configuration, is shown. For all transient simulations, results of only one ensemble member is presented. The dashed lines indicate the 2-sigma interval of the preindustrial control simulation, as computed from the entire 1000-year period. The dotted lines show the 3-sigma interval, respectively.

The 70 hPa annual-mean upward mass flux simulated by MPI-ESM is shown in Figure 5.4. Since no age-of-air tracer was incorporated in MPI-ESM, and since we have seen in Section 5.1 that the 70 hPa upward mass flux is an appropriate measure for the BDC strength in ECHAM6 also in the extratropical stratosphere, the following analysis is restricted to the upward mass flux at 70 hPa. In Figure 5.4 it is readily apparent that in the LR configuration of MPI-ESM the 70 hPa upward mass flux exceeds the 3-sigma threshold of the 1000-year preindustrial control simulation for the first time in the second half of the 21st century. Depending on the GHG emission scenario the future increase in BDC strength is more or less strong. While the BDC strengthening is largest in the RCP8.5 scenario, which assumes the highest increase in GHG concentrations, in the lowest GHG-emission scenario RCP2.6 the BDC increase is much weaker and the BDC strength is even not significantly distinguishable anymore from the preindustrial BDC strength at the end of the 21st century.

The 70 hPa upward mass flux is usually strongest in the DJF season, and also the contribution of the change in BDC strength to the annual-mean BDC strength is largest in DJF (see Section 4.2). In Figure 5.5 the upward mass flux as well as the contribution of resolved (EPFD) and unresolved (GWD) wave drag is shown for the CMIP5 simulations including the extended RCP future scenarios (see Section 2.4.2). As the gravity wave drag was not included in the output of the CMIP5 simulations, the unresolved wave drag contribution to the BDC strength was calculated here as the difference between the total upward mass flux and the resolved wave drag contribution, which usually yields a good approximation to the sum of orographic and non-orographic gravity wave drag contributions (see Section 4.1). It turns out that the increase in BDC strength is by far largest in the RCP8.5 scenario (see Fig. 5.5). The increase is here almost exclusively

(a) 70 hPa DJF-mean upward mass flux, MPI-ESM-LR

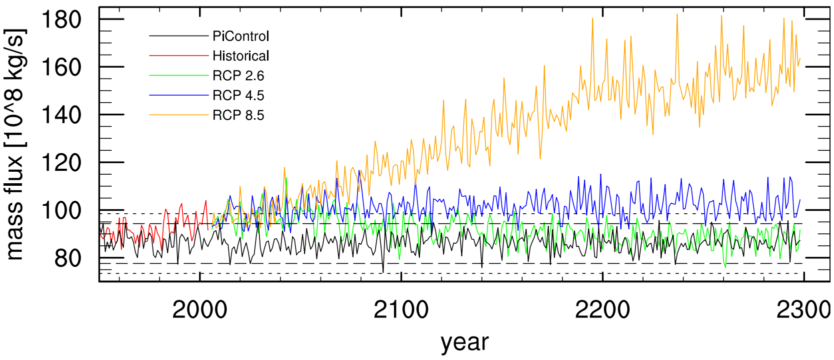

(b) 70 hPa DJF-mean upward mass flux due to EPFD

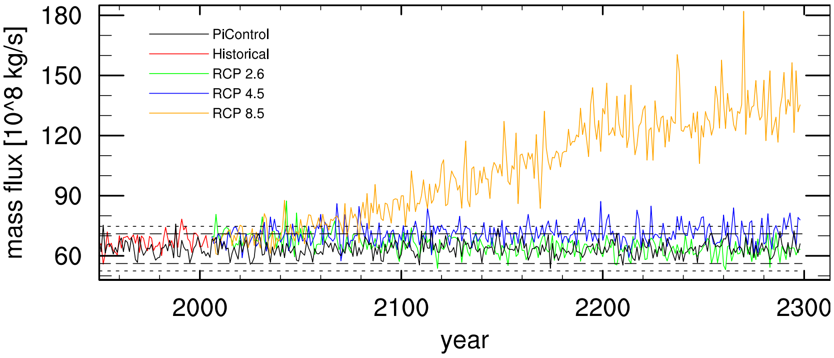

(c) 70 hPa DJF-mean upward mass flux due to GWD

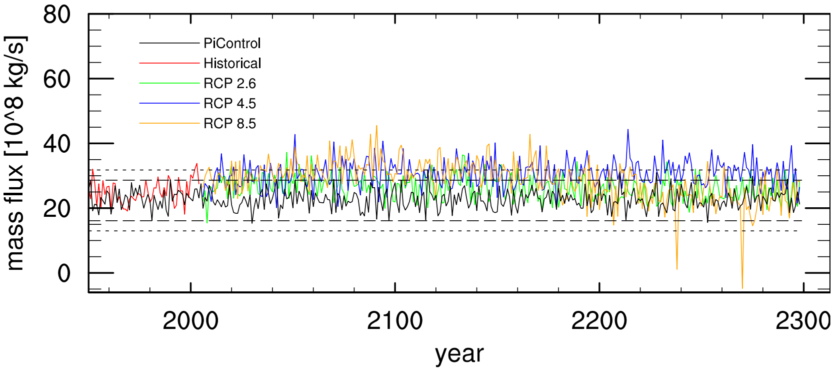

Figure 5.5: The DJF-mean 70 hPa total upward mass flux, as derived from the CMIP5 simulations performed with MPI-ESM in the LR model configuration, is shown. For all transient simulations, results of only one ensemble member is presented. The dashed lines indicate the 2-sigma interval of the preindustrial control simulation, as computed from the entire 1000-year period. The dotted lines show the 3-sigma interval, respectively. The different plots indicate the total DJF-mean 70 hPa upward mass flux (a), the contribution of resolved wave drag (b), and the contribution of gravity wave drag (c) as estimated from the difference of the total mass flux and the resolved wave contribution.

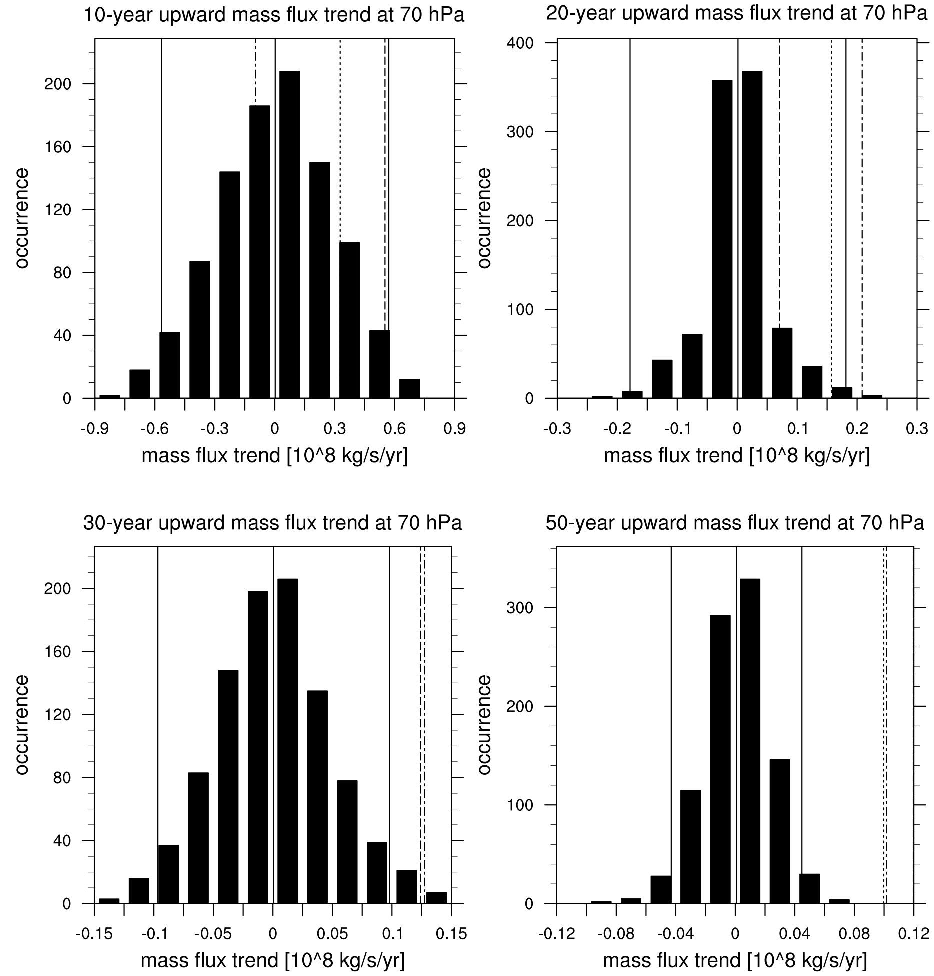

Figure 5.6: Trends in the annual-mean total upward mass flux, as derived from the preindustrial control simulation (histograms) and the three ensemble members of the historical simulation (dashed, dotted, and dashed-dotted lines) performed with MPI-ESM in the LR model configuration, are shown. The trends were computed via linear regression for the last 10, 20, 30, and 50 years (see plot title) of the historical simulation and for all time intervals of the respective period in the preindustrial control simulation. The 2-sigma interval of the trends obtained from the preindustrial control simulation is indicated by the solid lines.

due to an increase in the EPFD contribution, while for the moderate BDC increase in the other future scenarios the GWD contribution is at least as important as the EPFD contribution. The large EPFD contribution to the BDC strengthening obtained for the RCP8.5 scenario differs from the simulated primary origin of the BDC increase in the stand-alone ECHAM6 GCM (see Section 4.2). In the ECHAM6 high-top model (L47 and L95), the parameterised wave drag yields the primary contribution to the BDC increase. However, for the future climate state simulated with ECHAM6 stationary boundary conditions reflecting the climate state of 2050 were used (see Section 2.4.1). This implies that under the extreme climate change conditions, simulated in the RCP8.5 scenario from the end of the 21st century onwards, the dissipation and breaking of resolved waves yields the primary contribution to the BDC strengthening.

Besides the strong BDC increase, in the RCP8.5 scenario some decadal-scale oscillation

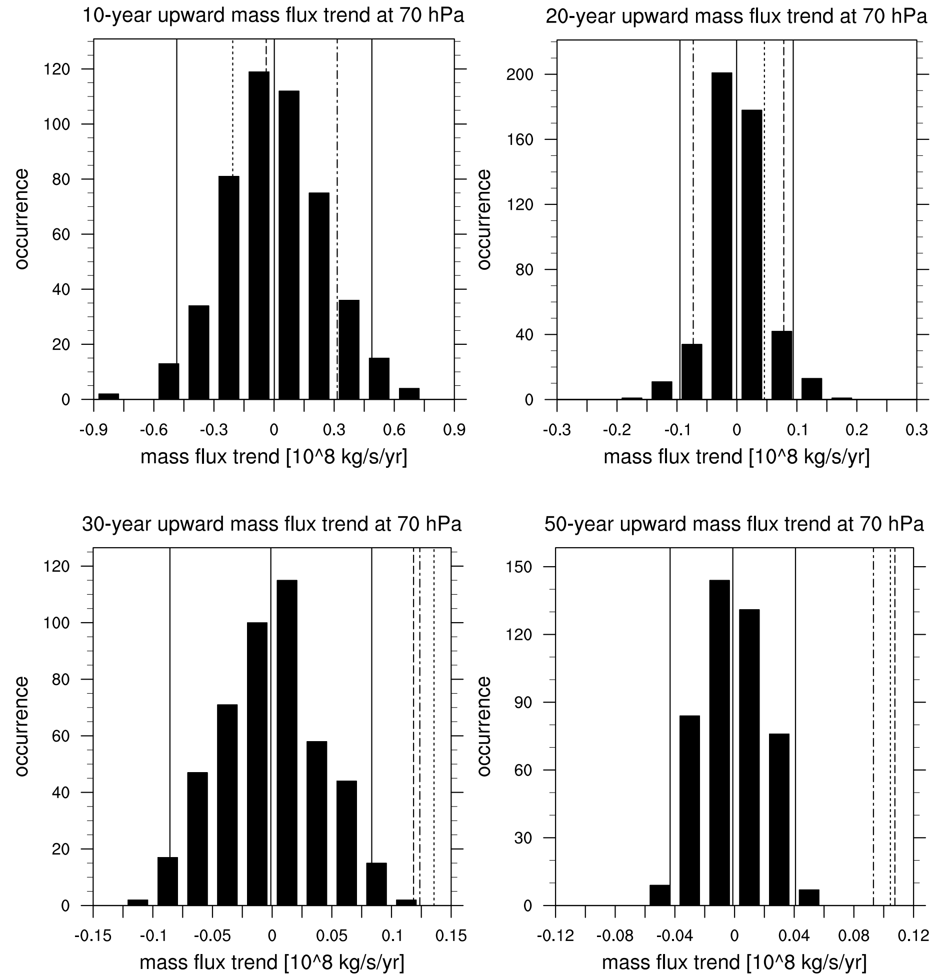

Figure 5.7: Trends in the annual-mean total upward mass flux, as derived from the preindustrial control simulation (histograms) and the three ensemble members of the historical simulation (dashed, dotted, and dashed-dotted lines) performed with MPI-ESM in the MR model configuration, are shown. The trends were computed via linear regression for the last 10, 20, 30, and 50 years (see plot title) of the historical simulation and for all time intervals of the respective period in the preindustrial control simulation. The 2-sigma interval of the trends obtained from the preindustrial control simulation is indicated by the solid lines.

in BDC strength seems to occur in the remote future after 2100, and in two single years the GWD even yields an extremely low (in one year even negative) contribution to the upward mass flux. All these features reflect an extreme climate change, which shall be further evaluated in Section 6.1.3.

In order to investigate the expected significance of BDC trends derived from observational datasets or transient model simulations covering the last decades of the 20th century, we contrast the BDC change in the last decades of the historical run to the natural variability on the respective timescale in the preindustrial run. The histograms in Figure 5.6 reflect all 10-year (20-year, 30-year, and 50-year, respectively) trends derived from the preindustrial control simulation, performed with MPI-ESM in the LR configuration, via linear regression. The BDC trend obtained from the last 10 (20, 30, and 50, respectively) years of the three ensemble members of the historical simulation (1995-2005, 1985-2005, etc.) is contrasted with the 2-sigma threshold of the histograms. It is readily apparent that the linear BDC trend of the last 10 or 20 years of the historical run can not be considered to be significantly distinguishable from natural BDC variability. Only by deriving the linear BDC trend over at least the last 30 years of the historical run, all ensemble members show a BDC increase, which can be considered to be significantly different from the average associated BDC trend in the preindustrial run. Another prominent feature is the relatively sharp peak of the histogram covering linear 20-year trends of the BDC strength. As we shall see later, this behaviour reflects that a time period of 20 years provides a good match to the large-amplitude modes of long-term BDC variability.

Figure 5.7 shows the results of the same analysis for the MR configuration of MPI-ESM. The internally generated QBO in this model configuration seems to reduce the occurrence of extreme BDC trends in both the historical simulation as well as the preindustrial control run by modulating the tropical upwelling. All histograms are more confined around zero compared to the LR configuration. As in the LR configuration, the results indicate that a time span of at least 30 years is necessary to obtain a trend in BDC strength significantly distinguishable from natural BDC variability, and a time span of 20 years seems to match best the large-amplitude modes of long-term BDC variability.

Although we found the upward mass flux through 70 hPa to clearly exceed the 3-sigma level of the 1000-year preindustrial run in the second half of the 21st century (see Fig. 5.4), the model simulations suggest that it remains difficult to derive significant trends in BDC strength from observational datasets. While the investigated model datasets yield a much better spatial and temporal resolution than any observational time series, it turns out that even in the model a 30-year period of well-resolved data is necessary to identify a BDC trend significantly distinguishable from natural BDC variability.

5.3 Origin of the BDC natural variability

As the natural BDC variability turned out to be important, when deriving trends in BDC strength (see Section 5.2), we shall evaluate the origin of the natural BDC variability in the following. The communication of anomalies from the troposphere-surface system to the stratosphere, especially from signals in the tropical sea surface temperatures (SSTs), has been investigated e.g. by Garny et al. (2009). García-Herrera et al. (2006) already found enhanced vertical propagation of Rossby waves during warm ENSO events to force an acceleration of the BDC winter branch. Changes in the BDC generally lag changes in, e.g. the *NINO 3.4 index* (central Pacific SST anomalies at 5°N to 5°S and 120°W to 170°W), by a few months (Marsh and Garcia, 2007).

In order to investigate the covariability of tropical SSTs and the BDC strength, the cospectrum of the NINO 3.4 index and the 70 hPa upward mass flux is evaluated in the following. The cospectrum represents the real part of the cross-spectrum of two quantities and, thus, can be used as a measure for the covariability of these quantities. In Figure 5.8 the cospectrum of the NINO 3.4 index and the 70 hPa upward mass

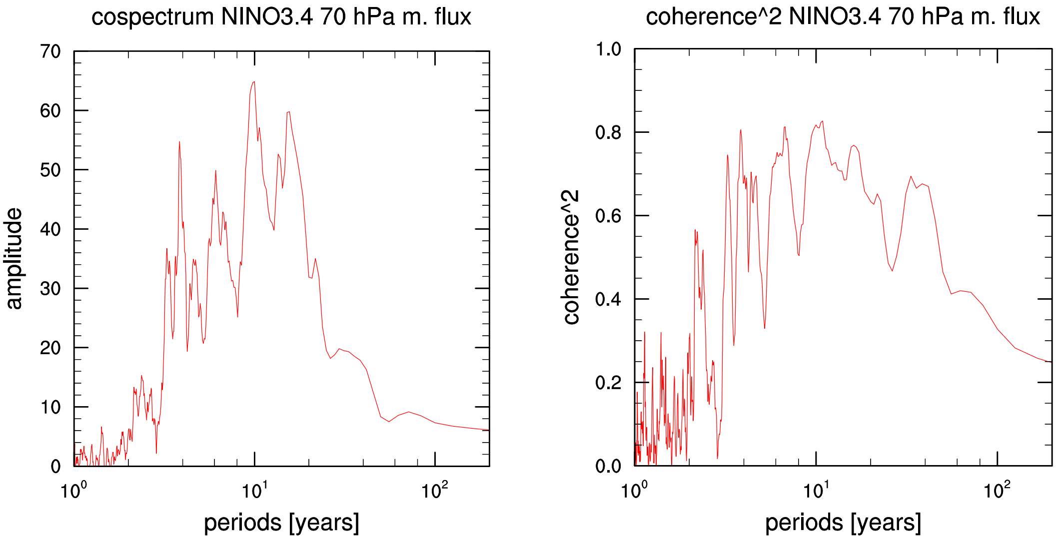

Figure 5.8: The cospectrum for the NINO3.4 index and the 70 hPa annual-mean total upward mass flux is shown (left) together with the associated squared coherence (right). The squared coherence is a measure for the significance of the covariability at a given frequency. The data was derived from the 500 years of the preindustrial control simulation performed with MPI-ESM in the LR model configuration.

flux is depicted together with the associated coherence, as derived from the 1000-year MPI-ESM preindustrial control run in the LR configuration. The coherence of the variability modes of two quantities yields a measure for the significance of the connection between these quantities at a given frequency. Substantial covariability between the NINO3.4 index and the BDC strength is found at periods between 3 and 20 years. An evaluation of the phase shift (not shown) between the variability modes in the two quantities indicates that, for almost the entire range of periods, the signal in the NINO 3.4 index leads the upward mass flux signal. The prominent 10-year mode of covariability (see Fig. 5.8) may be considered to be associated with the tropical Pacific quasi-decadal oscillation (TPQDO; White and Liu, 2008). This oscillation is often caused by an alignment of ENSO and solar-cycle signals. The preindustrial climate state was simulated with constant solar forcing, however, Misios and Schmidt (2012) also found a TPQDO-like variability mode in the coupled atmosphere-ocean GCM ECHAM5/MPIOM, the progenitor of MPI-ESM, and described it as an internal mode of variability. The origin of the prominent 18-year covariability mode is a feature unknown so far. Large-amplitude modes of variability in BDC strength at periods of 10 and 18 years may explain the sharp peak in the histogram reflecting the linear BDC trends over 20- and 50-year periods in the preindustrial control simulation (see Fig. 5.6).

Generally, all substantial covariability in the LR configuration of MPI-ESM is produced at periods between 3 and 20 years (see Fig. 5.8). The fact that for almost every mode of variability in this range of periods the signal in the NINO 3.4 index leads the signal in the BDC strength, indicates that also low-frequency modes of variability are communicated from the troposphere-surface system to the stratosphere.

In the MR configuration of MPI-ESM, the amplitudes in the long-term covariability

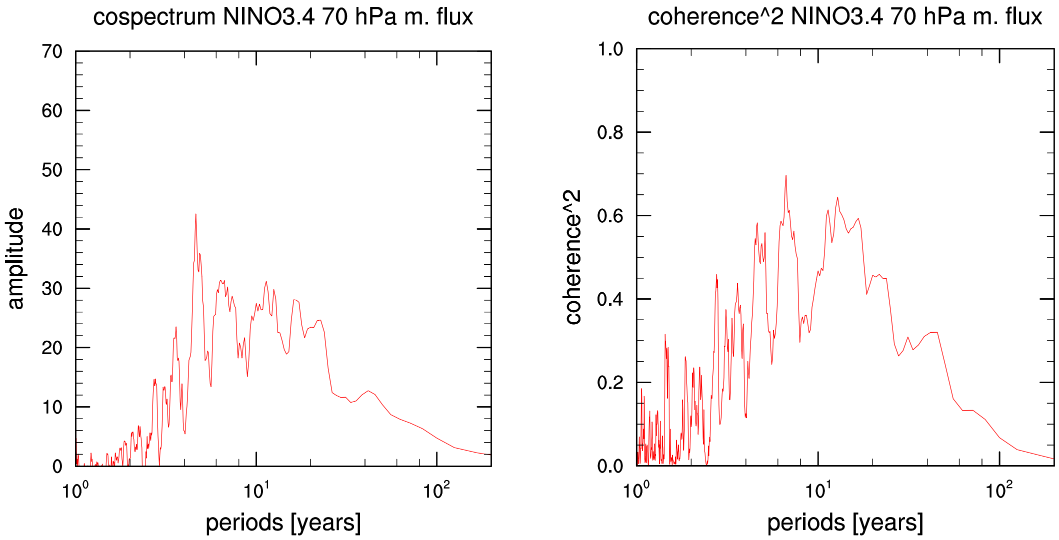

Figure 5.9: The cospectrum for the NINO3.4 index and the 70 hPa annual-mean total upward mass flux is shown (left) together with the associated squared coherence (right). The squared coherence is a measure for the significance of the covariability at a given frequency. The data was derived from the 500-year preindustrial control simulation performed with MPI-ESM in the MR model configuration.

spectrum are substantially weakened (see Fig. 5.9). As in the LR configuration, all substantial covariability is found at periods between 3 and 20 years, with the signal led by the NINO 3.4 index for almost all periods in this range. However, periods below 10 years here yield the most prominent contribution to the covariability spectrum. This may again be the result of the QBO, which is internally generated only in the MR configuration, and may diminish the coherence between the variability modes of the NINO3.4 index and the upward mass flux by modulating the tropical upwelling. However, as in the MR configuration also for the ocean-component of MPI-ESM, MPIOM, a different setup is applied (see Section 2.2), the simulation of the tropical SST variability itself may be different in the two configurations of MPI-ESM. The modes of variability in the NINO3.4 index (see Fig. 5.10) indeed corroborate this. While in both model configurations (LR and MR) substantial variability between 3 and 20 years is simulated, the amplitudes of the NINO3.4 index itself are generally larger in the LR configuration compared to the MR setup. Particularly at periods of 10 years or more, the simulated variability in the LR model is substantially enhanced, compared to the MR configuration.

In order to further visualise the communication of variability modes from the troposphere-surface system to the stratosphere, a wavelet analysis after Torrence and Compo (1998) is applied to the model output of both the LR (see Fig. 5.11) and MR (see Fig. 5.12) model configuration of MPI-ESM. In the LR configuration the coincidence of significant modes of variability for periods between 3 and 20 years in the 70 hPa upward mass flux and the NINO 3.4 index is readily apparent. Also the wavelet coherence (see Fig. 5.11) indicates strong evidence of an upward transmission of anomalies in the NINO 3.4 index. In the MR configuration (see Fig. 5.12), however, the connection between low-frequency variability modes in the NINO 3.4 index and

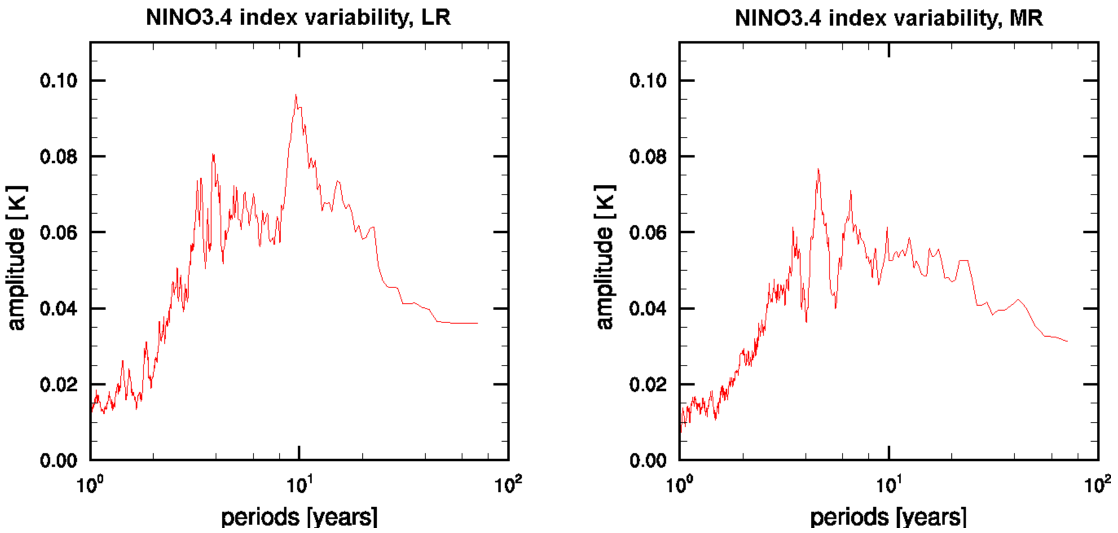

Figure 5.10: The modes of variability in the NINO3.4 index, computed via a Fourier analysis, are shown as derived from 500 years of the preindustrial control run in both the LR (left) and MR (right) configurations of the MPI-ESM model.

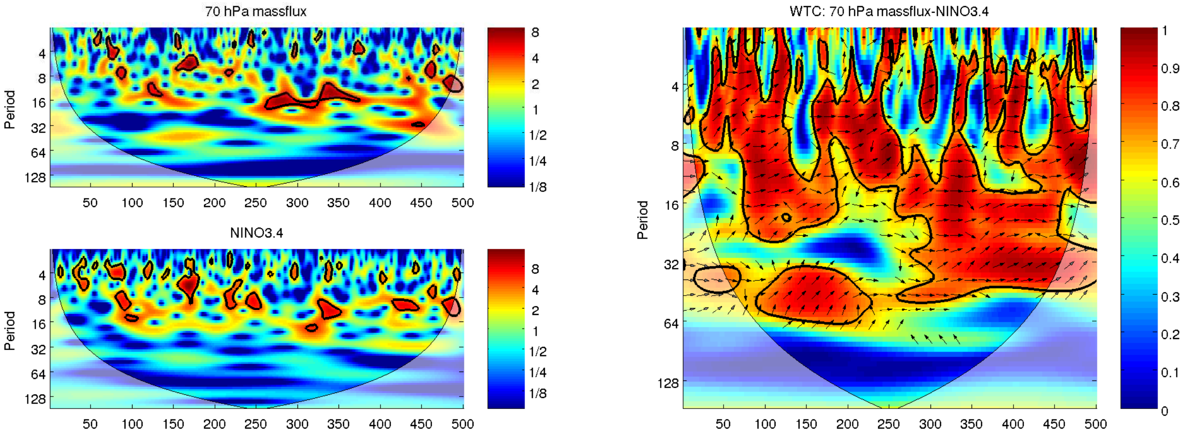

Figure 5.11: Variability spectra (left) derived via a wavelet analysis after Torrence and Compo (1998) for the 70 hPa total upward mass flux and the NINO3.4 index are shown together with the wavelet coherence (right) between the two quantities. The cone of influence is indicated by the thin solid line, while significances are marked with thick solid lines. The arrows depicted together with the wavelet coherence reflect the phase shift between the upward mass flux and the NINO3.4 index. An arrow pointing to the right indicates that the two quantities are in phase, while the angle (measured counterclockwise with respect to an arrow pointing to the right) of an arrow reflects a positive phase shift, which corresponds with a signal in the NINO3.4 index leading the signal in the upward mass flux. The data was derived from the 1000-year preindustrial control run simulated with MPI-ESM in the LR configuration.

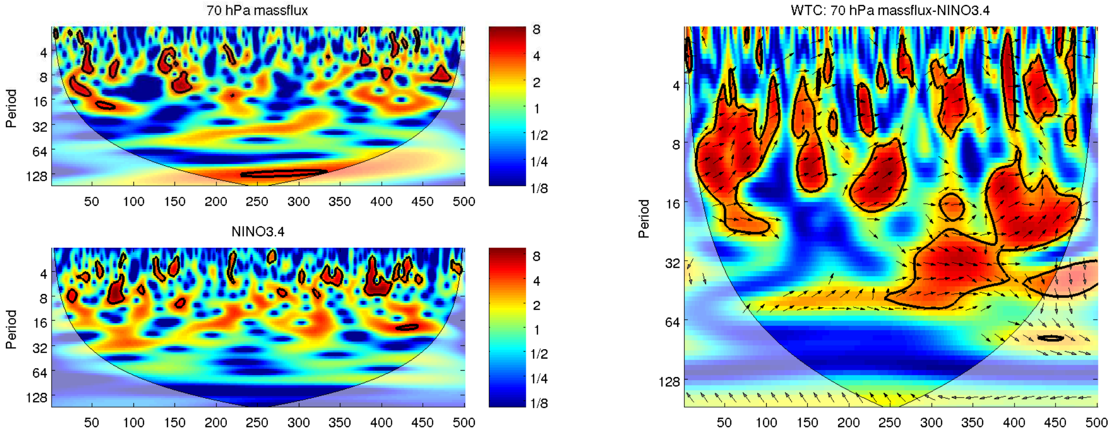

Figure 5.12: Variability spectra (left) derived via a wavelet analysis after Torrence and Compo (1998) for the 70 hPa total upward mass flux and the NINO3.4 index are shown together with the wavelet coherence (right) between the two quantities. The cone of influence is indicated by the thin solid line, while significances are marked with thick solid lines. The arrows depicted together with the wavelet coherence reflect the phase shift between the upward mass flux and the NINO3.4 index. An arrow pointing to the right indicates that the two quantities are in phase, while the angle (measured counterclockwise with respect to an arrow pointing to the right) of an arrow reflects a positive phase shift, which corresponds with a signal in the NINO3.4 index leading the signal in the upward mass flux. The data was derived from the 500-year preindustrial control run simulated with MPI-ESM in the MR configuration.

the upward mass flux is not as obvious as in the LR configuration. Also the wavelet coherence shows much less significant covariability compared to the LR configuration. This behaviour corroborates the results obtained from the cospectra (see Fig. 5.8 and 5.9). The covariability between tropical SSTs and BDC strength is diminished in the MR configuration compared to the LR model setup. The discrepancy between the two model configurations appears to be primarily due to the difference in the simulated tropical SST variability (see Fig. 5.10). The modulation of the tropical upwelling due to the internally generated QBO in the MR configuration, may play a secondary role here.

The multi-centennial preindustrial control simulations provide a unique possibility to investigate the significance of trends in BDC strength against the natural BDC variability, and the communication of long-term variability from the troposphere-surface system to the stratosphere. It turned out that datasets extending over at least 30 years with good spatial and temporal resolution are required to significantly distinguish a trend in BDC strength in the second half of the 20th century from natural BDC variability (see Section 5.2). The natural BDC variability was found to originate, at least partly, from tropical SST variability. The covariability of the BDC strength and the NINO3.4 index indicates substantial coupling between the troposphere-surface system and the stratosphere at long-term variability modes with periods between 3 and 20 years. The coupling is exerted upward for the vast majority of these periods and is substantially diminished in the MR configuration of MPI-ESM, compared to the LR configuration. This is primarily due to the tropical SST variability itself, as it is differently simulated in the two model configurations. A secondary contribution might originate from the modulation of the tropical upwelling due to the internally generated QBO in the MR configuration.

Chapter 6

Stratosphere-troposphere dynamical coupling in a changing climate

Since Charney and Drazin (1961) showed that the index of refraction for planetary waves is primarily controlled by the zonal-mean zonal winds, and Matsuno (1970) computed numerical solutions to the linearised wave propagation equation for realistic zonal wind profiles, upward propagating tropospheric dynamical disturbances are considered to be able to significantly alter the stratospheric state. On the winter hemisphere the zonal-mean zonal winds allow for an upward propagation of large-scale atmospheric waves, or *planetary waves*, far into the middle atmosphere. Here they eventually break or dissipate and, thus, decelerate the polar vortex. Periods of high planetary wave fluxes from the troposphere to the stratosphere may induce weak polar vortex events, which often coinicide with sudden stratospheric warmings (SSWs). On the other hand, periods of low planetary wave fluxes may induce strong polar vortex events. Due to the larger land-sea contrast on the northern hemisphere, planetary wave fluxes into the stratosphere are significantly stronger during midwinter on the northern hemisphere compared to the southern hemisphere. Thus, midwinter SSW events are much more likely to occur in the northern winter hemisphere.

The index of the Northern Annular Mode (NAM, see Section 3.5.2) can be considered as a measure for the strength of the stratospheric polar vortex. Negative NAM index anomalies correspond with a weak polar vortex, while positive anomalies in the NAM index correspond with a strong polar vortex. Baldwin and Dunkerton (1999) were the first to show that after the occurrence of an extreme stratospheric event the stratospheric disturbance may propagate downward and significantly affect the northern hemispheric middle to high latitude sea-level pressure field. The influence of a stratospheric event on the sea-level pressure field is in many cases reflected in the North Atlantic Oscillation (NAO) index, which is a key index for the weather and climate in Europe and Eurasia (e.g. Schnadt and Dameris, 2003). The significant impact of downward propagating stratospheric disturbances on the sea-level pressure field was corroborated and further evaluated in Baldwin and Dunkerton (2001) and other studies. However, since not all extreme stratospheric events are followed by a significant tropospheric disturbance, and the timescales involved in the downward propagation of the stratospheric signal vary significantly, the stratospheric impact on the troposphere-surface system turns out to be hardly predictable. How the mechanisms involved in stratosphere-troposphere dynamical coupling in the weeks before and after the occurrence of an extreme stratospheric event react to a changing climate, is so far not clear. Also the impact of the model configuration on the behaviour of the coupling between the stratosphere and the troposphere has not yet been systematically investigated.

In order to evaluate the dynamical coupling between the stratosphere and the troposphere, as well as its response to a GHG-induced changing climate, the downward propagation of the stratospheric disturbance after extreme stratospheric events is investigated in the following for different climate states and model configurations. First, the downward propagation of anomalies in the Northern Annular Mode (NAM) index, representing the strength of the polar vortex, is analysed in the ECHAM6 GCM (see Section 6.1.1). Then it is investigated how the frequency of extreme weak vortex events, which often coincide with SSWs, reacts to a changing climate (see Section 6.1.2). Furthermore, we shall evaluate the behaviour of stratospheric dynamics in the remote future as simulated with MPI-ESM in the RCP8.5 GHG emission scenario after 2100 (see Section 6.1.3). Eventually, it is shown how a future change in stratospheric dynamics may affect the troposphere-surface system (see Section 6.2).

6.1 Extreme stratospheric events

In Section 4 we studied the behaviour of the BDC in a changing climate and the underlying processes, which produce the BDC strengthening simulated by most state-of-the-art climate models. The GHG-induced tropospheric warming and simultaneous stratospheric cooling modifies the lower stratospheric meridional temperature gradient and causes a strengthening of the upper flanks of the subtropical jets via thermal wind balance (see Fig. 4.1). The change of the zonal-mean zonal wind field modifies the propagation conditions for large-scale planetary waves (Charney and Drazin, 1961). Particularly, the strengthening of the upper flanks of the subtropical jets allows for enhanced resolved wave activity flux from the troposphere to the stratosphere (e.g. Shepherd and McLandress, 2011). Since increased wave activity flux into the stratosphere implies increased wave dissipation or breaking at some altitude in the stratosphere or above, the most straightforward implication would be an increase in the frequency of weak polar vortex events, accompanied with an increased SSW frequency. In case the downward propagation characteristics of stratospheric disturbances are not too severely affected by the changing climate, this behaviour would in turn imply a negative shift in the North Atlantic Oscillation (NAO) index. We shall see that the predicted increase in SSW frequency is indeed simulated with MPI-ESM in the RCP4.5 and RCP8.5 scenarios. However, under the extreme climate change conditions in the remote future of the RCP8.5 scenario after 2100, a very different change in stratospheric dynamics occurs, which may have significant implications for the troposphere-surface system.

6.1.1 Downward propagation of anomalies in polar vortex strength

After the occurrence of an extreme event in the strength of the stratospheric polar vortex, the dynamical anomaly descends downward and often significantly affects the tropospheric state (e.g. Baldwin and Dunkerton, 1999). The downward propagation of weak and strong polar vortex anomalies is shown in Figure 6.1 for the present-day climate state, as simulated in different model configurations of the ECHAM6 GCM. These composite plots of weak and strong vortex events, defined by the excess of certain thresholds in the NAM index (see Section 3.5.2), clearly show the downward propagation of a stratospheric disturbance, which in most cases reaches the surface during the first 60 days after the occurrence of the event. As the timescale of the downward propagation varies significantly among the single events (see Tab. 6.1), and not all of the events show a significant disturbance reaching the surface, the tropospheric signal in the composite plots is usually not large. Nevertheless, the disturbance reaching the troposphere-surface system is larger on average in the L95 and L31 configurations compared to the L47 model configuration (see Fig. 6.1). However, it is important to emphasise here that the background state as well as the variability explained by the first EOF and the associated principal component time series, i.e. the NAM index, vary among the different time-slice simulations. Thus, a significantly different behaviour in terms of the underlying physics involved in the downward propagating NAM anomalies is hardly obtainable by comparing disturbances relative to the respective mean state of the associated time-slice simulation.

It is, however, apparent that in all model configurations a NAM anomaly of the opposite sign descends downward from the mesosphere after the occurrence of the actual stratospheric event. This implies that also the transition back to the “dynamical equilibrium” starts from above. After an extreme weak polar vortex event, the negative anomaly in zonal-mean zonal winds causes reduced wave activity flux into the stratosphere (Charney and Drazin, 1961). Thus, the recovery of the polar vortex may start in the upper stratosphere or mesosphere, before the wind regime is eventually reestablished also in the lower stratosphere.

Compared to ERA-40 reanalysis data (Baldwin and Thompson, 2009), the downward propagation of NAM anomalies is most realistically simulated in the L95 model configuration. In the L47 configuration, the fraction of the original stratospheric anomaly that reaches the troposphere-surface system is substantially smaller compared to ERA-40 data. In both ERA-40 data and in the L95 configuration the actual stratospheric event is preceded by an anomaly of the opposite sign. This preceding anomaly is not simulated in the L31 configuration.

How the downward propagating NAM anomalies on average react to a changing climate is depicted in Figure 6.2. The composite plots imply that for both weak and strong polar vortex anomalies a larger signal originating from the initial stratospheric disturbance reaches the troposphere-surface system in the future climate state compared to preindustrial conditions. However, considering again the broad range of timescales at which the stratospheric anomaly propagates downward (see Tab. 6.1), the observed behaviour could as well be an artefact of building the composite plots.

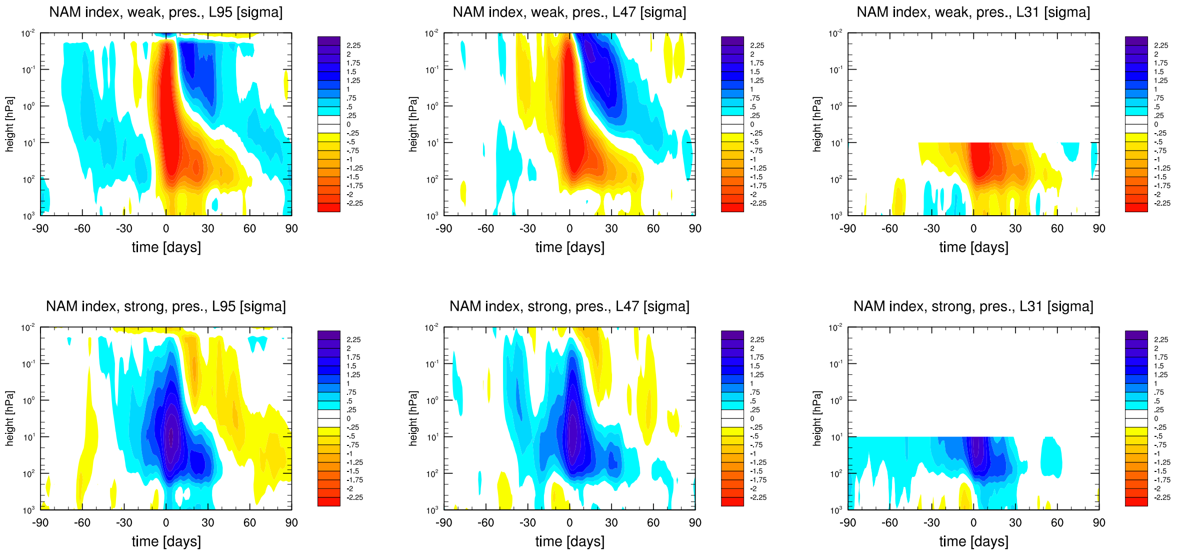

Figure 6.1: The Northern Annular Mode (NAM) index is shown for weak (upper panels) and strong (lower panels) vortex events, as computed level-by-level from the 50-year present-day time-slice simulation performed with the ECHAM6 GCM in the L95 (left), L47 (middle), and L31 (right) model configurations.

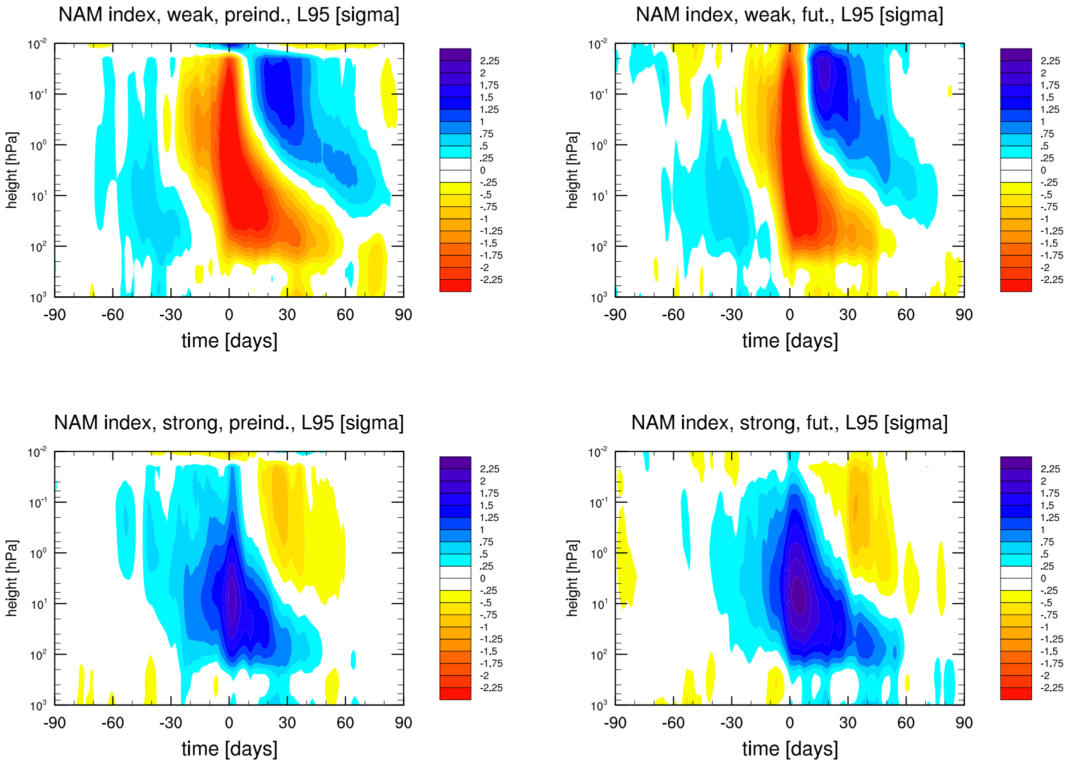

Figure 6.2: The NAM index is shown for weak (upper panels) and strong (lower panels) polar vortex events, as computed level-by-level from the 50-year preindustrial (left) and future (right) time-slice simulations performed with the ECHAM6 GCM in the L95 model configuration.

Due to the large case-to-case variability in the downward propagation speed of the stratospheric disturbance after weak and strong vortex events (see Tab. 6.1), no statistically significant change is found among the simulated climate states. Thus, in the following we shall focus more on the ratio of events affecting the lower troposphere in different climate states and model configurations. In order to investigate how many of the stratospheric events are followed by a dynamical disturbance in the lower troposphere, the events are separated into downward and non-downward propagating events by introducing a NAM threshold (-2.0/+2.0 σ for weak/strong vortex events, see Section 3.5.2 for more details) at 700 hPa during the 60 days after the initial stratospheric disturbance occurred. Figure 6.3 shows separate composite plots for downward and non-downward propagating extreme NAM events, as simulated in the L95 configuration of the ECHAM6 GCM. These plots clearly reflect that not all extreme stratospheric NAM events yield significant dynamical implications for the tropospheric state. After extreme weak non-downward propagating NAM events the tropospheric state, on average, even indicates slightly positive NAM anomalies, which is, however, due to construction of the plot. The composite plot of the non-downward propagating strong polar vortex events shows that at least some of the events precede downward-propagating weak vortex events. We shall further evaluate here how the ratio of downward propagating events is affected by both the climate state and the model configuration and, if the speed of the downward propagating stratospheric disturbances changes significantly among the time-slice simulations performed with ECHAM6.

The number of downward and non-downward propagating stratospheric polar vortex anomalies is shown in Table 6.1 together with the average downward propagation time of a stratospheric disturbance to the lower troposphere, as simulated for different climate states and model configurations. The average downward propagation time is considered here as the time shift between the stratospheric and the subsequent tropospheric disturbance, averaged over all downward propagating events (see above or Section 3.5.2 for the detailed definition). It turns out that the majority of the extreme stratospheric events is in all climate states and model configurations followed by a significant (at the 95% confidence level) tropospheric disturbance. The ratio of downward to non-downward propagating extreme stratospheric events does not depend significantly on the model configuration or the simulated climate state. The time lag between the stratospheric and the tropospheric disturbance shows large case-to-case variations, so that the speed of the downward propagating stratospheric disturbance can also not significantly be distinguished among the different climate states and model configurations.

The investigation of the downward propagation of a stratospheric disturbance in the different 50-year ECHAM6 time-slice simulations showed that neither the climate state nor the model configuration yields a significant impact on the speed of the downward propagation. However, in all simulations a majority of the extreme stratospheric events is followed by a significant disturbance in the lower troposphere. Thus, the model simulations imply that the stratosphere can be considered to have a measurable impact on the tropospheric state, at least during the 60 days after a majority of extreme events in stratospheric polar vortex strength. This behaviour is also found in the ERA-40 reanalysis dataset (Runde, 2012).

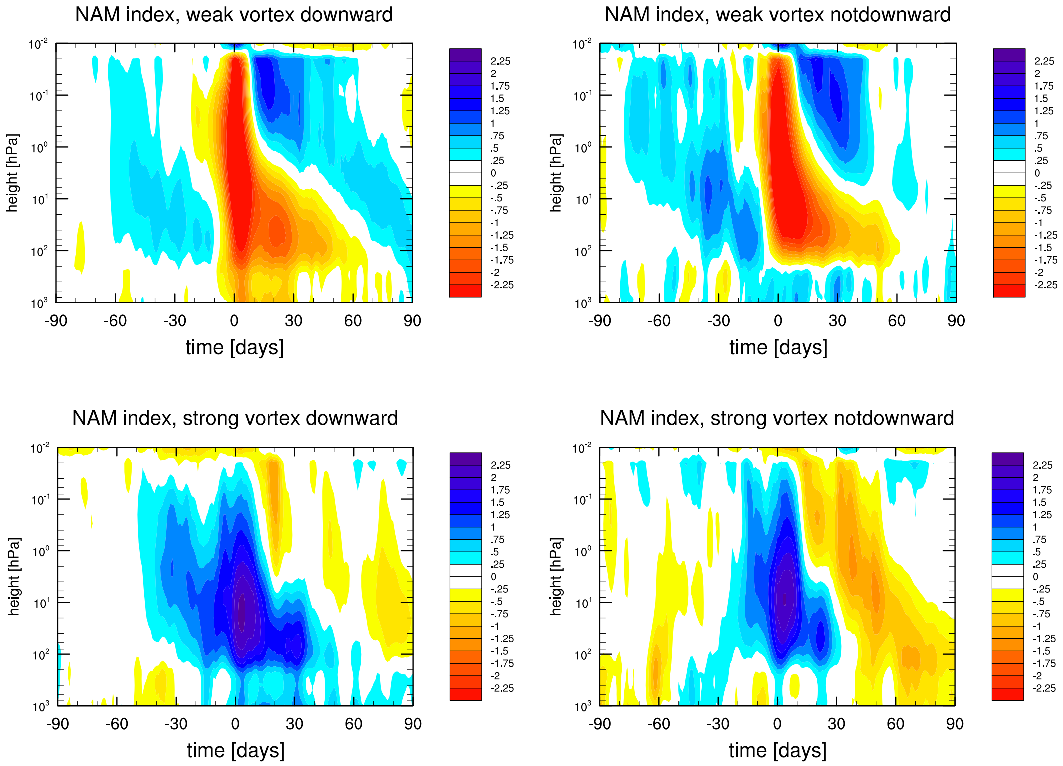

Figure 6.3: The NAM index is shown for weak (upper panels) and strong (lower panels) polar vortex events, as computed level-by-level from the 50-year present-day time-slice simulation performed with the ECHAM6 GCM in the L95 model configuration. Separate composites were plotted for downward propagating (left) and non-downward propagating (right) extreme NAM events.

Table 6.1: The number of downward and non-downward propagating weak/strong vortex events is shown for different climate states as simulated with different ECHAM6 model configurations. Additionally, the average time lag between the stratospheric and the tropospheric disturbance is given, calculated from all downward-propagating extreme NAM events in the respective time-slice simulation. The number in brackets indicates one standard deviation.

Model	Climate state	Weak dw./n-dw.	Strong dw./n-dw.	Time lag (days) weak/strong
ECHAM6 L95	1860	12 / 11	27 / 9	16.9 (± 14.2) / 26.2 (± 19.2)
	1990	20 / 10	18 / 15	12.1 (± 14.2) / 17.3 (± 14.6)
	2050	11 / 10	19 / 10	21.0 (± 16.1) / 28.9 (± 19.7)
ECHAM6 L47	1860	18 / 13	27 / 20	24.3 (± 17.0) / 22.1 (± 16.9)
	1990	17 / 14	23 / 14	16.5 (± 14.8) / 26.6 (± 16.9)
	2050	19 / 12	26 / 15	25.3 (± 22.1) / 20.3 (± 16.6)
ECHAM6 L31	1860	13 / 10	20 / 18	27.6 (± 17.7) / 25.8 (± 22.2)
	1990	20 / 7	18 / 15	17.3 (± 16.3) / 16.6 (± 14.8)
	2050	11 / 9	22 / 13	10.3 (± 14.4) / 23.5 (± 19.3)

As the NAM index merely yields a measure of the strength of the polar vortex relative to the mean vortex strength, it is not well-suited for a comparison of the frequency of extreme stratospheric events in different climate states. As for weak polar vortex events, however, the occurrence of SSW events, which usually coincide with weak vortex events, yields an objective measure of the frequency of extreme stratospheric events. In the following it is analysed how the frequency of extreme weak polar vortex events and, thus, the potential impact of stratospheric dynamics on the tropospheric state reacts to a changing climate.

6.1.2 Sudden stratospheric warmings in a changing climate

In order to evaluate how the frequency of extreme stratospheric events, such as SSWs coinciding with weak vortex events, reacts to a changing climate, we first evaluate if the ECHAM6 GCM is capable of simulating SSWs realistically. Thus, the frequency and monthly distribution of the two types of SSWs, vortex displacements and vortex splits (see Section 3.5.1), are compared between ECHAM6 model data and reanalyses. The frequency and monthly distribution of SSWs for ERA-40 and NCEP/NCAR reanalysis datasets is shown in Figure 6.4, as analysed by Charlton and Polvani (2007), for the two types of SSW events. The SSW detection algorithm of Charlton and Polvani (2007) is very similar to the one compiled within this study (see Section 3.5.1). In both algorithms an SSW event is triggered by the reversal of the zonal-mean zonal wind at 60°N and 10 hPa. The only difference between the two algorithms is the defined recovery time of the polar vortex after an SSW event. While in the algorithm of Charlton and Polvani (2007, see their corrigendum) a time interval of 20 consecutive days of westerly winds after an SSW event is necessary, before a new event can be defined, the algorithm compiled within this study uses a vortex recovery time of 10 days. This difference has, however, no impact on the number of SSW events obtained for, e.g., the ERA-40 dataset.

For the classification of SSW events Charlton and Polvani (2007) compiled an algorithm based on absolute vorticity. As their algorithm was both not accessible for the context of this study and hardly reproducible after their description, a new SSW classification algorithm based on geopotential height was compiled within this study (see Appendix). It turns out that the results obtained for the ERA-40 dataset (see Fig. 6.5) compare reasonably well with the results of Charlton and Polvani (2007). Generally, the reanalysis datasets show an SSW occurrence frequency of about 6.4 events per decade (Charlton and Polvani, 2007), which is roughly equally distributed among vortex displacements and splits (as classified by Charlton and Polvani, 2007). The monthly SSW distribution reflects a peak in midwinter and only very few events in early winter (see Figs. 6.4 and 6.5). While the distribution of SSW displacement events is rather flat, the distribution of SSW splits appears to be responsible for the overall monthly SSW distribution, as it shows a sharp peak in midwinter. Compared to the SSW classification algorithm of Charlton and Polvani (2007), the classification algorithm compiled within this study shows a bias towards vortex splitting events. A subjective analysis of the polar vortex during the SSW events, however, showed that all SSW events differently categorised by the two algorithms indeed coincide with a

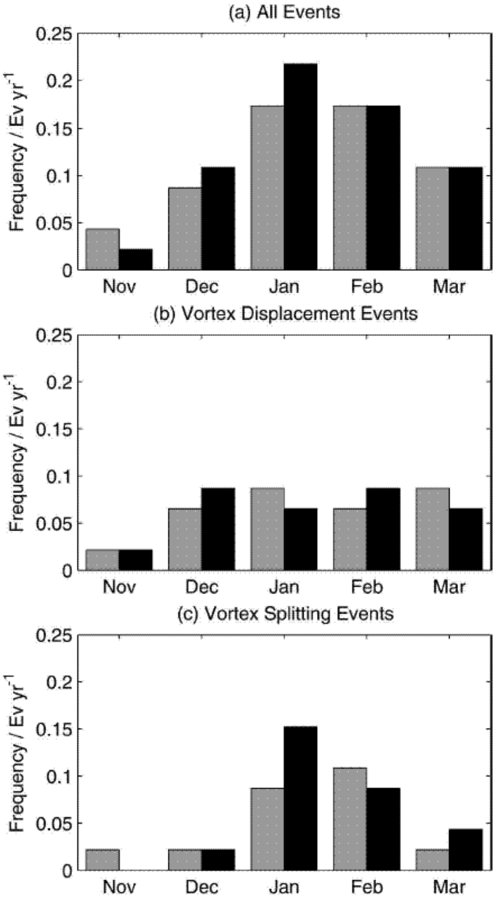

Figure 6.4: The frequency and monthly distribution of sudden stratospheric warming (SSW) events is shown, as derived from NCEP/NCAR (grey) and ERA-40 (black) reanalysis datasets. The depicted histograms reflect the distribution of the total number of SSW events (a), events classified as vortex displacements (b), and events classified as vortex splits (c). The applied SSW classification algorithm is based on the geometry of the absolute vorticity field (Charlton and Polvani, 2007). [Figure from Charlton and Polvani (2007)]

split of the polar vortex. Nevertheless, the classification of SSWs based on geometric measures using empirical parameters (see Charlton and Polvani, 2007; or Appendix), always contains a subjective component.

The SSW frequency and monthly distribution as simulated for the present-day climate state in the L95 and L47 model configurations with ECHAM6 are shown in Figure 6.6. A comparison of the model results with reanalysis data (see Fig. 6.5) indicates that the main features of the monthly distribution, such as the midwinter peak or the relative contribution of the different event types, are simulated relatively realistically. The SSW occurrence frequency, in turn, is larger by up to 60% in the L95 model configuration (30% in L47) compared to reanalysis data. One has to note here, however, that the model was run under stationary present-day climate conditions (see Section 2.4.1), while the reanalysis data covers almost the entire second half of the 20th century. The stationary climate conditions of the model run could simply be more favourable for SSW events to occur. We shall see later that the SSW frequency obtained from the CMIP5 simulations (see Section 2.4.2), performed with ECHAM6 in the framework of

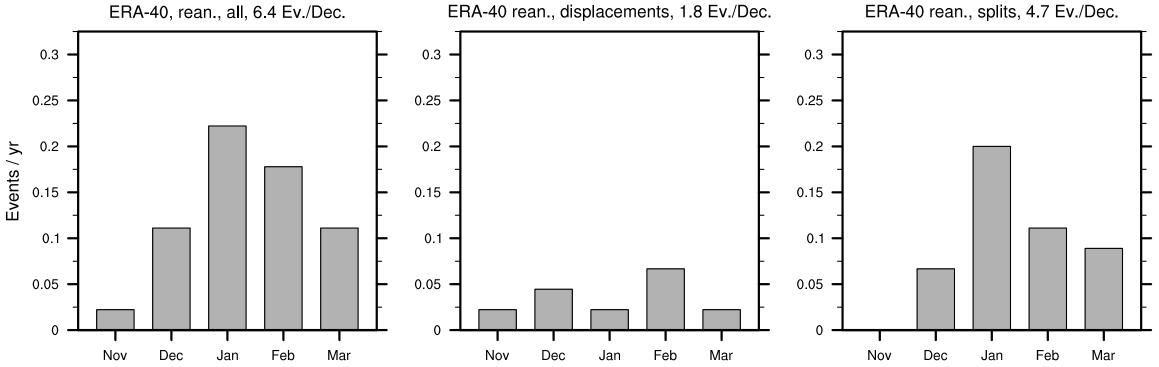

Figure 6.5: The frequency and monthly distribution of SSW events is shown, as derived from ERA-40 reanalysis data. The depicted histograms reflect the distribution of the total number of SSW events (left), events classified as vortex displacements (middle), and events classified as vortex splits (right). The applied SSW classification algorithm is based on the geometry of the geopotential height field (see Appendix).

the Earth System Model MPI-ESM, compares well with reanalysis datasets.

Having verified the capability of the ECHAM6 GCM to simulate SSW events realistically, the behaviour of the SSW frequency and monthly distribution in a changing climate is investigated in the following. Figure 6.7 shows the results of the SSW analysis for both preindustrial and future climate states, as simulated in the L95 model configuration. In both climate states the monthly SSW distribution resembles the distribution of reanalysis data (see Fig. 6.5) by exhibiting the peak occurrence frequency in midwinter. In the preindustrial climate state both the relative contribution of the event types to the overall monthly distribution as well as the SSW frequency are very similar to reanalysis data. In the future time slice the SSW frequency increases to 12.7 SSW events per decade, which is largely due to an increase in SSW displacement events. As SSW displacements reflect a wave number 1 pattern (see Section 3.5.1), the conditions for wave propagation appear to have changed in a way that more wave activity associated with wave number 1 is able to propagate into the middle stratosphere in the future northern winter hemisphere.

To investigate how the interaction of large-scale waves with the zonal-mean flow and, thus, the conditions for large-scale wave propagation react to a changing climate, the Eliassen-Palm flux (EP flux) and its divergence (see Section 3.1.2) are evaluated in the following.

The dissipation and breaking of large-scale atmospheric waves propagating upward from the troposphere to the middle atmosphere weaken the polar vortex. In extreme cases the zonal-mean zonal wind at 60°N and 10 hPa is reversed and an SSW event occurs (see Section 3.5.1). In order to visualise the interaction between large-scale waves and the zonal-mean flow, an assessment of the EP flux and its divergence turns out to be a useful tool (see Section 3.1.2). In Figure 6.8 the DJF-mean EP-flux vectors scaled by density are depicted together with the drag exerted by resolved waves on the zonal-mean flow, as derived from the present-day time-slice simulations with the L47 and L95 configurations of the ECHAM6 GCM. In both configurations the upward propagation of resolved waves and their decelerating effect on the polar vortex in the

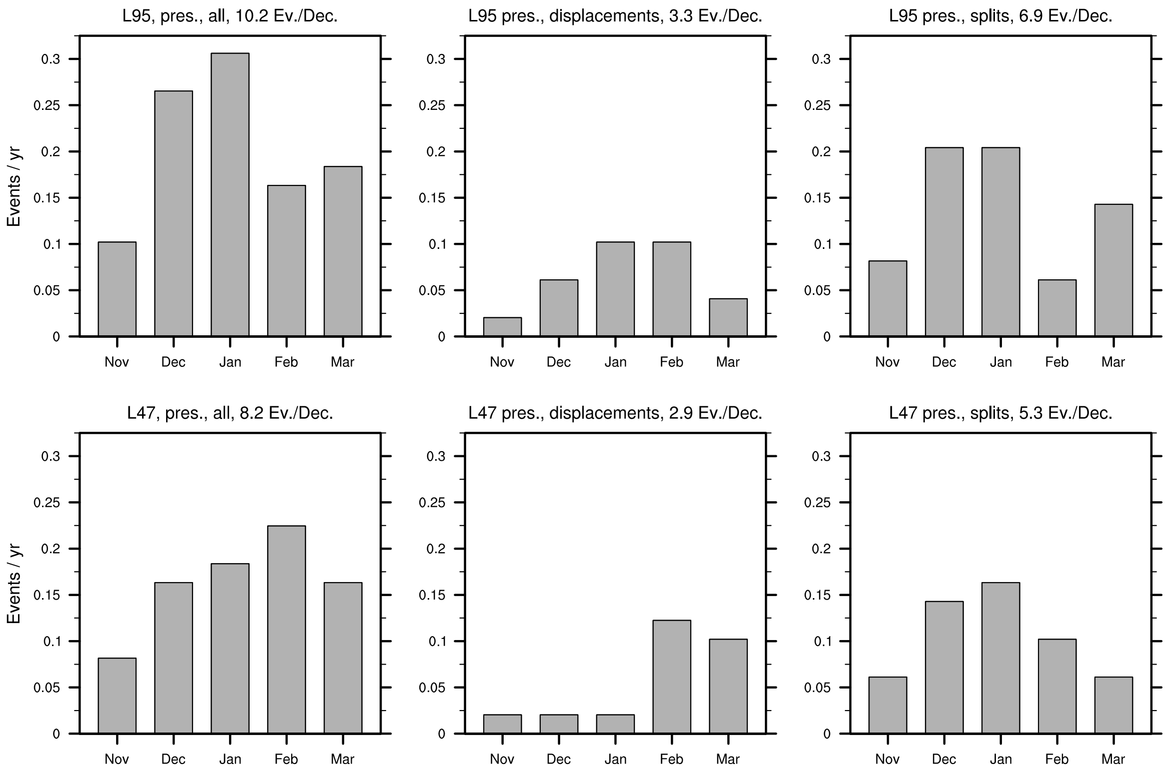

Figure 6.6: The frequency and monthly distribution of SSW events is shown, as derived from the 50-year present-day time-slice simulations performed with the ECHAM6 GCM in the L95 (upper panels) and L47 (lower panels) model configurations. The depicted histograms reflect the distribution of the total number of SSW events (left), events classified as vortex displacements (middle), and events classified as vortex splits (right). The applied SSW classification algorithm is based on the geometry of the geopotential height field (see Appendix).

northern middle atmosphere is readily apparent. In the L95 configuration smaller structures in the resolved wave drag compared to the L47 model configuration show up, which is likely to be related to the higher vertical resolution.

The associated change in DJF-mean resolved wave drag from the preindustrial to the future climate state as simulated in the L47 and L95 configurations of ECHAM6, is depicted in Figure 6.9. In both model configurations the DJF-mean deceleration of the polar vortex is enhanced in the future climate state, which corresponds with the simulated increase in SSW frequency. The change pattern in the troposphere is likely to reflect the upward shift of the critical layers in a changing climate, which was extensively discussed in Section 4.

The ECHAM6 time-slice simulations performed within this study (see Section 2.4.1) imply that a GHG-induced climate change not only causes an acceleration of the Brewer-Dobson Circulation (see Section 4.2), but also leads to a stronger deceleration of the stratospheric polar vortex, coinciding with an increase in frequency of SSW events. Whether this behaviour also holds for extreme climate change conditions in the remote future simulated in the RCP8.5 scenario, is investigated in the following.

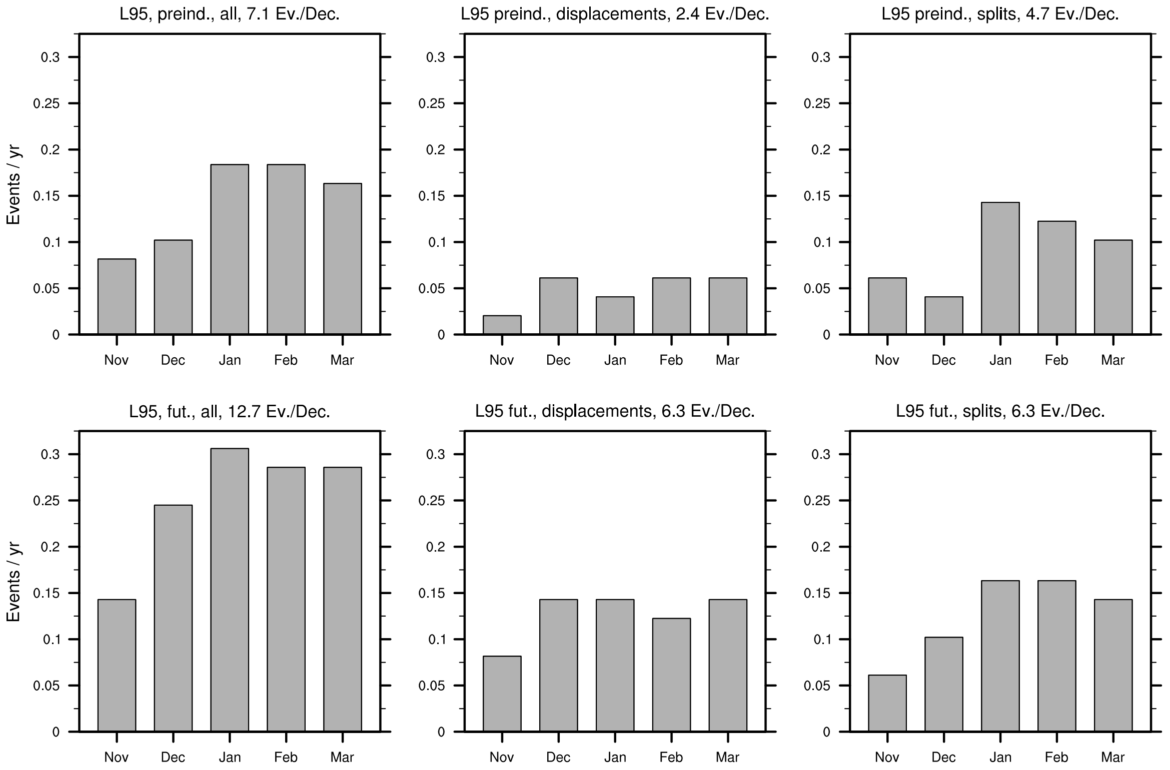

Figure 6.7: The frequency and monthly distribution of SSW events is shown, as derived from the 50-year preindustrial (upper panels) and future (lower panels) time-slice simulations performed with the ECHAM6 GCM in the L95 model configuration. The depicted histograms reflect the distribution of the total number of SSW events (left), events classified as vortex displacements (middle), and events classified as vortex splits (right). The applied SSW classification algorithm is based on the geometry of the geopotential height field (see Appendix).

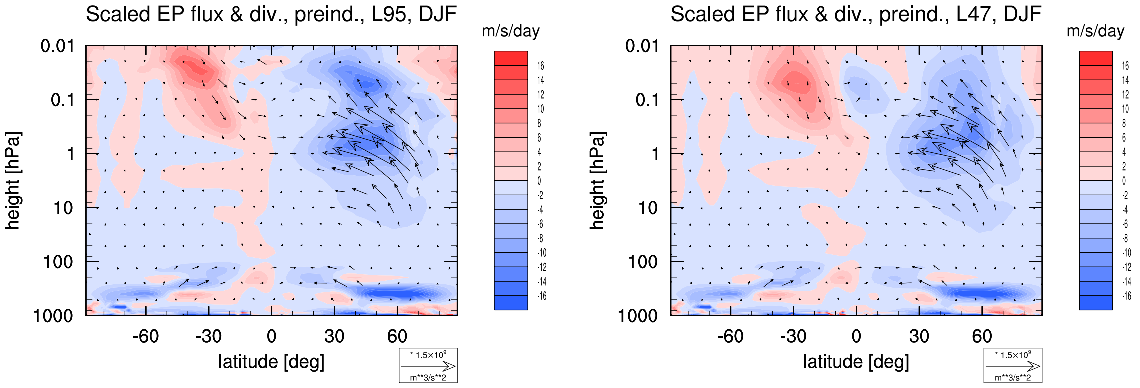

Figure 6.8: The DJF-mean Eliassen-Palm flux (EP flux) scaled by density is depicted (arrows) together with the resolved wave drag associated with the EP flux divergence (contours). The data was derived from the 50-year preindustrial time-slice simulation performed with the ECHAM6 GCM in the L95 (left) and L47 (right) model configurations.

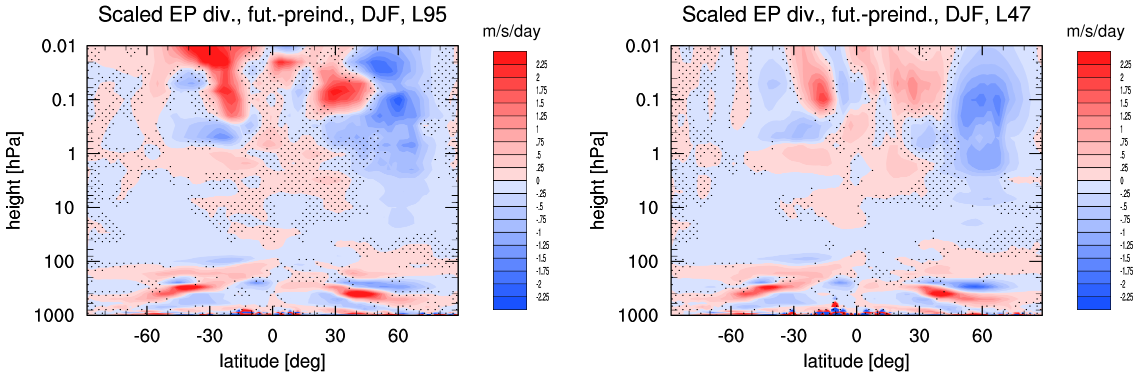

Figure 6.9: The change in DJF-mean resolved wave drag associated with the EP flux divergence from the preindustrial to the future climate state is shown, as derived from 50-year time-slice simulations performed with the ECHAM6 GCM in the L95 (left) and L47 (right) model configurations. Dotted regions indicate that the change is not significant at the 95% confidence level.

6.1.3 Stratosphere dynamics under extreme climate change

In order to be able to quantify the significance of changes in stratospheric dynamics in the remote future of the RCP8.5 scenario, as simulated with MPI-ESM, the occurrence frequency of SSW events and its natural variability are first evaluated in the stationary multi-centennial preindustrial control simulation. It turns out that in the preindustrial control run performed with the LR configuration of MPI-ESM the average number of SSW events per decade is the same as in the ERA-40 reanalysis dataset (see Fig. 6.5). Merely the monthly distribution of events differs from reanalysis data, as it rather shows a flat distribution than a midwinter peak (see Fig. 6.10). As decadal variability in the occurrence of SSWs is usually large, significant trends in SSW frequency can be masked by low-frequency variability in SSW frequency. To evaluate the SSW low-frequency variability, a wavelet analysis after Torrence and Compo (1998) is applied here. The preindustrial control simulation shows significant long-term variability in SSW frequency at periods of 40-50 years (see Fig. 6.11). This result is very similar to the one obtained for the multi-centennial control simulation with the coupled atmosphere-ocean GCM EGMAM (Schimanke et al., 2011), and provides a good basis to assess the significance of changes in SSW frequency derived from the transient RCP scenario simulations with MPI-ESM, which shall be analysed in the following.

In the second half of the 21st century both the RCP4.5 and RCP8.5 scenario show an increase in SSW frequency of roughly 50% (see Fig. 6.12) compared to the preindustrial control simulation (see Fig. 6.10). In the RCP4.5 scenario the monthly SSW distribution is rather similar to the one shown by reanalysis data (see Fig. 6.5), while the distribution of SSW events in the RCP8.5 scenario exhibits a slight shift to the late winter. Evaluating the remote future (2100-2300) in these scenario simulations shows no significant difference to the second half of the 21st century for the RCP4.5 scenario. Since a constant radiative forcing is assumed for the RCP4.5 scenario after 2100 (see Section 2.4.2), this is not a surprising result. The monthly SSW distribution still exhibits a midwinter peak and the SSW frequency is still roughly 50% increased in the RCP4.5 scenario after 2100 compared to the preindustrial climate state. In the

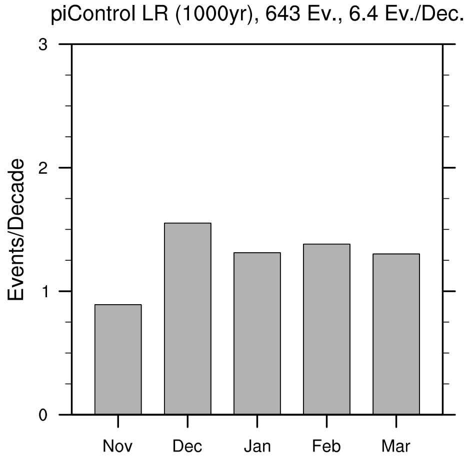

Figure 6.10: The SSW frequency and monthly distribution, as derived from the 1000-year preindustrial control simulation performed with MPI-ESM in the LR configuration, is shown.

RCP8.5 scenario, however, a remarkable change in both SSW frequency and monthly distribution occurs. The SSW frequency decreases by almost 50% compared to the second half of the 21st century coinciding with a remarkable shift in monthly SSW distribution towards the late winter. This behaviour is counterintuitive to our previous conclusion that the increased large-scale wave activity flux from the troposphere to the stratosphere causes increased wave dissipation and, thus, stronger deceleration of the zonal mean flow in the northern winter stratosphere, which would be reflected by an increase in SSW frequency. In order to evaluate what change in stratospheric dynamics could be responsible for the behaviour of the SSW frequency and monthly distribution in the remote future of the RCP8.5 scenario, the impact of resolved waves on the zonal mean flow and its change under the extreme climate change conditions of the RCP8.5 scenario after 2100 are analysed in the following.

The DJF-mean resolved wave activity flux, the EP flux (see Section 3.1.2), is shown in Figure 6.13 together with the tendency the resolved waves exert on the zonal mean flow in the preindustrial control simulation. The upward propagating large-scale waves as well as their decelerating effect on the polar vortex in the middle atmosphere are readily apparent. As the dissipation and breaking of large-scale waves is considered to cause SSW events, the relatively rapid change in SSW frequency, as observed after 2100 in the RCP8.5 scenario (see Fig. 6.12), is expected to be reflected in the resolved wave drag at 60°N and 10 hPa, where the definition for the occurrence of SSW events refers to (see Section 3.5.1).

The resolved wave drag indicates a slightly but significantly enhanced deceleration of the zonal-mean flow in the DJF-mean at 60°N and 10 hPa from the preindustrial climate state to both the near (2050-2100) and the remote future (2100-2300) in the RCP8.5 scenario (see Fig. 6.14). This behaviour would, however, rather suggest a similarly enhanced SSW frequency also in the remote future of the RCP8.5 scenario. Generally, the change pattern obtained for the two time periods in the RCP8.5 scenario appears to be similar to the one derived for the difference between preindustrial and future time-slice simulations with ECHAM6 (see Fig. 6.9), with a conspicuously stronger deceleration of the polar vortex in the upper stratosphere and mesosphere

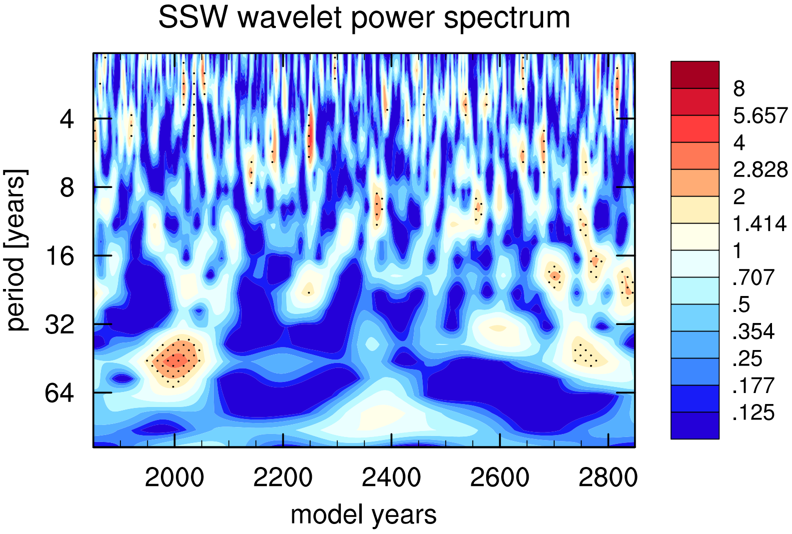

Figure 6.11: The wavelet power spectrum of SSW events per winter, computed after Torrence and Compo (1998), is depicted. Dotted regions represent significance at the 95% level.

in the RCP8.5 scenario after 2100. As a comprehensive explanation for the relatively rapid decrease in SSW frequency after 2100 can not be derived from the change in DJF-mean resolved wave drag, the climatological zonal-mean zonal wind together with the climatological resolved wave drag exerted on the zonal mean flow at 60°N and 10 hPa is evaluated in the following.

The change in the climatological zonal-mean zonal wind reveals that under the extreme climate change conditions of the RCP8.5 scenario after 2100 the zonal-mean wind field is enhanced by up to 10 m/s from early to midwinter, compared to preindustrial conditions in the region where the definition of the occurrence of SSW events refers to (see Fig. 6.16). It turns out that this strengthening of the zonal-mean zonal wind is a consequence of the strengthening of the upper flanks of the subtropical jets, which is a robust response to a GHG-induced climate change and extends even into the high-latitude middle stratosphere under the extreme climate change conditions of the RCP8.5 scenario after 2100 (see Fig. 6.15). The zonal-mean zonal wind increase is accompanied by a modification of the conditions for large-scale wave propagation in this region. Considering the similar response of the resolved wave drag before and after 2100 in the RCP8.5 scenario at 60°N and 10 hPa, however, the simulated increase in zonal-mean zonal winds appears to yield the stronger contribution to the observed change in the frequency of SSW events. A modification of wave propagation conditions due to the enhanced zonal-mean zonal winds is clearly reflected in the resolved wave drag in this region during early to midwinter (see Fig. 6.16). However, it can not be entirely disentangled here whether the strengthening of the zonal-mean zonal wind reduces the large-scale wave dissipation, or if reduced large-scale wave dissipation allows for increased zonal-mean zonal winds. In order to fully resolve this cause-and-effect relationship, a detailed investigation of the large-scale wave fluxes into the stratosphere would be required.

Starting in midwinter the deceleration exerted by resolved waves on the zonal mean

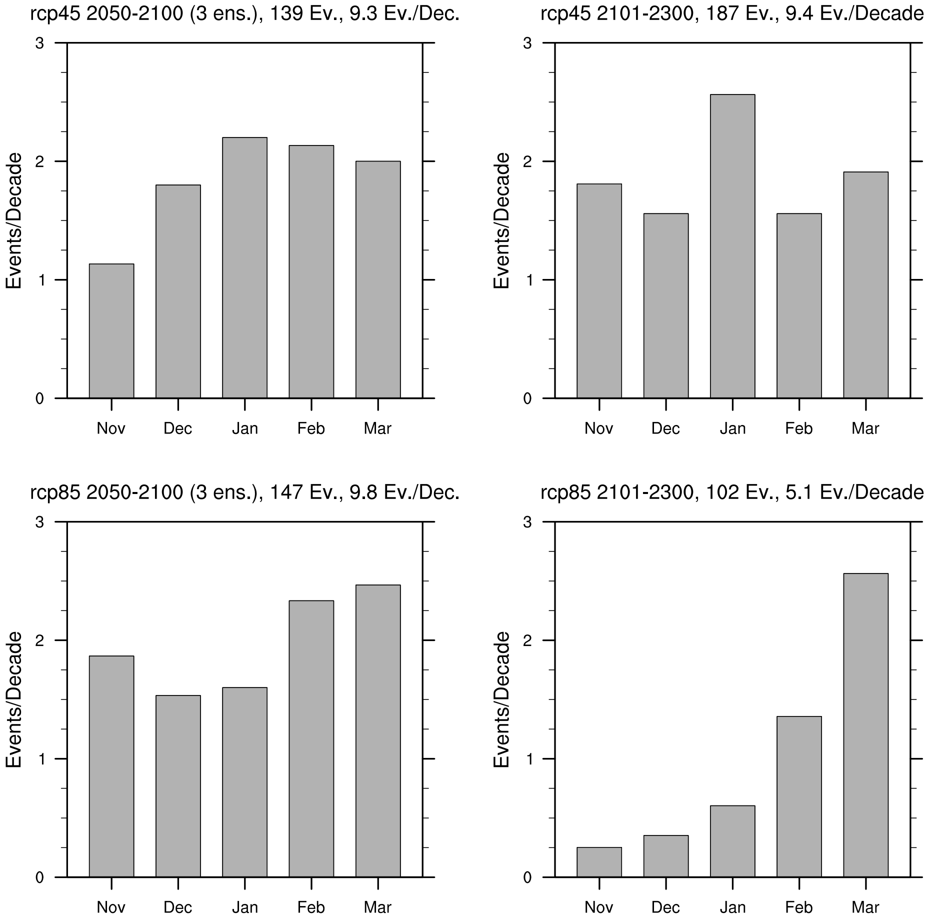

Figure 6.12: The SSW frequency and monthly distribution is shown for the RCP4.5 (upper panels) and RCP8.5 (lower panels) scenario simulations in the LR model configuration of MPI-ESM. The results are split up into two time periods. The first analysed period (left) covers the years 2050-2100 (simulated years of the 3 ensemble members were merged), while the second period (right) covers the time from 2100 to 2300 as simulated in the extended ensemble member (see Section 2.4.2).

flow exceeds the according wave drag under preindustrial conditions, corresponding with a steeper decrease in zonal-mean zonal wind in the RCP8.5 scenario after 2100. This yields an explanation for the remarkable shift of the SSW monthly distribution towards the late winter, when even an increase in SSW events is simulated after 2100 (see Fig. 6.12).

Thus, the analyses carried out in this section showed that the response of the stratosphere to a GHG-induced changing climate may be non-linear under the extreme climate change conditions, as simulated in the RCP8.5 scenario after 2100. The strengthening of the upper flanks of the subtropical jets allows for more wave propagation from the troposphere to the stratosphere where, initially, the increased wave dissipation causes on average a stronger deceleration of the polar vortex and, thus, an increase in SSW frequency by up to 50% at the end of the 21st century. After 2100, however, the strengthening of the upper flank of the subtropical jets extends up into the middle stratosphere, exceeding the effect of increased wave dissipation in the region where SSW events are defined. This leads to a relatively rapid reduction of SSW events after

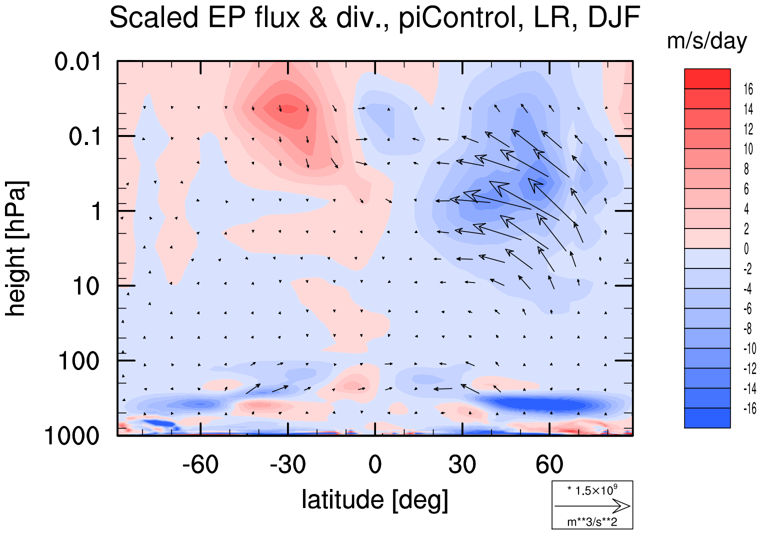

Figure 6.13: The DJF-mean EP flux scaled by density is depicted (arrows) together with the resolved wave drag associated with the EP flux divergence (contours). The data represents the multi-centennial DJF-mean of the preindustrial control simulation performed with MPI-ESM in the LR model configuration.

2100 coinciding with a remarkable shift in the SSW monthly distribution towards the late winter. Another consequence of this behaviour might be that some SSW events may occur in April or May.

As the exact region where the definition of the occurrence of SSW events refers to is to some extent arbitrary, one may argue that the observed behaviour simply reflects a continuous upward shift of the critical layers for wave dissipation, which at some point eventually affects the region where SSWs are defined. However, we shall see in the next section that the relatively rapid change in SSW frequency and monthly distribution after 2100 coincides with another relatively sharp transition in the troposphere-surface system.

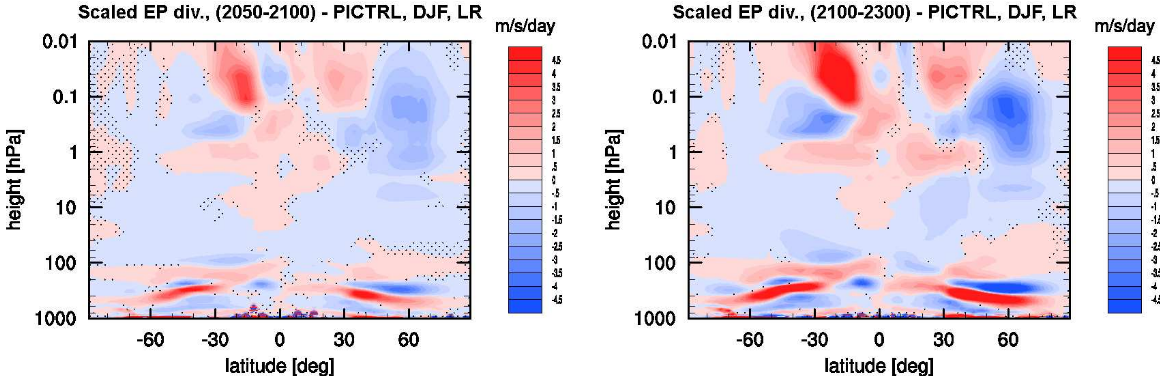

Figure 6.14: The change in DJF-mean resolved wave drag associated with the EP flux divergence from the preindustrial climate state to the future climate state (left: average over 2050-2100, right: average over 2100-2300), as simulated in the LR configuration of MPI-ESM in the extended RCP8.5 scenario, is shown. Dotted regions indicate that the change is not significant at the 95% confidence level.

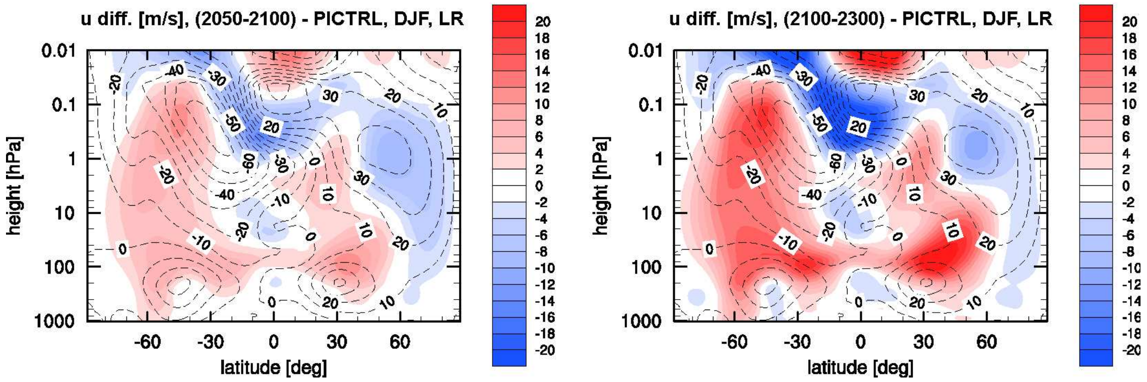

Figure 6.15: The change in DJF-mean zonal-mean zonal wind (colors) from the preindustrial climate state to the future climate state (left: average over 2050-2100, right: average over 2100-2300), as simulated in the LR configuration of MPI-ESM in the extended RCP8.5 scenario, is shown. The dashed contours represent the zonal-mean zonal wind field, as derived from the preindustrial control simulation.

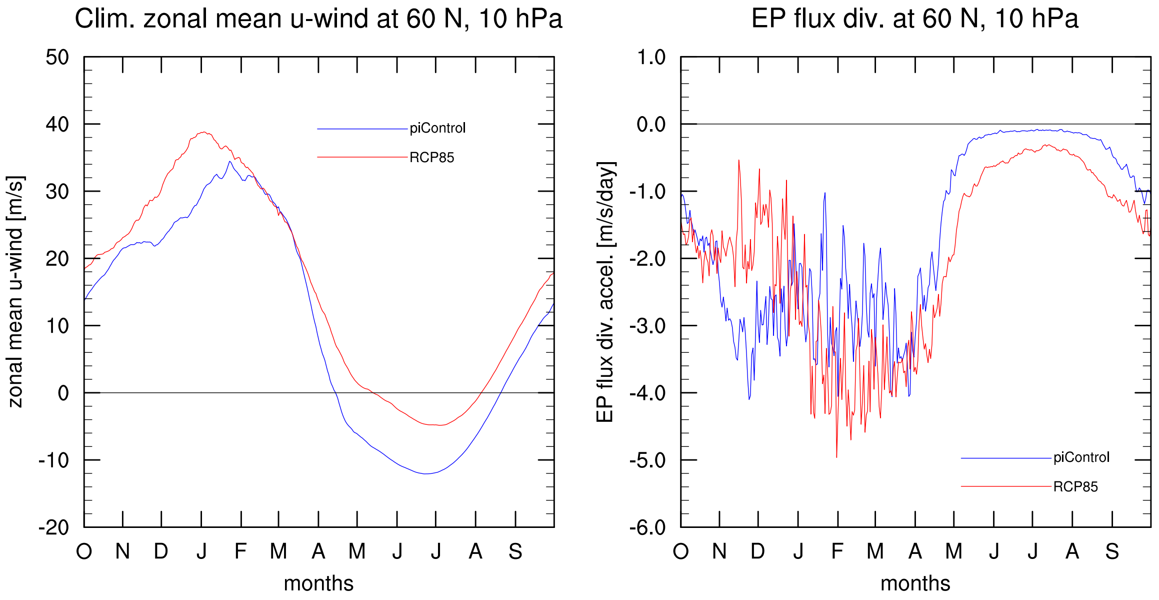

Figure 6.16: The climatological zonal-mean zonal wind (left) as well as the drag exerted by resolved waves on the zonal mean flow (right) at 60°N and 10 hPa is shown. The data was derived from 200 years of the 1000-year preindustrial control run (blue) and from the RCP8.5 scenario simulation (red, computed from the years 2100-2300).

6.2 Implications for the troposphere-surface system

Baldwin and Dunkerton (1999) were the first to show that, after the occurrence of an extreme stratospheric event, the stratospheric dynamical disturbance may propagate downward and cause a significant impact on the troposphere-surface system. This impact is, e.g., reflected in the northern hemispheric middle to high latitude sea-level pressure field. The North Atlantic Oscillation (NAO, see Section 3.5.3) index, which is a key index for the weather and climate in Europe and Eurasia (e.g. Schnadt and Dameris, 2003), can be used to quantify the anomaly in the sea-level pressure field after the occurrence of an extreme stratospheric event. Thus, the impact of stratospheric dynamical disturbances on surface weather and climate can be assessed. A positive anomaly in the NAO index reflects an increase in sea-level pressure difference between the low-pressure system centered over Iceland and the high-pressure system centered over the Azores (see Fig. 3.16, Section 3.5.3). This implicates enhanced westerlies over the North Atlantic corresponding with increased eastward transport of warm and moist air, which causes mild winters in central and northern Europe and Eurasia.

In Figure 6.17 the NAO index, represented by the first principal component time series of DJF-mean sea-level pressure anomalies over the North Atlantic (see Section 3.5.3 for the exact definition), is depicted together with the associated spatial pattern, as derived for the historical simulation with MPI-ESM extended with the RCP8.5 scenario simulation until 2300. While the NAO spatial pattern resembles the one derived for the preindustrial climate state (see Fig. 3.16), the most prominent feature here is the remarkable shift in the NAO to more positive phases after 2100, coinciding with the abrupt decrease in SSW events (see Fig. 6.12). Considering that downward propagating dynamical disturbances after SSW events cause negative anomalies in the NAO index, the abrupt increase in the NAO index in the RCP8.5 scenario after 2100 may be a direct consequence of the decrease in SSW events. This indicates for the first time how a future change in stratospheric dynamics, as simulated under the extreme climate change conditions of the RCP8.5 scenario after 2100, may affect the troposphere-surface system. However, the obtained results do not entirely resolve the cause-and-effect relationship. Although the evaluation of the SSW frequency and the NAO index indicate a simultaneous change, it is eventually not entirely clear whether the signal is transported from the stratosphere to the troposphere, or vice versa. A further set of sensitivity simulations would need to be performed, in order to better separate causes from effects here. Nevertheless, the positive shift in the NAO index, accompanied with the decrease in SSW events, would imply enhanced westerlies over the North Atlantic and, thus, more mild winters in central and northern Europe in the RCP8.5 scenario after 2100.

We have seen from ECHAM6 time-slice simulations that the impact of both the simulated climate states and the applied model configurations on stratosphere-troposphere coupling during extreme stratospheric events is small. Neither in the number of extreme events nor in the ratio of downward to non-downward propagating events, significant changes among the ECHAM6 time slices were obtained. However, in the transient simulations with MPI-ESM, where the characteristics of SSW events turned out to be more realistically represented, compared to the ECHAM6 stand-alone atmospheric

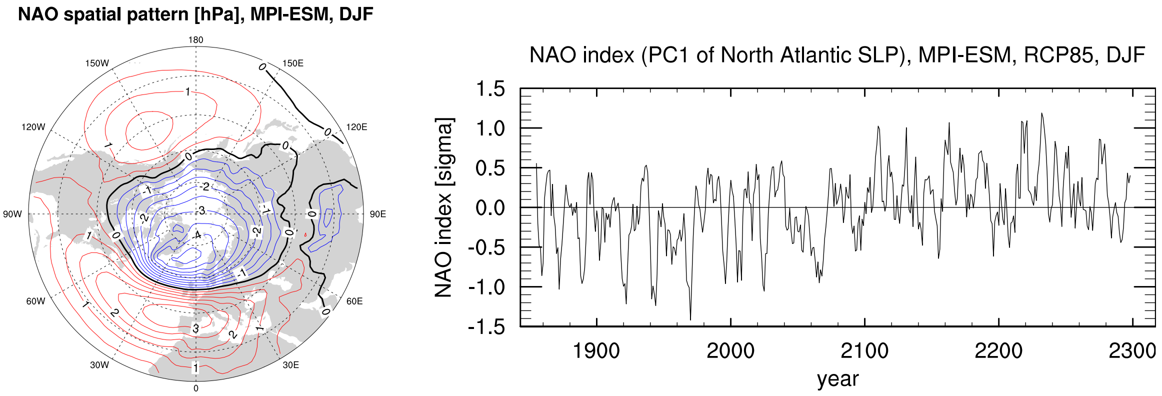

Figure 6.17: The NAO spatial pattern (left) is depicted together with the associated NAO index (right), as derived for the historical simulation extended with the extended ensemble member of the RCP8.5 scenario simulation. For the NAO index 5-year running-mean values are shown.

GCM, a robust response to a changing climate is obtained for the second half of the 21st century. In both the RCP4.5 and the RCP8.5 scenario, an increase in SSW events of roughly 50% compared to the preindustrial climate state is simulated. After 2100, in turn, the RCP8.5 scenario exhibits a reduction in SSW events of about 50% compared to the second half of the 21st century, accompanied with a shift in the SSW monthly distribution to the late winter. This change in stratospheric dynamics coincides with a substantial shift in the sea-level pressure field over the North Atlantic. Thus, a future change in the troposphere-surface system may be induced by a change in stratospheric dynamics.

Chapter 7

Conclusions and outlook

7.1 Conclusions

The stratosphere-troposphere dynamical coupling is investigated in this study with the stand-alone atmospheric GCM ECHAM6 and the coupled atmosphere-ocean-land Earth System Model MPI-ESM. Sensitivity simulations performed with ECHAM6 indicate that both the model configuration, in terms of the representation of the stratosphere in a GCM, as well as the simulated climate state yield a significant impact on the stratospheric meridional overturning circulation, the Brewer-Dobson Circulation (BDC). A consistent strengthening of the BDC from the preindustrial to the future climate state is obtained for all ECHAM6 model configurations. This corroborates the results of the vast majority of state-of-the-art climate models. However, the systematical investigation of the impact of the model configuration on the driving of the BDC in a changing climate (see also Bunzel and Schmidt, 2013) indicates that similar BDC trends originate from different causes depending on the vertical extent of the model. While in the high-top model the parameterised wave drag yields the primary contribution to the simulated BDC trend, in the low-top model resolved waves yield the most prominent contribution to the trend. This result may help explain the findings of Butchart et al. (2010), who found a large spread in both amplitude and origin of the BDC trend simulated by different models.

The obtained impact of the model configuration on the origin and magnitude of the BDC change in a GHG-induced changing climate, can also be considered to be important with regard to the discrepancy between model and observational datasets in terms of the BDC trend (Engel et al., 2009). While climate models simulate a robust BDC increase over the last decades, observational datasets do not show any significant trend in BDC strength. In order to study both the significance and origin of this discrepancy the natural BDC variability is for the first time assessed from multi-centennial simulations with MPI-ESM. A comparison of the obtained natural BDC variability to BDC trends derived from observational datasets and transient MPI-ESM simulations covering the last decades, implies that at least 30 years of data with good temporal and spatial coverage on a global scale are necessary to significantly distinguish BDC trends from natural BDC variability in the second half of the 20th century. The natural

BDC variability is found to be produced, at least partly, by SST anomalies in the central Pacific, as decadal-scale modes of variability turn out to be transmitted from the troposphere-surface system to the lower stratosphere. The transmission of these low-frequency modes of variability, however, is substantially influenced by the MPI-ESM model configuration. In the MR configuration, the enhanced resolution in both the oceanic and the atmospheric component of MPI-ESM alters the low-frequency modes of variability and, thus, diminishes the communication of decadal-scale anomalies from the troposphere-surface system to the lower stratosphere.

The behaviour of stratospheric dynamics and stratosphere-troposphere coupling mechanisms is for the first time evaluated in this study for the remote future simulated in the extended RCP8.5 scenario with MPI-ESM. The transient RCP8.5 scenario simulation indicates a highly non-linear behaviour with a prominent transition after 2100. In the second half of the 20th century, the modification of the wave propagation conditions due to the change in the zonal-mean zonal wind field causes an increase in extreme weak stratospheric polar vortex events, accompanied with sudden stratospheric warmings (SSWs). After 2100 the ongoing increase in zonal-mean zonal winds, however, causes a relatively rapid decrease in SSW events. This decrease is accompanied with a prominent transition in the troposphere-surface system, reflected in a shift of the North Atlantic Oscillation (NAO) to more positive phases. This may imply that a future change in stratospheric dynamics significantly affects the weather and climate in central and northern Europe and Eurasia. The positive shift in the NAO index would imply stronger westerlies over the North Atlantic accompanied with enhanced transport of warm and moist air towards Europe. Eventually, the implication of the obtained change in stratospheric dynamics in the RCP8.5 scenario would cause more mild winters in central and northern Europe and Eurasia after 2100.

A more detailed summary of the results and conclusions obtained from the different chapters of this thesis, is given in the following.

7.1.1 The BDC: Impact of the model configuration

The impact of the model configuration on the behaviour of the mechanisms that drive the BDC is investigated by analysing model simulations performed with the state-of-the-art GCM ECHAM6, using different model setups in terms of the representation of the stratosphere. The results of these 50-year sensitivity simulations for different climate states have shown several similarities in the appearance of the BDC among the applied configurations of the model. The BDC pattern is qualitatively similar, independent of vertical resolution and vertical extent of the model. Even the relative contribution of resolved and unresolved waves to the driving of the total upward mass flux from the troposphere to the stratosphere is comparable. However, the 70 hPa upward mass flux is found to be lower by roughly 25% in the L31 configuration than in the high-top configurations of the model. When the air is close to the lid of the L31 model, an artificial force causes an additional acceleration, making the BDC in the mid- and high-latitudes appear as strong as in the high-top configurations of the model. In fact, here values of the mean age of air in the L31 model lie between those of the two high-top model configurations. The artificial force acting in the L31 model originates from the horizontal diffusion scheme, which was modified in order to damp the momentum carried by the resolved waves into the upper model layers to avoid wave reflection at the model lid. The reduced EPFD contribution to the driving of the upward mass flux in the lower stratosphere, together with a second-order contribution of the missing NGWD in the L31 configuration, cause the slower tropical upwelling in the low-top configuration of ECHAM6. Considering the total upward mass flux as derived from ERA-Interim reanalysis data, however, the L31 configuration simulates the most realistic upward mass flux at 70 hPa.

Increasing the vertical resolution in the high-top model, in turn, results in a slightly slower BDC. The total upward mass flux at 70 hPa is reduced by roughly 5%, and the mean age of stratospheric air increases by about 20% in the mid-latitudes. It turns out that the origin of this difference in age of air among the two high-top model setups is primarily due to the reduced numerical diffusion through the tropopause in the L95 model configuration. By inducing the Secondary Meridional Circulation (Plumb and Bell, 1982) the internally generated QBO in the L95 model may be another source for the difference in the BDC pattern among the two high-top model configurations.

In order to examine the prominent discrepancy between model results and observational data in terms of the BDC trend in a changing climate, we have first evaluated the BDC change between the different climate states, as simulated with the different ECHAM6 model setups. All configurations of the model have shown a qualitatively similar BDC change between the different time slices. The weakest increase in strength of the subtropical jets is simulated in the L31 configuration of ECHAM6, coinciding with the weakest response in the 70 hPa upward mass flux in this model setup. Nevertheless, we have found a significant increase in tropical upwelling through the tropopause in all model configurations. It is important to emphasise here, however, that BDC changes obtained from different time-slice simulations, each performed under stationary boundary conditions, can not necessarily be considered to be directly comparable to trends derived from transient climate simulations or observational time series.

Nevertheless, the picture of a BDC strengthening is qualitatively confirmed for all applied configurations of the ECHAM6 GCM. This result is consistent with the findings of Karpechko and Manzini (2012), who analysed the BDC change from the present-day climate to a climate under doubled CO_2 concentrations as simulated with the ECHAM5 GCM in low-top and high-top model configurations. The behaviour of the BDC driving mechanisms in a changing climate indicates a prominent difference among the applied ECHAM6 model configurations. In both ECHAM6 L47 and L95 model setups the increase in 70 hPa DJF upward mass flux is dominated by an increase in the parameterised wave drag contribution. Although the upward mass flux was found to be largest in the L47 model, the highest increase in upward mass flux is simulated in the L95 version of the model. The parameterised wave drag causes a slightly larger increase in the upward mass flux in this model version than in the L47 configuration. In the L31 model, however, the change is generally smaller by roughly 30% compared to the L95 configuration, and is dominated by an increase in the contribution of the resolved wave drag. Thus, we conclude that although the origin of the change in tropical upwelling varies with the vertical extent of the model, the ECHAM6 low-top model simulates a qualitatively similar BDC response as the two high-top configurations.

The reason for the dependence of the wave drag contribution on the vertical model extent is likely to be related to the treatment of the wave momentum flux at the model lid. Shaw and Shepherd (2007) found that the conservation of angular momentum by depositing the gravity wave momentum flux in the upper model levels has a significant impact on the downwelling induced by gravity wave drag. Depositing the orographic gravity wave momentum flux in the upper levels of the ECHAM6 GCM could therefore yield significant implications for the wave drag contribution to the tropical upwelling in the low-top configuration.

An evaluation of the vertical profile of the zonal-mean change in DJF tropical upwelling implies an increase from the preindustrial to the future climate state in the entire lower-to-middle stratosphere. In all model configurations the change in the lowermost stratosphere is mainly produced by resolved wave drag. However, the resolved wave drag contribution decreases with height, and at a certain pressure level the contribution of orographic gravity waves exceeds the resolved wave contribution. It turns out that the level, where this excess occurs, crucially depends on the vertical extent of the model. While in the high-top model the orographic gravity wave contribution exceeds the contribution of resolved waves already below 70 hPa, the level of the excess is shifted upward above the 70 hPa level in the L31 model. This result may help explain the findings of Butchart et al. (2010), who analysed many different CCMs with regard to the wave type contribution to the 70 hPa upward mass flux and its trend. They found different origins of the derived mass flux trend among models with different configurations regarding vertical extent and resolution. If we consider now that the primary origin of the change in upward mass flux varies even in simulations performed with the same GCM with different vertical extents, one may conclude that the spread in the results obtained from the CCMs used in Butchart et al. (2010) are, at least partly, due to the different configurations of the CCMs.

7.1.2 BDC trend versus natural BDC variability

The discrepancy between model results and observational data in terms of the BDC trend is further examined in this study by assessing the natural BDC variability from the multi-centennial preindustrial control simulation performed with MPI-ESM in the context of CMIP5. The BDC strength showed substantial variability for periods between 3 and 20 years. In order to evaluate the importance of this natural BDC variability with regard to the discrepancy between model and observational data in terms of the BDC trend, decadal-scale trends in the 70 hPa upward mass flux were first derived from the last decades of the CMIP5 historical simulation. The historical simulation covers the period from 1850 to 2005, and the 3-sigma significance threshold of the preindustrial control simulation is first exceeded in the second half of the 20th century. We have compared decadal-scale 70 hPa upward mass flux trends, derived from the last decades of the historical simulation, with trends derived from arbitrary periods of the same length in the preindustrial control simulation. This comparison showed that in MPI-ESM in the second half of the 20th century a simulation period of at least 30 years is necessary to significantly distinguish a trend in BDC strength from the natural BDC variability. Considering now that model simulations usually provide much better spatial resolution and temporal coverage than observational datasets, it may not be surprising that no significant BDC trend is obtained from age-of-air observations covering the last 30 years (Engel et al., 2009). Thus, it can not be excluded that the observed BDC trend is significantly influenced by natural BDC variability.

Besides the magnitude of the different modes of the natural BDC variability, we have also evaluated the origin of the natural BDC variability. The multi-centennial preindustrial control simulation, performed with MPI-ESM in different model configurations, indicates that also low-frequency modes of variability are transported from the troposphere-surface system to the stratosphere. MPI-ESM model simulations show significant coherence between the variability modes of the 70 hPa upward mass flux and the central Pacific SST anomalies (NINO 3.4 index) at periods between 3 and 20 years, with the signal in the NINO3.4 index leading the upward mass flux. This indicates that long-term modes of tropical SST variability are communicated to the lower stratosphere and are there visible in the strength of the tropical upward mass flux at 70 hPa. In the MR configuration of MPI-ESM, the enhanced resolution in both the oceanic and atmospheric component of MPI-ESM alters the low-frequency modes of variability and, thus, diminishes the communication of decadal-scale anomalies from the troposphere-surface system to the lower stratosphere.

7.1.3 Stratosphere-troposphere coupling in a changing climate

Eventually, the behaviour of dynamical stratosphere-troposphere coupling processes in a changing climate is investigated in this study. Several other studies showed that the decadal variability in frequency of extreme stratospheric events as well as the variation of the timescales involved in stratosphere-troposphere coupling processes is large. This makes a potential change in these processes under a changing climate difficult to detect in transient model simulations or reanalysis datasets, which cover only a few decades. We have seen that this behaviour is also reflected by the ECHAM6 simulations of different stationary climate states in different model configurations. Neither the weak nor the strong polar vortex events indicate any systematic change among climate states or model configurations, and also the time lag between the stratospheric and tropospheric disturbances is not distinguishable among the time-slice simulations. A robust model result, however, is that in all time slices and model configurations more than 50% of the extreme stratospheric events are followed by a significant dynamical tropospheric disturbance at 700 hPa during the 60 days after the occurrence of a stratospheric event. This behaviour compares well with ERA-40 reanalysis data (Runde, 2012). Generally, the downward propagation of NAM anomalies is most realistically simulated in the L95 model configuration of ECHAM6, when compared to the respective anomalies inferred from ERA-40 data (Baldwin and Thompson, 2009). In the L47 configuration, the fraction of the original stratospheric anomaly that reaches the troposphere-surface system is substantially smaller compared to ERA-40 data. In both ERA-40 data and in the L95 configuration the actual stratospheric event is preceded by an anomaly of the opposite sign. This preceding anomaly is not simulated in the L31 configuration.

The extreme case of a weak stratospheric polar vortex event, a sudden stratospheric warming (SSW), is considered to be a main feature of stratosphere-troposphere coupling. Thus, in order to study the interaction of the stratosphere and troposphere in a changing climate on the basis of model simulations, we have first evaluated the ability of the underlying models to simulate SSW events realistically. An SSW detection and classification algorithm was developed to analyse the simulation of SSWs in ECHAM6 and MPI-ESM. The obtained model results are compared to reanalysis datasets in terms of SSW frequency, monthly distribution, and ratio between vortex splitting and displacement events. It turned out that the ECHAM6 model reproduces the observed SSW characteristics equally well in L47 and L95 model configurations. The positive bias in SSW frequency simulated in the L95 configuration is larger, however, the ratio between vortex splits and displacements is simulated more realistically compared to the L47 model configuration. An even better representation of, particularly, the SSW frequency is obtained for MPI-ESM, in which ECHAM6 is used as the atmospheric component of a coupled Earth System Model. The multi-centennial MPI-ESM preindustrial control simulation indicates significant long-term variability in the SSW occurrence frequency at a period of around 50 years, which corroborates earlier results obtained by Schimanke et al. (2011) for another coupled atmosphere-ocean climate model.

In all ECHAM6 model configurations an increase in SSW frequency of up to 50% from the preindustrial to the future climate state is simulated. This increase is primarily due to an increase in SSW displacement events, which reflects an increased importance of the planetary wave number 1 in terms of the triggering of SSW events in a future climate. Also in MPI-ESM an increase in SSW frequency of roughly 50% is simulated from the preindustrial climate state (6.4 events/decade) to the second half of the 21st century in both the RCP4.5 (9.3 events/decade) and RCP8.5 scenario (9.8 events/decade). We have seen that the strengthening of the upper flanks of the subtropical jets, caused by a GHG-induced changing climate, allows for more waves to propagate from the troposphere to the stratosphere in the simulated future climate state. This mechanism, which is considered to be responsible for the simulated BDC strengthening, is likely to cause also the obtained increase in SSW frequency. In the real world the longest available observational datasets which allow for an SSW frequency analysis merely extend over 4 to 5 decades, and exhibit large decadal-scale variability. Thus, a significant change in SSW frequency can not be detected from state-of-the-art observational or reanalysis datasets.

In the remote future simulated in the RCP8.5 scenario after 2100, where a further increase of GHG concentrations is assumed, we have also seen a drop in SSW frequency by 50% compared to the second half of the 21st century. Thus, the SSW frequency in the RCP8.5 scenario after 2100 (5.1 events/decade) lies below the value obtained from the preindustrial control simulation. This drop in SSW frequency coincides with a shift in the SSW monthly distribution towards the late winter. An evaluation of the zonal-mean zonal winds under these extreme climate change conditions, showed that the strengthening of the upper flanks of the subtropical jets continues also after 2100 in the RCP8.5 scenario. Eventually, the affected region even extends to 60°N at 10 hPa, the region where the definition of SSW events refers to. This allows for more waves to propagate through this region and dissipate or break further above. Only in the very late winter, when the polar vortex becomes weaker, SSW events still occur frequently. As the final warming is on average shifted to May, one may even find SSW events in April or early May.

Although the relatively rapid change in SSW frequency after 2100 seems to be just a manifestation of a continuous and steady upward shift of the critical layers for wave dissipation, the change in SSW frequency is accompanied with a prominent transition in the troposphere-surface system. The index of the North Atlantic Oscillation (NAO) exhibits a remarkable shift to more positive NAO phases after 2100, which would imply more mild winters in central and northern Europe and Eurasia. Several other studies showed that the stratospheric disturbance after extreme weak stratospheric vortex events propagates downward, and often induces a negative shift in the NAO index. Thus, a connection between the drop in SSW frequency around 2100 and the coinciding positive shift in the NAO index can be considered to be likely. Taking into account the results of other studies in terms of the connection between extreme stratospheric events and the NAO, it also appears to be likely that the change in the NAO index is induced by the change in SSW frequency. Whether this also holds for the remote future climate state simulated with MPI-ESM for the RCP8.5 scenario, however, is so far not entirely clear.

7.2 Outlook

The results of this study show that the discrepancy between state-of-the-art model simulations and observational datasets in terms of the BDC trend, derived for the last decades, may entirely be due to natural BDC variability. However, many challenges with regard to the realistic simulation of the BDC in state-of-the-art climate model remain. A substantial offset in terms of the age of stratospheric air between model and observational data exists, which implies that the simulated BDC strength, as assessed from age-of-air tracers, indicates a substantial positive bias compared to observational age-of-air time series. As we identified reduced numerical diffusion through the tropopause already in the L95 model as the main origin of the older age of air compared to the L47 configuration, an even higher vertical model resolution might lead to a further reduction of the offset between model and observational data. This hypothesis is corroborated by the ascent rates of air in the tropical lower stratosphere derived from the water vapour tape recorder. We have seen that increasing the vertical model resolution decreases the positive bias in the simulated upward transport of water vapour, and only in the L95 model configuration the stratospheric water vapour transport velocities can be considered to be relatively realistic. In order to further investigate the dependence of the tracer transport on the vertical model resolution, the design of further sensitivity studies would be required.

In terms of the behaviour of stratosphere-troposphere dynamical coupling in a changing climate, the results of this thesis suggest that a highly non-linear response may occur in the future climate system, as simulated in the RCP8.5 scenario for the end of the 21st century. While the continuous upward shift of the critical layers for wave dissipation is accompanied with an increase in SSW events in the second half of the 21st century, a relatively rapid drop in SSW frequency occurs after 2100. Almost simultaneously the troposphere-surface system undergoes a prominent transition, which is reflected in a shift towards more positive NAO phases. The future change in stratospheric dynamics, as simulated in the RCP8.5 scenario after 2100, may cause this shift in the NAO index and, thus, may eventually lead to more mild winters over central and northern Europe and Eurasia in a future climate. However, resolving the entire cause-and-effect relationship involved in the transmission of dynamical disturbances between the stratosphere and the troposphere, would require additional sensitivity simulations.

Appendix

I. Validity and accuracy of the TEM framework

As the derivation of the primitive equations and the subsequent application of the TEM framework introduces many assumptions to the equations of motion, the validity and accuracy of the TEM framework is investigated here for an altitude range extending from the surface far into the thermosphere. For this purpose a HAMMONIA model output dataset is used, which extends over one month and is derived from an experiment, which was run under January atmospheric conditions. The HAMMONIA model (Schmidt et al., 2006) is a chemistry-climate model (CCM) with a model domain extending up to an altitude of roughly 250 km ($\approx 1.7 \cdot 10^{-7}$ hPa). In the dataset analysed here the output frequency is 10 minutes, so that output was written at every model time step. Thus, this dataset is suited to check the validity of the approximations involved in the TEM framework (see Section 3.1) in a large vertical domain, and test the impact of the model output frequency on the derived TEM quantities.

In terms of the validity of the TEM framework it turns out that the static stability of the atmosphere is a crucial quantity. It is represented here by the zonal-mean vertical gradient of the potential temperature, $\partial\overline{\Theta}/\partial z$ or $\partial\overline{\Theta}/\partial p$, and appears in the denominator of almost all definitions involved in the TEM framework, e.g. the residual velocities $\overline{v}^*$ and $\overline{w}^*$ (see Eqs. 3.22 and 3.23). In the zonal mean the atmospheric stratification is

$$\text{stable, if} \quad \frac{\partial\overline{\Theta}}{\partial p} < 0 \ , \tag{7.1}$$

$$\text{neutral, if} \quad \frac{\partial\overline{\Theta}}{\partial p} = 0 \ , \ \text{and} \tag{7.2}$$

$$\text{unstable, if} \quad \frac{\partial\overline{\Theta}}{\partial p} > 0 \ . \tag{7.3}$$

Applying the TEM framework to the 1-month test dataset shows that there are two regions, where the atmospheric stratification becomes unstable in the zonal mean at some time steps: the equatorial lowermost troposphere and the polar thermosphere.

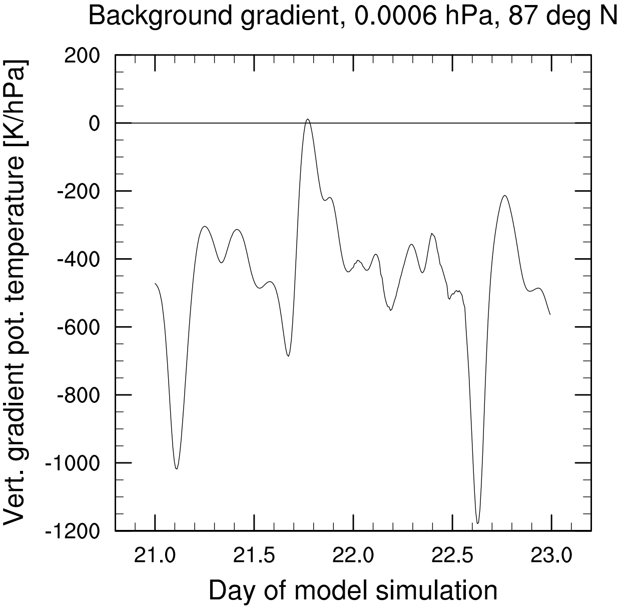

Figure 7.1: The vertical gradient of the zonal-mean potential temperature, $\partial\overline{\Theta}/\partial p$, is shown at 87°N at an altitude of $\approx$ 100km (0.0006 hPa). On day 21 of the model simulation (see text for description) the stratification of the atmosphere becomes unstable for a few model time steps.

An example for a situation of unstable atmospheric stratification in the zonal mean is shown in Figure 7.1. On day 21 of the model simulation the atmosphere becomes unstable for a few time steps in the polar thermosphere. The impact of the unstable stratification on the residual mean meridional velocity is depicted in Figure 7.2. The stratification term in the denominator of the TEM quantities causes a strong oscillation in the TEM quantities, when the stratification becomes unstable. This oscillation usually persists only for a few time steps, however, its amplitude is large enough to significantly alter the mean calculated over a certain time period. The impact of such an oscillation can be reduced if a mean-differences approach is used to calculate the derivative $\partial\overline{\Theta}/\partial p$ instead of a cubic-spline (used here) or a polynomial approximation. However, the most comprehensive method would probably be to mask the time steps, when the atmospheric stratification becomes neutral or unstable.

The impact of the model output frequency on the TEM quantities is assessed here by comparing the residual mean vertical velocity $\overline{w}^*$ computed from different versions of the test dataset, each of which representing a different temporal resolution. While Figure 7.3 shows the monthly mean of $\overline{w}^*$ calculated for 6-hour model output frequency, in Figure 7.4 the monthly mean computed for the full temporal resolution (10 minutes) is depicted. The impact of the temporal data resolution on the derived TEM quantity does not seem to be large in the entire middle atmosphere, however, in the thermosphere a high temporal data resolution leads to a much smoother structure. It appears that the variability on short timescales is much larger in the thermosphere compared to the lower and middle atmosphere. Additionally, the probability to resolve time steps of unstable atmospheric stratification increases with the temporal resolution of the dataset, which can significantly alter the mean value in the polar thermosphere

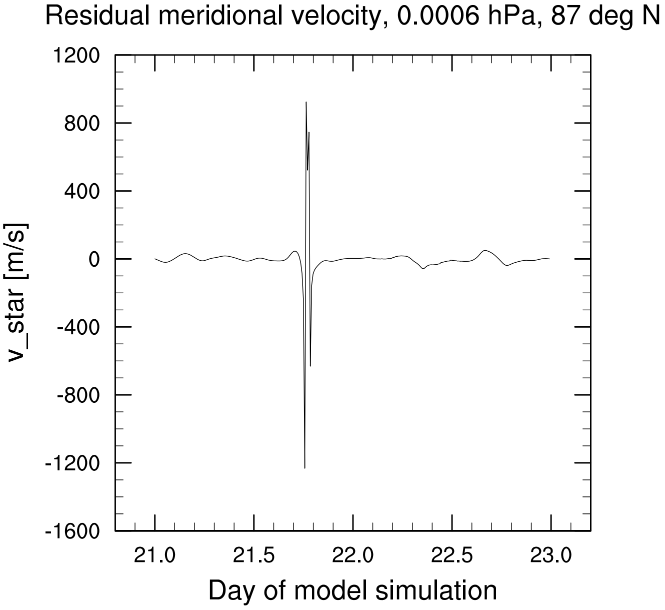

Figure 7.2: The residual mean meridional velocity $\overline{v}^*$ is presented at 87°N at an altitude of $\approx$ 100km (0.0006 hPa). The unstable stratification of the atmosphere on day 21 of the model simulation (see Fig. 7.1) causes a fluctuation in the residual mean meridional velocity (see Eq. 3.22).

and equatorial lowermost troposphere (see above). Other temporal data resolutions, ranging from 10-minute to daily model output, were also tested. It turned out that 6-hourly model output is the minimum temporal resolution necessary to reproduce the data fields of the TEM quantities computed from the full temporal resolution (10 minutes) comprehensively. Applying daily averaging on the 6-hourly model output before calculating the TEM quantities usually yields a comparable result for the stratosphere.

In summary, the investigation of the validity and accuracy of the TEM framework showed that the assumptions involved in the derivation of the TEM equations hold in the entire middle atmosphere and, to a large extent, also in the troposphere. It is merely the lowermost equatorial troposphere as well as the polar thermosphere, where unstable atmospheric stratification cancels the validity of the TEM quantities. Additionally, in the entire thermosphere large variability on short timescales leads to a strong dependence of the TEM quantities on the temporal resolution of the original model data.

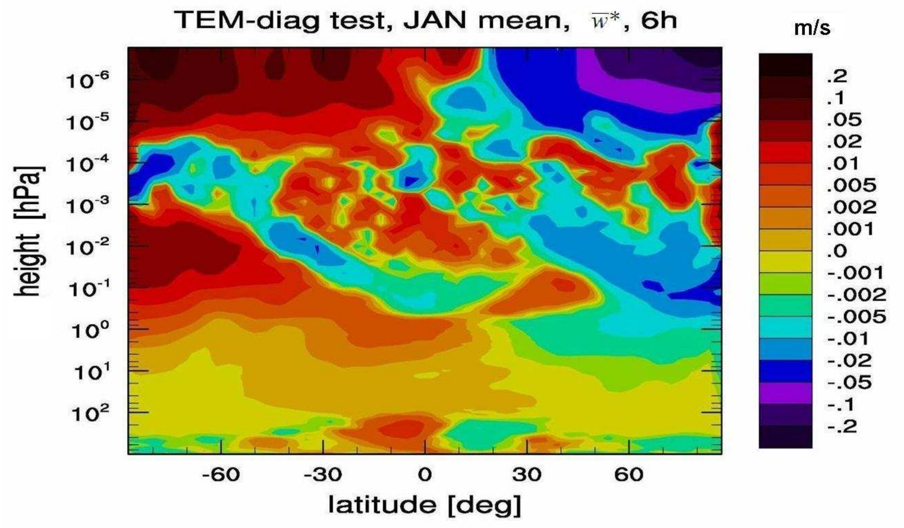

Figure 7.3: The January-mean of the residual mean vertical velocity $\overline{w}^*$ is shown for the full domain of the HAMMONIA model. The values of $\overline{w}^*$ in this plot were computed via the TEM framework applied on model data with output every 6 hours.

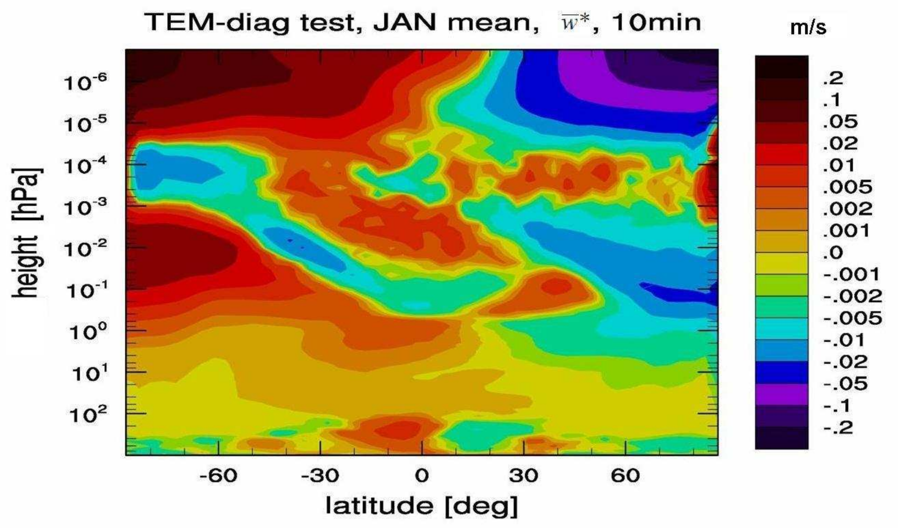

Figure 7.4: The January-mean of the residual mean vertical velocity $\overline{w}^*$ is shown for the full domain of the HAMMONIA model. The values of $\overline{w}^*$ in this plot were computed via the TEM framework applied on model data with output at every time step (every 10 minutes).

II. A classification algorithm for sudden stratospheric warmings

We classify a sudden stratospheric warming (SSW) event (see Section 3.5.1) as a vortex split or a vortex displacement, depending on the geometry of the geopotential height field from 5 days before until 10 days after the central date of the event. Other studies also distinguished between these two types of SSW events by e.g. the geometry of the absolute vorticity field during SSW events Charlton and Polvani (2007) or the amplitude of large-scale wave numbers during the onset of SSW events Bancalá et al. (2012). The algorithm compiled within this study is described in the following. A similar version of this algorithm is used in Miller et al. (2013).

First, the input dataset consisting of daily-mean values is interpolated to the T31 horizontal resolution. Then the following steps are applied to every day from 5 days before until 10 days after the central date of an SSW event.

The absolute minimum of the geopotential height at 10 hPa, $\Phi_{10}(\lambda, \phi)$, is determined and assumed to represent the center of the main polar vortex:

$$\Phi_{10,center} = min \left\{ \Phi_{10}(\lambda, \phi) \right\} \tag{7.4}$$

In a second step, we identify the local minima $\Phi_{10,local,i}$ on every latitude in the model grid from the North Pole to 20°N.

The decision if a particular SSW is categorised as a split or a displacement is determined by searching for paths from the location of $\Phi_{10,center}$ to the locations of all $\Phi_{10,local,i}$'s in the latitude-longitude model grid (λ, ϕ) along positive geopotential height gradients. If our algorithm finds such a path for every local minimum, we refer to the event as a displacement. Otherwise, it is called a split.

Additionally, we introduce two adjustable parameters to the routine. The first parameter reduces the number of $\Phi_{10,local,i}$'s to make sure that only significant minima are considered. If

$$\begin{gathered} (\Phi_{10,mean} - \Phi_{10,local,i}) < 0.3 \cdot (\Phi_{10,mean} - \Phi_{10,center}), \\ \text{where} \quad \Phi_{10,mean} = \overline{\Phi_{10}(\lambda, \phi)} \; for \; 20^\circ \leq \phi \leq 90^\circ, \end{gathered} \tag{7.5}$$

the local minimum $\Phi_{10,local,i}$ is excluded from the computations.

A second parameter accounts for the finite resolution in model and reanalysis data. It allows for path steps p with slightly negative gradients. We set it to allow for

$$p > -0.03 \cdot (\Phi_{10,mean} - \Phi_{10,center}). \tag{7.6}$$

These parameter settings are arbitrary but are experimentally determined for the T31 horizontal grid according to our subjective impressions. For ERA40 data interpolated to T31, the classification routine produces similar results as the one presented by Charlton and Polvani (2007).

List of Figures

List of Tables

Bibliography

Andrews, D. G., J. R. Holton, and C. B. Leovy, 1987: *Middle atmosphere dynamics.* Academic Press.

Aßmann, R. A., 1902: Über die Existenz eines wärmeren Luftstromes in der Höhe von 10 bis 15 km. *Sitzungsber. K. Preuss. Akad. Wiss.*, **24**, 495–504.

Austin, J. and F. Li, 2006: On the relationship between the strength of the Brewer-Dobson circulation and the age of stratospheric air. *Geophys. Res. Lett.*, **33**, D17 807.

Ayarzagüena, B., U. Langematz, and E. Serrano, 2011: Tropospheric forcing of the stratosphere: A comparative study of the two different major stratospheric warmings in 2009 and 2010. *J. Geophys. Res.*, **116**, D18114, doi:10.1029/2010JD015023.

Baldwin, M. P. and T. J. Dunkerton, 1999: Propagation of the Arctic Oscillation from the stratosphere to the troposphere. *J. Geophys. Res.*, **104**, 30 937–30 946, doi:10.1029/1999JD900445.

Baldwin, M. P. and T. J. Dunkerton, 2001: Stratospheric Harbingers of Anomalous Weather Regimes. *Science*, **294**, 581–584, doi:10.1126/science.1063315.

Baldwin, M. P. and D. W. J. Thompson, 2009: A critical comparison of stratosphere-troposphere coupling indices. *Q. J. R. Meteorol. Soc.*, **135**, 1661–1672, doi:10.1002/qj.479.

Bancalá, S., K. Krüger, and M. Giorgetta, 2012: The preconditioning of major sudden stratospheric warmings. *J. Geophys. Res.*, **117**, D04101, doi:10.1029/2011JD016769.

Birner, T. and H. Bönisch, 2011: Residual circulation trajectories and transit times into the extratropical lowermost stratosphere. *Atmos. Chem. Phys.*, **11**, 817–827.

Black, D. E., L. C. Peterson, J. T. Overpeck, A. Kaplan, M. N. Evans, and M. Kashgarian, 1999: Eight Centuries of North Atlantic Ocean Atmosphere Variability. *Science*, **286**, 1709–1713.

Black, E., M. Blackburn, G. Harrison, B. Hoskins, and J. Methven, 2004: Factors contributing to the summer 2003 European heatwave. *Weather*, **59**, 217–223, doi:10.1256/wea.74.04.

Bönisch, H., A. Engel, T. Birner, P. Hoor, D. W. Tarasick, and E. A. Ray, 2011: On the structural changes in the Brewer-Dobson circulation after 2000. *Atmos. Chem. Phys.*, **11**, 3937–3948, doi:10.5194/acp-11-3937-2011.

Brasseur, G. P. and S. Solomon, 2005: *Aeronomy of the Middle Atmosphere: Chemistry and Physics of the Stratosphere and Mesosphere.* Springer.

Brewer, A. W., 1949: Evidence for a world circulation provided by the measurements of helium and water vapour distribution in the stratosphere. *Q. J. R. Meteorol. Soc.*, **75**, 351–363.

Brovkin, V., L. Boysen, T. Raddatz, V. Gayler, A. Loew, and M. Claussen, 2013: Evaluation of vegetation cover and land-surface albedo in MPI-ESM CMIP5 simulations. *J. Adv. Model. Earth Syst.*

Bunzel, F. and H. Schmidt, 2013: The Brewer-Dobson Circulation in a changing climate: Impact of the model configuration. *J. Atmos. Sci.*, in press.

Butchart, N., J. Austin, J. R. Knight, A. A. Scaife, and M. L. Gallani, 2000: The Response of the Stratospheric Climate to Projected Changes in the Concentrations of Well-Mixed Greenhouse Gases from 1992 to 2051. *J. Climate*, **13**, 2142–2159, doi:10.1175/1520-0442(2000)013⟨2142:TROTSC⟩2.0.CO;2.

Butchart, N. and A. Scaife, 2001: Removal of chlorofluorocarbons by increased mass exchange between the stratosphere and troposphere in a changing climate. *Nature*, **410**, 799–802.

Butchart, N., et al., 2006: Simulations of anthropogenic change in the strength of the Brewer-Dobson circulation. *Climate Dyn.*, **27**, 727–741.

Butchart, N., et al., 2010: Chemistry-Climate Model Simulations of Twenty-First Century Stratospheric Climate and Circulation Changes. *J. Climate*, **23**, 5349–5374.

Butchart, N., et al., 2011: Multimodel climate and variability of the stratosphere. *J. Geophys. Res.*, **116**, D05102, doi:10.1029/2010JD014995.

Charlton, A. J. and L. M. Polvani, 2007: A New Look at Stratospheric Sudden Warmings. Part I: Climatology and Modeling Benchmarks. *J. Climate*, **20**, 449, doi:10.1175/JCLI3996.1.

Charlton, A. J., et al., 2007: A New Look at Stratospheric Sudden Warmings. Part II: Evaluation of Numerical Model Simulations. *J. Climate*, **20**, 470, doi:10.1175/JCLI3994.1.

Charney, J. G. and P. G. Drazin, 1961: Propagation of planetary-scale disturbances from the lower into the upper atmosphere. *J. Geophys. Res.*, **66**, 83–109, doi:10.1029/JZ066i001p00083.

Cook, P. A. and H. K. Roscoe, 2009: Variability and trends in stratospheric NO_2 in Antarctic summer, and implications for stratospheric NO_y. *Atmos. Chem. Phys.*, **9**, 3601–3612.

Courant, R., K. Friedrichs, and H. Lewy, 1928: Über die partiellen Differenzengleichungen der mathematischen Physik. *Mathematische Annalen*, **100**, 32–74, doi:10.1007/BF01448839.

Croci-Maspoli, M. and H. C. Davies, 2009: Key Dynamical Features of the 2005/06 European Winter. *Mon. Wea. Rev.*, **137**, 664, doi:10.1175/2008MWR2533.1.

Dameris, M., et al., 2005: Long-term changes and variability in a transient simulation with a chemistry-climate model employing realistic forcing. *Atmos. Chem. Phys.*, **5**, 2297–2353.

Deckert, R. and M. Dameris, 2008: Higher tropical SSTs strengthen the tropical upwelling via deep convection. *Geophys. Res. Lett.*, **35**, L10813, doi:10.1029/2008GL033719.

Diallo, M., B. Legras, and A. Chedin, 2012: Age of stratospheric air in the ERA-Interim. *Atmos. Chem. Phys.*, **12**, 17 087–17 134, doi:10.5194/acpd-12-17087-2012.

Dobson, G. M. B., 1952: Ozone in the Earth's atmosphere. *Endeavour*, **11**, 215–219.

Edmon, H. J., Jr., B. J. Hoskins, and M. E. McIntyre, 1980: Eliassen-Palm Cross Sections for the Troposphere. *J. Atmos. Sci.*, **37**, 2600–2616, doi:10.1175/1520-0469(1980)037⟨2600:EPCSFT⟩2.0.CO;2.

Eliassen, A. and E. Palm, 1961: On the transfer of energy in stationary mountain waves. *Geofysiske Publikasjoner*, **12**, 1–23.

Engel, A., et al., 2009: Age of stratospheric air unchanged within uncertainties over the past 30years. *Nat. Geosci.*, **2**, 28–31.

Etling, D., 2002: *Theoretische Meteorologie: Eine Einführung*. Springer Verlag.

Eyring, V., et al., 2005: A Strategy for Process-Oriented Validation of Coupled Chemistry Climate Models. *Bull. Amer. Meteor. Soc.*, **86**, 1117–1133, doi:10.1175/BAMS-86-8-1117.

Eyring, V., et al., 2008: Overview of the new ccmval reference and sensitivity simulations in support of upcoming ozone and climate assessments and the planned sparc ccmval report. *SPARC Newsl.*, **30**, 20–26.

Fischer, H. and B. Mieding, 2005: A 1,000-year ice core record of interannual to multidecadal variations in atmospheric circulation over the North Atlantic. *Climate Dyn.*, **25**, 65–74, doi:10.1007/s00382-005-0011-x.

Garcia, R. R. and W. J. Randel, 2008: Acceleration of the Brewer-Dobson Circulation due to Increases in Greenhouse Gases. *J. Atmos. Sci.*, **65**, 2731–2739.

Garcia, R. R., W. J. Randel, and D. E. Kinnison, 2011: On the Determination of Age of Air Trends from Atmospheric Trace Species. *J. Atmos. Sci.*, **68**, 139–154, doi:10.1175/2010JAS3527.1.

García-Herrera, R., N. Calvo, R. R. Garcia, and M. A. Giorgetta, 2006: Propagation of ENSO temperature signals into the middle atmosphere: A comparison of two general circulation models and ERA-40 reanalysis data. *J. Geophys. Res.*, **111**, D06101, doi:10.1029/2005JD006061.

Garny, H., M. Dameris, W. Randel, G. E. Bodeker, and R. Deckert, 2011: Dynamically Forced Increase of Tropical Upwelling in the Lower Stratosphere. *J. Atmos. Sci.*, **68**, 1214–1233.

Garny, H., M. Dameris, and A. Stenke, 2009: Impact of prescribed SSTs on climatologies and long-term trends in CCM simulations. *Atmos. Chem. Phys.*, **9**, 6017–6031.

Gerber, E. P. and L. M. Polvani, 2009: Stratosphere-Troposphere Coupling in a Relatively Simple AGCM: The Importance of Stratospheric Variability. *J. Climate*, **22**, 1920, doi:10.1175/2008JCLI2548.1.

Giorgetta, M., et al., 2012: Climate change from 1850 to 2100 in mpi-esm simulations for the coupled model intercomparison project 5. *J. Adv. Model. Earth Syst.*, submitted.

Giorgetta, M. A., E. Manzini, E. Roeckner, M. Esch, and L. Bengtsson, 2006: Climatology and Forcing of the Quasi-Biennial Oscillation in the MAECHAM5 Model. *J. Climate*, **19**, 3882, doi:10.1175/JCLI3830.1.

Hall, T. M. and R. A. Plumb, 1994: Age as a diagnostic of stratospheric transport. *J. Geophys. Res.*, **99**, 1059–1070.

Harada, Y., A. Goto, H. Hasegawa, N. Fujikawa, H. Naoe, and T. Hirooka, 2010: A Major Stratospheric Sudden Warming Event in January 2009. *J. Atmos. Sci.*, **67**, 2052–2069, doi:10.1175/2009JAS3320.1.

Haynes, P. H., M. E. McIntyre, T. G. Shepherd, C. J. Marks, and K. P. Shine, 1991: On the 'Downward Control' of Extratropical Diabatic Circulations by Eddy-Induced Mean Zonal Forces. *J. Atmos. Sci.*, **48**, 651–680.

Hegglin, M. I. and T. G. Shepherd, 2009: Large climate-induced changes in ultraviolet index and stratosphere-to-troposphere ozone flux. *Nat. Geosci.*, **2**, 687–691, doi:10.1038/ngeo604.

Hines, C. O., 1997: Doppler-spread parameterization of gravity-wave momentum deposition in the middle atmosphere. Part 1: Basic formulation. *J. Atmos. Sol.-Terr. Phys.*, **59**, 371–386.

Holton, J. R., 1983: The Influence of Gravity Wave Breaking on the General Circulation of the Middle Atmosphere. *J. Atmos. Sci.*, **40**, 2497–2507, doi:10.1175/1520-0469(1983)040⟨2497:TIOGWB⟩2.0.CO;2.

Holton, J. R., 1992: *An introduction to dynamic meteorology*. International geophysics series, Academic Press.

Holton, J. R., P. H. Haynes, M. E. McIntyre, A. R. Douglass, R. B. Rood, and L. Pfister, 1995: Stratosphere-troposphere exchange. *Rev. Geophys.*, **33**, 403–439, doi:10.1029/95RG02097.

Holton, J. R. and H.-C. Tan, 1980: The Influence of the Equatorial Quasi-Biennial Oscillation on the Global Circulation at 50 mb. *J. Atmos. Sci.*, **37**, 2200–2208, doi:10.1175/1520-0469(1980)037⟨2200:TIOTEQ⟩2.0.CO;2.

Hoskins, B. J. and P. D. Sardeshmukh, 1987: A diagnostic study of the dynamics of the northern hemisphere winter of 1985-86. *Q. J. R. Meteorol. Soc.*, **113**, 759–778, doi:10.1002/qj.49711347705.

Hurrell, J. W., Y. Kushnir, G. Ottersen, and M. Visbeck, 2003: *The North Atlantic Oscillation: Climatic Significance and Environmental Impact*. Geophys. Monogr. Ser., vol. 134, 279 pp., AGU, Washington, D. C., doi:{10.1029/GM134}.

Ilyina, T., K. D. Six, J. Segschneider, E. Maier-Reimer, H. Li, and I. Núñez-Riboni, 2013: The global ocean biogeochemistry model hamocc: Model architecture and performance as component of the mpi-earth system model in different cmip5 experimental realizations. *J. Adv. Model. Earth Syst.*

Jiang, X., S. J. Eichelberger, D. L. Hartmann, R. Shia, and Y. L. Yung, 2007: Influence of Doubled CO2 on Ozone via Changes in the Brewer Dobson Circulation. *J. Atmos. Sci.*, **64**, 2751.

Jung, T., F. Vitart, L. Ferranti, and J.-J. Morcrette, 2011: Origin and predictability of the extreme negative NAO winter of 2009/10. *Geophys. Res. Lett.*, **38**, L07701, doi:10.1029/2011GL046786.

Jungclaus, J. H., et al., 2006: Ocean Circulation and Tropical Variability in the Coupled Model ECHAM5/MPI-OM. *J. Climate*, **19**, 3952, doi:10.1175/JCLI3827.1.

Jungclaus, J. H., et al., 2013: Characteristics of the ocean simulations in mpiom, the ocean component of the mpi-earth system model. *J. Adv. Model. Earth Syst.*

Kalnay, E., et al., 1996: The NCEP/NCAR 40-Year Reanalysis Project. *Bull. Amer. Meteor. Soc.*, **77**, 437–472, doi:10.1175/1520-0477(1996)077⟨0437:TNYRP⟩2.0.CO;2.

Karpechko, A. and E. Manzini, 2012: Stratospheric influence on tropospheric climate change in the Northern Hemisphere. *J. Geophys. Res.*, **117**, D05 133, 14 pp.

Kirk-Davidoff, D. B., E. J. Hintsa, J. G. Anderson, and D. W. Keith, 1999: The effect of climate change on ozone depletion through changes in stratospheric water vapour. *Nature*, **402**, 399–401, doi:10.1038/46521.

Kodera, K. and Y. Kuroda, 2002: Dynamical response to the solar cycle. *J. Geophys. Res.*, **107**, 4749, doi:10.1029/2002JD002224.

Krismer, T. R., M. A. Giorgetta, and M. Esch, 2013: Seasonal Aspects of the Quasi-Biennial Oscillation. *J. Adv. Model. Earth Syst.*, in press.

Kushner, P. J., I. M. Held, and T. L. Delworth, 2001: Southern Hemisphere Atmospheric Circulation Response to Global Warming. *J. Climate*, **14**, 2238–2249, doi:10.1175/1520-0442(2001)014⟨0001:SHACRT⟩2.0.CO;2.

Labitzke, K. and H. van Loon, 1988: Associations between the 11-year solar cycle, the QBO and the atmosphere. I - The troposphere and stratosphere in the Northern Hemisphere in winter. *J. Atmos. Terr. Phys.*, **50**, 197–206.

Li, F., J. Austin, and J. Wilson, 2008: The Strength of the Brewer Dobson Circulation in a Changing Climate: Coupled Chemistry Climate Model Simulations. *J. Climate*, **21**, 40.

Limpasuvan, V., D. W. J. Thompson, and D. L. Hartmann, 2004: The Life Cycle of the Northern Hemisphere Sudden Stratospheric Warmings. *J. Climate*, **17**, 2584–2597, doi:10.1175/1520-0442(2004)017⟨2584:TLCOTN⟩2.0.CO;2.

Lott, F. and M. J. Miller, 1997: A new subgrid-scale orographic drag parametrization: Its formulation and testing. *Q. J. R. Meteorol. Soc.*, **123**, 101–127.

Lu, J., G. Chen, and D. M. W. Frierson, 2008: Response of the Zonal Mean Atmospheric Circulation to El Niño versus Global Warming. *J. Climate*, **21**, 5835, doi:10.1175/2008JCLI2200.1.

Mahfouf, J. F., D. Cariolle, J. F. Royer, J. F. Geleyn, and B. Timbal, 1994: Response of the Météo-France climate model to changes in CO_2 and sea surface temperature. *Climate Dyn.*, **9**, 345–362, doi:10.1007/BF00223447.

Manney, G. L., et al., 2011: Unprecedented Arctic ozone loss in 2011. *Nature*, **478**, 469–475, doi:10.1038/nature10556.

Manzini, E. and J. Feichter, 1999: Simulation of the SF_6 tracer with the middle atmosphere MAECHAM4 model: Aspects of the large-scale transport. *J. Geophys. Res.*, **104**, 31 097–31 108, doi:10.1029/1999JD900963.

Manzini, E., M. A. Giorgetta, M. Esch, L. Kornblueh, and E. Roeckner, 2006: The Influence of Sea Surface Temperatures on the Northern Winter Stratosphere: Ensemble Simulations with the MAECHAM5 Model. *J. Climate*, **19**, 3863–3881.

Manzini, E. and N. A. McFarlane, 1998: The effect of varying the source spectrum of a gravity wave parameterization in a middle atmosphere general circulation model. *J. Geophys. Res.*, **103**, 31 523–31 540, doi:10.1029/98JD02274.

Marsh, D. R. and R. R. Garcia, 2007: Attribution of decadal variability in lower-stratospheric tropical ozone. *Geophys. Res. Lett.*, **34**, L21807, doi:10.1029/2007GL030935.

Marsland, S., 2003: The Max-Planck-Institute global ocean/sea ice model with orthogonal curvilinear coordinates. *Ocean Modell.*, **5**, 91–127.

Matsuno, T., 1970: Vertical Propagation of Stationary Planetary Waves in the Winter Northern Hemisphere. *J. Atmos. Sci.*, **27**, 871–883, doi:10.1175/1520-0469(1970)027⟨0871:VPOSPW⟩2.0.CO;2.

Matsuno, T., 1971: A Dynamical Model of the Stratospheric Sudden Warming. *J. Atmos. Sci.*, **28**, 1479–1494, doi:10.1175/1520-0469(1971)028⟨1479:ADMOTS⟩2.0.CO;2.

Matthewman, N. J., J. G. Esler, A. J. Charlton-Perez, and L. M. Polvani, 2009: A New Look at Stratospheric Sudden Warmings. Part III: Polar Vortex Evolution and Vertical Structure. *J. Climate*, **22**, 1566, doi:10.1175/2008JCLI2365.1.

McLandress, C. and T. G. Shepherd, 2009: Simulated Anthropogenic Changes in the Brewer-Dobson Circulation, Including Its Extension to High Latitudes. *J. Climate*, **22**, 1516.

Meinshausen, M., et al., 2011: The rcp greenhouse gas concentrations and their extensions from 1765 to 2300. *Climatic Change*, **109 (1)**, 213–241.

Miller, A., H. Schmidt, and F. Bunzel, 2013: Vertical coupling of the middle atmosphere during stratospheric warming events. *J. Atmos. Sol.-Terr. Phys.*, in press.

Misios, S. and H. Schmidt, 2012: Mechanisms Involved in the Amplification of the 11-yr Solar Cycle Signal in the Tropical Pacific Ocean. *J. Climate*, **25**, 5102–5118, doi:10.1175/JCLI-D-11-00261.1.

Monge-Sanz, B. M., M. P. Chipperfield, D. P. Dee, A. J. Simmons, and S. M. Uppala, 2012: Improvements in the stratospheric transport achieved by a chemistry transport model with ECMWF (re)analyses: identifying effects and remaining challenges. *Q. J. R. Meteorol. Soc.*, doi:10.1002/qj.1996.

Mote, P. W., et al., 1996: An atmospheric tape recorder: The imprint of tropical tropopause temperatures on stratospheric water vapor. *J. Geophys. Res.*, **101**, 3989–4006, doi:10.1029/95JD03422.

Murgatroyd, R. J., 1971: Dynamical Modelling of the Stratosphere and Mesosphere. *Mesospheric Models and Related Experiments*, G. Fiocco, Ed., Astrophysics and Space Science Library, Vol. 25, 104.

Murgatroyd, R. J. and F. Singleton, 1961: Possible meridional circulations in the stratosphere and mesosphere. *Q. J. R. Meteorol. Soc.*, **87**, 125–135, doi:10.1002/qj.49708737202.

Nakicenovic, N. and R. Swart, 2000: *Special Report on Emissions Scenarios*. Cambridge University Press, New York, NY, 598 pp.

Neu, J., S. Strahan, P. Braesicke, A. Douglass, P. Huck, L. Oman, D. Pendlebury, and S. Tegtmeier, 2010: Sparc report on the evaluation of chemistry-climate models: Chapter 5: Transport. *SPARC CCMVal Report*.

Nishii, K., H. Nakamura, and T. Miyasaka, 2009: Modulations in the planetary wave field induced by upward-propagating Rossby wave packets prior to stratospheric sudden warming events: A case-study. *Q. J. R. Meteorol. Soc.*, **135**, 39–52, doi:10.1002/qj.359.

Okamoto, K., K. Sato, and H. Akiyoshi, 2011: A study on the formation and trend of the Brewer-Dobson circulation. *J. Geophys. Res.*, **116**, D10117.

Oltmans, S. J., H. Vömel, D. J. Hofmann, K. H. Rosenlof, and D. Kley, 2000: The increase in stratospheric water vapor from balloonborne, frostpoint hygrometer measurements at Washington, D.C., and Boulder, Colorado. *Geophys. Res. Lett.*, **27**, 3453–3456, doi:10.1029/2000GL012133.

Pawson, S., et al., 2000: The GCM-Reality Intercomparison Project for SPARC (GRIPS): Scientific Issues and Initial Results. *Bull. Amer. Meteor. Soc.*, **81**, 781–796, doi:10.1175/1520-0477(2000)081⟨0781:TGIPFS⟩2.3.CO;2.

Plumb, A. R. and R. C. Bell, 1982: A model of the quasi-biennial oscillation on an equatorial beta-plane. *Q. J. R. Meteorol. Soc.*, **108**, 335–352, doi:10.1002/qj.49710845604.

Plumb, R. A. and J. Eluszkiewicz, 1999: The Brewer-Dobson Circulation: Dynamics of the Tropical Upwelling. *J. Atmos. Sci.*, **56**, 868–890, doi:10.1175/1520-0469(1999)056⟨0868:TBDCDO⟩2.0.CO;2.

Polvani, L. M. and P. J. Kushner, 2002: Tropospheric response to stratospheric perturbations in a relatively simple general circulation model. *Geophys. Res. Lett.*, **29 (7)**, 1114, doi:10.1029/2001GL014284.

Quiroz, R. S., 1969: The Warming of the Upper Stratosphere in February 1966 and the Associated Structure of the Mesosphere. *Mon. Wea. Rev.*, **97**, 541, doi:10.1175/1520-0493(1969)097⟨0541:TWOTUS⟩2.3.CO;2.

Raddatz, T. J., et al., 2007: Will the tropical land biosphere dominate the climate-carbon cycle feedback during the twenty-first century? *Climate Dyn.*, **29**, 565–574, doi:10.1007/s00382-007-0247-8.

Ramaswamy, V., et al., 2001: *Radiative forcing of climate change*. Cambridge University Press, 349-416 pp.

Reichler, T., J. Kim, E. Manzini, and J. Kröger, 2012: A stratospheric connection to Atlantic climate variability. *Nat. Geosci.*, **5**, 783–787.

Reichler, T., P. J. Kushner, and L. M. Polvani, 2005: The Coupled Stratosphere-Troposphere Response to Impulsive Forcing from the Troposphere. *J. Atmos. Sci.*, **62**, 3337–3352, doi:10.1175/JAS3527.1.

Rind, D., D. Shindell, P. Lonergan, and N. K. Balachandran, 1998: Climate Change and the Middle Atmosphere. Part III: The Doubled CO_2 Climate Revisited. *J. Climate*, **11**, 876–894, doi:10.1175/1520-0442(1998)011⟨0876:CCATMA⟩2.0.CO;2.

Rind, D., R. Suozzo, N. K. Balachandran, and M. J. Prather, 1990: Climate Change and the Middle Atmosphere. Part I: The Doubled CO_2 Climate. *J. Atmos. Sci.*, **47**, 475–494.

Roeckner, E., et al., 2003: The atmospheric general circulation model ECHAM 5. PART I: Model description. *Max-Planck-Institut für Meteorologie Rep.*, **349**, 127 pp.

Roeckner, E., et al., 2006: Sensitivity of Simulated Climate to Horizontal and Vertical Resolution in the ECHAM5 Atmosphere Model. *J. Climate*, **19**, 3771–3791.

Rosenlof, K. H., 1995: Seasonal cycle of the residual mean meridional circulation in the stratosphere. *J. Geophys. Res.*, **100**, 5173–5192, doi:10.1029/94JD03122.

Rosenlof, K. H., et al., 2001: Stratospheric water vapor increases over the past half-century. *Geophys. Res. Lett.*, **28**, 1195–1198, doi:10.1029/2000GL012502.

Runde, T., 2012: Ursachen und wirkung der dynamischen kopplung von stratosphäre und troposphäre. *PhD thesis*, URL `http://nbn-resolving.de/urn:nbn:de:bvb:19-145456`.

Santer, B. D., et al., 2003: Contributions of Anthropogenic and Natural Forcing to Recent Tropopause Height Changes. *Science*, **301**, 479–483, doi:10.1126/science.1084123.

Scaife, A. A., et al., 2012: Climate change projections and stratosphere-troposphere interaction. *Climate Dyn.*, **38**, 2089–2097, doi:10.1007/s00382-011-1080-7.

Scherhag, R., 1952: Die explosionsartigen Stratosphärenerwärmungen des Spätwinters 1951/52. *Ber. Dtsch. Wetterdienst (US Zone)*, **6**, 51–63.

Schimanke, S., J. Körper, T. Spangehl, and U. Cubasch, 2011: Multi-decadal variability of sudden stratospheric warmings in an AOGCM. *Geophys. Res. Lett.*, **38**, L01801, doi:10.1029/2010GL045756.

Schmidt, H., G. P. Brasseur, and M. A. Giorgetta, 2010: Solar cycle signal in a general circulation and chemistry model with internally generated quasi-biennial oscillation. *J. Geophys. Res.*, **115**, D00I14, doi:10.1029/2009JD012542.

Schmidt, H., et al., 2006: The HAMMONIA Chemistry Climate Model: Sensitivity of the Mesopause Region to the 11-Year Solar Cycle and CO2 Doubling. *J. Climate*, **19**, 3903, doi:10.1175/JCLI3829.1.

Schmidt, H., et al., 2013: The response of the middle atmosphere to anthropogenic and natural forcing in the cmip5 simulations with the mpi-esm. *J. Adv. Model. Earth Syst.*, doi:10.1002/jame.20014, in press.

Schnadt, C. and M. Dameris, 2003: Relationship between North Atlantic Oscillation changes and stratospheric ozone recovery in the Northern Hemisphere in a chemistry-climate model. *Geophys. Res. Lett.*, **30**, 1487, doi:10.1029/2003GL017006.

Schoeberl, M. R., A. R. Douglass, R. S. Stolarski, S. Pawson, S. E. Strahan, and W. Read, 2008: Comparison of lower stratospheric tropical mean vertical velocities. *J. Geophys. Res.*, **113 (12)**, D24109, doi:10.1029/2008JD010221.

Semeniuk, K. and T. G. Shepherd, 2001: Mechanisms for Tropical Upwelling in the Stratosphere. *J. Atmos. Sci.*, **58**, 3097–3115, doi:10.1175/1520-0469(2001)058⟨3097:MFTUIT⟩2.0.CO;2.

Seviour, W. J. M., N. Butchart, and S. C. Hardiman, 2012: The Brewer-Dobson circulation inferred from ERA-Interim. *Q. J. R. Meteorol. Soc.*, **138**, 878–888, doi:10.1002/qj.966.

Shaw, T. A. and T. G. Shepherd, 2007: Angular Momentum Conservation and Gravity Wave Drag Parameterization: Implications for Climate Models. *J. Atmos. Sci.*, **64**, 190, doi:10.1175/JAS3823.1.

Shepherd, T. G. and C. McLandress, 2011: A Robust Mechanism for Strengthening of the Brewer-Dobson Circulation in Response to Climate Change: Critical-Layer Control of Subtropical Wave Breaking. *J. Atmos. Sci.*, **68**, 784–797.

Sigmond, M., P. C. Siegmund, E. Manzini, and H. Kelder, 2004: A Simulation of the Separate Climate Effects of Middle-Atmospheric and Tropospheric CO_2 Doubling. *J. Climate*, **17**, 2352–2367, doi:10.1175/1520-0442(2004)017⟨2352:ASOTSC⟩2.0.CO;2.

Smith, K. L., C. G. Fletcher, and P. J. Kushner, 2010: The Role of Linear Interference in the Annular Mode Response to Extratropical Surface Forcing. *J. Climate*, **23**, 6036–6050, doi:10.1175/2010JCLI3606.1.

Spangehl, T., U. Cubasch, C. C. Raible, S. Schimanke, J. Körper, and D. Hofer, 2010: Transient climate simulations from the Maunder Minimum to present day: Role of the stratosphere. *J. Geophys. Res.*, **115**, D00I10, doi:10.1029/2009JD012358.

Stenke, A. and V. Grewe, 2005: Simulation of stratospheric water vapor trends: impact on stratospheric ozone chemistry. *Atmos. Chem. Phys.*, **5**, 1257–1272.

Stevens, B., et al., 2013: The atmospheric component of the mpi-m earth system model: Echam6. *J. Adv. Model. Earth Syst.*, doi:10.1002/jame.20015, in press.

Stiller, G. P., et al., 2012: Observed temporal evolution of global mean age of stratospheric air for the 2002 to 2010 period. *Atmos. Chem. Phys.*, **12**, 3311–3331, doi:10.5194/acp-12-3311-2012.

Tabazadeh, A., M. L. Santee, M. Y. Danilin, H. C. Pumphrey, P. A. Newman, P. J. Hamill, and J. L. Mergenthaler, 2000: Quantifying Denitrification and Its Effect on Ozone Recovery. *Science*, **288**, 1407–1411, doi:10.1126/science.288.5470.1407.

Taguchi, M., 2008: Is There a Statistical Connection between Stratospheric Sudden Warming and Tropospheric Blocking Events? *J. Atmos. Sci.*, **65**, 1442, doi:10.1175/2007JAS2363.1.

Taylor, K. E., R. J. Stouffer, and G. A. Meehl, 2012: An Overview of CMIP5 and the Experiment Design. *Bull. Amer. Meteor. Soc.*, **93**, 485–498, doi:10.1175/BAMS-D-11-00094.1.

Teisserenc de Bort, L., 1902: Variations de la temperature de l'air libre dans la zone comprise entre 8 km et 13 km d'altitude. *C. R. Acad. Sci., Paris*, **138**, 42–45.

Tomassini, L., E. P. Gerber, M. Baldwin, F. Bunzel, and M. Giorgetta, 2012: The role of stratosphere-troposphere coupling in the occurrence of extreme winter cold spells over northern europe. *J. Adv. Model. Earth Syst.*, submitted.

Torrence, C. and G. P. Compo, 1998: A Practical Guide to Wavelet Analysis. *Bull. Amer. Meteor. Soc.*, **79**, 61–78, doi:10.1175/1520-0477(1998)079⟨0061:APGTWA⟩2.0.CO;2.

Tung, K. K. and R. S. Lindzen, 1979: A Theory of Stationary Long Waves. Part I: A Simple Theory of Blocking. *Mon. Wea. Rev.*, **107**, 714, doi:10.1175/1520-0493(1979)107⟨0714:ATOSLW⟩2.0.CO;2.

Valcke, S., 2013: The oasis3 coupler: a european climate modelling community software, geosci. model dev., 6, 373-388, doi: 10.5194. gmd-6-373-2013.

van Loon, H. and K. Labitzke, 1987: The Southern Oscillation. Part V: The Anomalies in the Lower Stratosphere of the Northern Hemisphere in Winter and a Comparison with the Quasi-Biennial Oscillation. *Mon. Wea. Rev.*, **115**, 357, doi:10.1175/1520-0493(1987)115⟨0357:TSOPVT⟩2.0.CO;2.

van Vuuren, D. P., et al., 2011: The representative concentration pathways: an overview. *Climatic Change*, **109**, 5–31.

Varotsos, C., 2002: The southern hemisphere ozone hole split in 2002. *Environ. Sci. Pollut. Res.*, **9**, 375–376.

Waugh, D. and T. Hall, 2002: Age of Stratospheric Air: Theory, Observations, and Models. *Rev. Geophys.*, **40**, 1010, doi:10.1029/2000RG000101.

White, W. B. and Z. Liu, 2008: Resonant excitation of the quasi-decadal oscillation by the 11-year signal in the Sun's irradiance. *J. Geophys. Res.*, **113**, C01002, doi:10.1029/2006JC004057.

Acknowledgements

This study was funded by the German Research Foundation (DFG) through the project SHARP (Stratospheric Change and its Role for Climate Prediction).

I would like to thank...

- ⋆ Dr. Hauke Schmidt, for helpful discussions, all the proofreading, patience, for giving me the opportunity to work on this research topic, and for being my IMPRS advisor.
- ⋆ Dr. Sebastian Rast, for support, helpful discussions, and insights into the ECHAM6 General Circulation Model.
- ⋆ Dr. Elisa Manzini, for help, proofreading, and for insights into the treatment of different types of wave drag at the model lid.
- ⋆ Dr. Marco Giorgetta, for help, for insights into the transformed Eulerian Mean framework, and for being my IMPRS co-advisor.
- ⋆ Dr. Jin-Song von Storch, for supervising my supervisors as my IMPRS panel chair, and for cheering me up after I screwed up a talk.
- ⋆ Prof. Dr. Bjorn Stevens, for a nice atmosphere in *The Atmosphere in the Earth System.*
- ⋆ Dr. Edwin Gerber, for help, proofreading, for insights into more or less everything related to this thesis, and for motivating discussions.
- ⋆ Dr. Alexey Karpechko, for help, proofreading, for insights into the Northern Annular Mode, and for motivating discussions.
- ⋆ Dr. Harald Bönisch, for help, motivating discussions, for insights into the age of stratospheric air, and for a nice train ride from Grindelwald to Frankfurt.
- ⋆ Prof. Dr. Martin Dameris, for support, and for coordinating the SHARP-BDC subproject.
- ⋆ Prof. Dr. Ulrike Langematz, for support, and for coordinating the SHARP project.
- ⋆ Aslak Grinsted, for the Crosswavelet and Wavelet Coherence Tool.

Additionally, I would like to thank...

- ⋆ my parents, Petra and Manfred Bunzel, for everything.
- ⋆ Vera Hermanns, for the last 7 years. Without her this thesis would not have been possible.

- my colleagues at MPI-M, especially Mathias Heinze, Delf Neubersch, Max Popp, Jan Ackmann, Juliane Petersen, Christina Rieckers, Nina Maaß, as well as the football and tennis communities, for distractions, help and support in difficult times, and for all the nice moments.
- my colleagues in the SHARP project, especially Hella Garny, Blanca Ayarzagüena, Sophie Oberländer, Stefanie Meul, and Stefan Lossow, for helpful discussions, and a nice and motivating working atmosphere.
- Antje Weitz and Cornelia Kampmann, for all their help, support, and organisation.

ISSN 1614-1199